Cinvestav-Querétaro

CENTRO DE INVESTIGACIÓN Y DE ESTUDIOS AVANZADOS

DEL INSTITUTO POLITÉCNICO NACIONAL

UNIDAD QUERÉTARO

Análisis del Espectro de Fotoemisión del Co 2*p* en Cobalto Metálico y Oxidado

Tesis que presenta

Dagoberto Cabrera Germán

Para Obtener el Grado de

Maestro en Ciencias

En la Especialidad de

Materiales

Director de Tesis:

Dr. Alberto Herrera Gómez

Santiago de Querétaro, Qro. Septiembre de 2015

For Lauren,

my beloved fiancée whose

never ending Love keeps me

pursuing my passion.

My Dad, Mom and Sister

Patience, Sacrifice,

Encouragement.

A product of the impact you

have had in my life, this will

forever be yours.

ACKNOWLEDGEMENTS

- Al Profesor Dr. Alberto Herrera Gómez por darme la oportunidad de ayudarle en el fascinante mundo de la ciencia. Aprecio mucho los esfuerzos que hizo como mi mentor; recibiéndome, apoyándome y formándome durante estos años. Bajo su dirección he podido entender conceptos, tal vez pocos, pero que me han intensificado el deseo de seguir el camino de la ciencia. Usted es un ejemplo de excelencia como investigador y profesor. Gracias.
- A mis sinodales: Dr. Andrés de Luna Bugallo y Dr. Sergio Joaquín Jiménez Sandoval; gracias por sus comentarios y sugerencias que enriquecieron mi trabajo de tesis.
- Al Dr. Leonardo Soriano el cual estuvo al pendiente de mis experimentos e interpretación de estos; me mostró varias formas de cómo interpretar lo que sucede en la naturaleza.
- Agradezco al Dr. Wencel de la Cruz por el tiempo que me dedicó y los conocimientos que me brindó tan desinteresadamente. Aprovecharé lo poco que le pude aprender.
- Quiero reconocer la labor que desempeña el CINVESTAV-Querétaro. Personal administrativo, técnicos y sobre todo a los profesores que me ofrecieron una pequeña parte de sus conocimientos.
- Agradezco todos los momentos buenos y malos, apoyo, comentarios y motivación que he recibido por parte de los "babies" Han hecho que mi estancia, en una idiosincrasia totalmente diferente, haya sido muy agradable y fructífera. Compañeros Julio Mata, *Shocko*, *Dalia*, *Gusifer*, Oscar Ceballos, Yuri Chipatecua, Cynthia Negrete, Víctor Arellano, Pierre Dávalos y Alejandro Torres. Con ustedes muy agradecido me encuentro.
- Agradezco al Dr. Gustavo Gómez Sosa y al Ing. Alfredo Muñoz Salas por la asistencia técnica que me brindaron, así como la capacitación que me dieron para poder completar este trabajo de tesis.

- Al Dr. Zeuz Montiel González y a la Dra. Dalia Mazón Montijo por las atenciones, asesorías y comentarios. Ustedes son un gran ejemplo para mí.
- Al CONACyT por haberme otorgado la beca nacional de inversión en el conocimiento #369900. Pienso que lo que se consiguió con su apoyo contribuirá al desarrollo de la ciencia en México.
- I want to thank all the love, support and encouragement given to me by my soon to be wife Lauren; I hope our bond is even stronger after all that we have endured during this years.
- Finalmente a mi familia por todo lo que ha hecho por mí, nunca podré terminar de agradecer y siempre estaré en deuda con ustedes. Sin duda, ustedes me hacen ser muy afortunado de lo que me sucede. Sólo espero poder ser un poco el hijo, hermano, nieto que se merecen. Gracias y cada lección de vida la llevaré conmigo siempre.

ABSTRACT

X-Ray photoelectron spectroscopy as a quantitative technique requires an accurate experimental data reproduction and background modeling. However, data extracted from Cobalt and cobalt oxides present many complications such as shake-up features, Auger line interferences, peak asymmetries and strong background contributions to the spectra making the peak fitting procedure a challenging task. Traditionally, the assessment of X-Ray photoemission spectra is mainly done in a qualitative fashion. In this work metallic cobalt thin films (~25nm) were deposited on a Si(100) substrate. Oxidation was performed controlling pressure and time of ultra-high purity O_2 at high vacuum. A metallic Cobalt thin film was oxidized in order to obtain a partially and fully oxidized film, while a metallic Cobalt film with impurities was chemically assessed during subsequent oxidation stages. The reproduction of experimental data is achieved simultaneously reproducing both Co $np_{3/2}$ and $np_{1/2}$ photoemission branch. It is found that the often overlooked Auger LMM structure has a very strong contribution to the Co *2p* spectra when Al $K\alpha_1$ radiation is used. Photoemission peaks present distinct asymmetry values that indicate multiplet splitting effects occur in the Co electron system upon photoemission. Determination of satellite peak position with respect to mainline, the branching splitting that is the binding energy difference between the $j = 3/2$ and $j = 1/2$ photoemission branches, indicate that shake-up features are produced by correlation effects with strong angular momentum dependency.

Chemical assessment was done by quantification of peak areas and the employment of a multilayer model resulting in close to stoichiometric oxide values. The background modeling, Auger peak interference determination and peak area estimations accurately account for the photoemission line spectral shapes and peak intensities. This was concluded in part, by the coherency of the results of oxide composition and close fits to experimental data.

RESUMEN

El uso de espectroscopia de fotoelectrones por Rayos-X como una técnica cuantitativa requiere de una reproducción de datos experimentales y un modelado del "background" preciso. Sin embargo, la información extraída de Cobalto y óxidos de cobalto presenta muchas complicaciones, tal como, señales shake-up, interferencias Auger, picos asimétricos y una fuerte contribución del background al espectro de fotoemisión que hace que el procedimiento de ajuste sea una tarea desafiante. Tradicionalmente, la evaluación del espectro de fotoemisión por Rayos-X regularmente se hace de manera cualitativa. En este trabajo, películas ultra-delgadas de Cobalto metálico (~25nm) han sido depositadas sobre un sustrato de Si(100). Oxidación se llevó a cabo controlando la presión y tiempo de O_2 de ultra-alta pureza en alto vacío. Una película delgada de cobalto fue oxidada con el objeto de obtener una película parcial y totalmente oxidada, mientras que una película de cobalto metálico con impurezas fue evaluada químicamente durante diferentes etapas de oxidación. La reproducción de datos experimentales se hace simultáneamente en las dos ramas Co $np_{3/2}$ and $np_{1/2}$ de fotoemisión. Se obtiene que la en ocasiones olvidada estructura Auger LMM presenta una fuerte contribución el espectro de Co 2*p* cuando radiación Al $K\alpha_1$ es utilizada. Los picos de fotoemisión presentan diferentes asimetrías que indican que efectos de "splitting" múltiples ocurren en el sistema electrónico de Co al momento del proceso de fotoemisión. La determinación de la posición de satélites con respecto a la línea principal, el "branching splitting" que es la diferencia en energía de enlace entre la *j=3/2* y *j=1/2* ramas de fotoemisión, indica que las señales shake-up son producidas por efectos de correlación con una fuerte dependencia con el momento angular. Evaluación química fue realizada mediante la cuantificación de las áreas de pico y el uso de un modelo multicapas que arroja resultados muy cercanos a óxidos estequiométricos. El modelado del background, interferencia de picos Auger y las estimaciones de área de picos acertadamente dan cuenta de las formas espectrales de las líneas de fotoemisión e intensidades de pico. Esto fue concluido en parte por

la coherencia de los resultados con la composición de óxidos y los ajustes cercanos a datos experimentales.

Table of Contents

LIST OF FIGURES

LIST OF TABLES

1 Introduction

1.1 Rationale for this Thesis

The use photoemission spectroscopy (XPS) in the field of micro- and nano-materials is very important because of the possible chemical state information that can be extracted. Fundamental, as well as applied science, have a strong interest in understanding the true nature of the electronic structure of these materials, in terms of all the features that a core level spectra might show, like fine structures and satellites which lead to several final state interactions aside from chemical assessment.[1]

The technological importance of evaluating the chemical state of materials that incorporate transition metals is that in the integrated circuit industry, it is imperative to know the properties of metal-oxide-semiconductor structures or metal on Si substrates arrangements,[2] in order to develop electronic devices with high performance and reliability.

Transition metals play an important role in the fields of surface sciences, catalysis, environmental, clean energies and health. Cobalt especially in nanostructured materials is currently being studied for its potential to clean air, lockdown and elimination of virsues[3], solid state devices, biofuels and catalysis related to renewable energy technologies.[4] The dimension of these materials are ideal for its study using XPS; yet challenging issues still need to be resolved in terms of the output XPS offers as a characterization technique, thus improving the technological application of transition metals.

XPS analysis technique is capable of quantifying the amount and distribution of an element within a certain material. Without the need of reference materials, quantification is done with the relative ease in which core level signals are recorded and subsequently peak fitted. However, the curve fitting process is non-trivial and under ideal conditions an accuracy no better than 5% can be reached accompanied of errors up to 30%.[5]

Quantitative analysis is a challenging task due to the plasmon loss, shake-up peaks, peak asymmetries and intense background. These complex contributions can lead to inaccurate results on the assessment of the chemical state of thin films,[6] specially the Co 2*p* core level spectra that features Auger peaks that further complicate the situation.[7]

Still today the background contribution to the photoemission spectra of transition metals is not successfully taken into account,[5] there have been efforts[6,8] to do so by applying traditional background types, but both photoemission branches that comprise the 2*p* core level spectra are not accounted for. Nevertheless, using complementary techniques for background subtration[9–11] is a viable method to approximate the photoemission lines true intensity; though, the method itself is not practical.

The issue to overcome is the accurate estimation of peak area intensities of all the features that comprise the photoemission spectra, thus, this requires a proper background modeling[12] and close experimental data reproduction using state of the art algorithms. In this work, the XPS data quantification difficulties are tackled with the aforementioned and a rigorous approach[13] to evaluate the peak area calculations is implemented. In principle, the cobalt core level photoemission features are accurately resolved and results serve as experimental evidence to help understand the true nature of how the strongly correlated system within cobalt and cobalt oxides respond to photoemission.

1.2 Hypothesis

By reproducing the experimental photoemission spectra using peak fitting and an accurate background modeling it is possible to quantify and identify features in the photoemission spectra in order to achieve an accurate chemical assessment of the material measured.

1.3 Objectives

1.3.1 General

To quantify the X-Ray photoemission spectra of metallic cobalt and cobalt oxides achieving an accurate experimental data reproduction of the XPS features via peak fitting.

1.3.2 Specific

- Obtain photoemission spectra from metallic cobalt.
- Obtain photoemission spectra from cobalt oxide thin films.
- Reproduce experimental data using peak fitting.
- Achieve an accurate background modeling using state of the art algorithms.
- Calculate peak areas alongside their uncertainty values.
- Assess the chemical state of the films using a multilayer model.

1.4 Structure of the Thesis

The present work is divided in 6 chapters. Chapter 1 describes the rationale for the thesis project and scientific goals to be achieved. Chapter 2 gives an insight into the physical principles of XPS as a surface analysis technique. Different spectra line shapes are discussed, as well as a brief description of the Shirley background. This chapter also includes the deduction of the multilayer model which is the primary quantification model in this work. Previous work done on Co and cobalt oxides using XPS is later described. Chapter 3 describe the experimental details of the thesis. Chapter 4 is a listing of all the peak fits obtained alongside the calculated peak shape and background parameters; at the ending of the chapter the multilayer results of the chemical assessment of the materials analyzed is presented. Chapter 5 deals with the analysis and discussion of results where some of the XPS features found are evaluated considering other scientific reports. Chapter 6 finally lists the conclusions generated from the completion of this work.

2 Background

2.1 X-Ray Photoelectron Spectroscopy (XPS)

What we know today about photoelectron spectroscopy comes a long way since the first works, in the 19th century, of Heinrich Hertz,[14] where the properties of certain materials under the exposure to light were first described. In the beginning of the 20th century, Albert Einstein[15] subsequently explained the photoelectric effect, introducing the term photon (light), in terms of a transfer of energy from photons to electrons, Rutherford et al.[16,17] then realized that this energy transfer involves the photon energy and the electron binding energy in such a way their difference is the kinetic energy in which the same electron will be emitted.

More theoretical predictions came to stall, mainly to experimental difficulties that the technology of the time could not resolve. After the development of more precise electron spectrometers, Kai Siegbahn[18] was the first to record the first photoemission spectra using high resolution and the core level binding energies accompanied of the shift due to chemical bonding was sufficient evidence to demonstrate the capabilities of the technique that further popularized it until now.

2.1.1 Principles of XPS

The basic process within photoemission spectroscopy concerns the ionization of a core level caused by the interaction of photons with core electrons. The ejected electron is referred to as a photoelectron, because the initially bound electron is ejected by a photon interaction. The photoelectron will have a kinetic energy that can be fairly approximated by the difference between photon energy and core level binding energy; kinetic energy is recorded by an electron spectrometer and photoelectrons are plotted in terms of intensity versus their respective binding energy and the result is what we call photoemission spectra. The intensity of photoelectrons

in the spectra will show up in the form of photoemission peaks that originate from the discrete nature of the atomic energy levels.[5,19,20]

In XPS, photoelectrons are labeled in terms of quantum numbers that correspond to the core level and angular momentum of the ground state or the involved photoemission transition in the case of Auger photoelectrons. The nomenclature can give an insight on some of the properties of the resulting spectra and almost all of the photoemission properties will depend on angular momentum.

The total angular momentum, when the Russell-Saunders coupling scheme applies[21], is described by the absolute value of the vectorial addition of angular and spin momentum expressed as $\bar{j} = |\bar{l} + \bar{s}|$, for different coupling schemes the angular momentum requires the use of specific term symbols.

An effect of angular momentum in the photoemission spectra is the presence of multiplet structures, these correspond to a photoemission line that is split in several peaks. Generally, these come in pairs called doublets whose relative intensities depend on the degeneracy of the sates, described as $2j+1$ where separation between peaks will depend on the magnitude of the spin orbit coupling. Figure 2.1 is a schematic representation taken from Ref[5] of all the possible stationary ground state present in an atom, the figure also shows the two most common nomenclatures used in electron spectroscopy. We can observe how the ground states are described by their given quantum numbers and the possible number of electrons they can hold. It is noteworthy that spin orbit coupling magnitude increases with an increasing atomic number and the magnitude decreases with increasing n and l This properties can be explained solving the Dirac equation[21] for a given potential or when perturbation theory is taken into account.[22]

The process of photoemission is shown schematically in Figure 2.2 along with the description of the Auger process. In practical terms, the binding energy parameter is what identifies specifically an electron, and it is calculated using the following expression[19]

$$E_B = h\nu - E_K - W \qquad (2.1)$$

Where $h\nu$ is the photon energy, E_K is the kinetic energy at which the photoelectron reaches de analyzer and W is the spectrometer work function. We can also observe the emission of an Auger electron, which is a process that occurs when an internal transition is promoted after the process of direct photoemission, because the atom once excited must find a way to relax. The kinetic energy of Auger photoelectrons is always constant, because it depends on the energy difference of the internal transition.

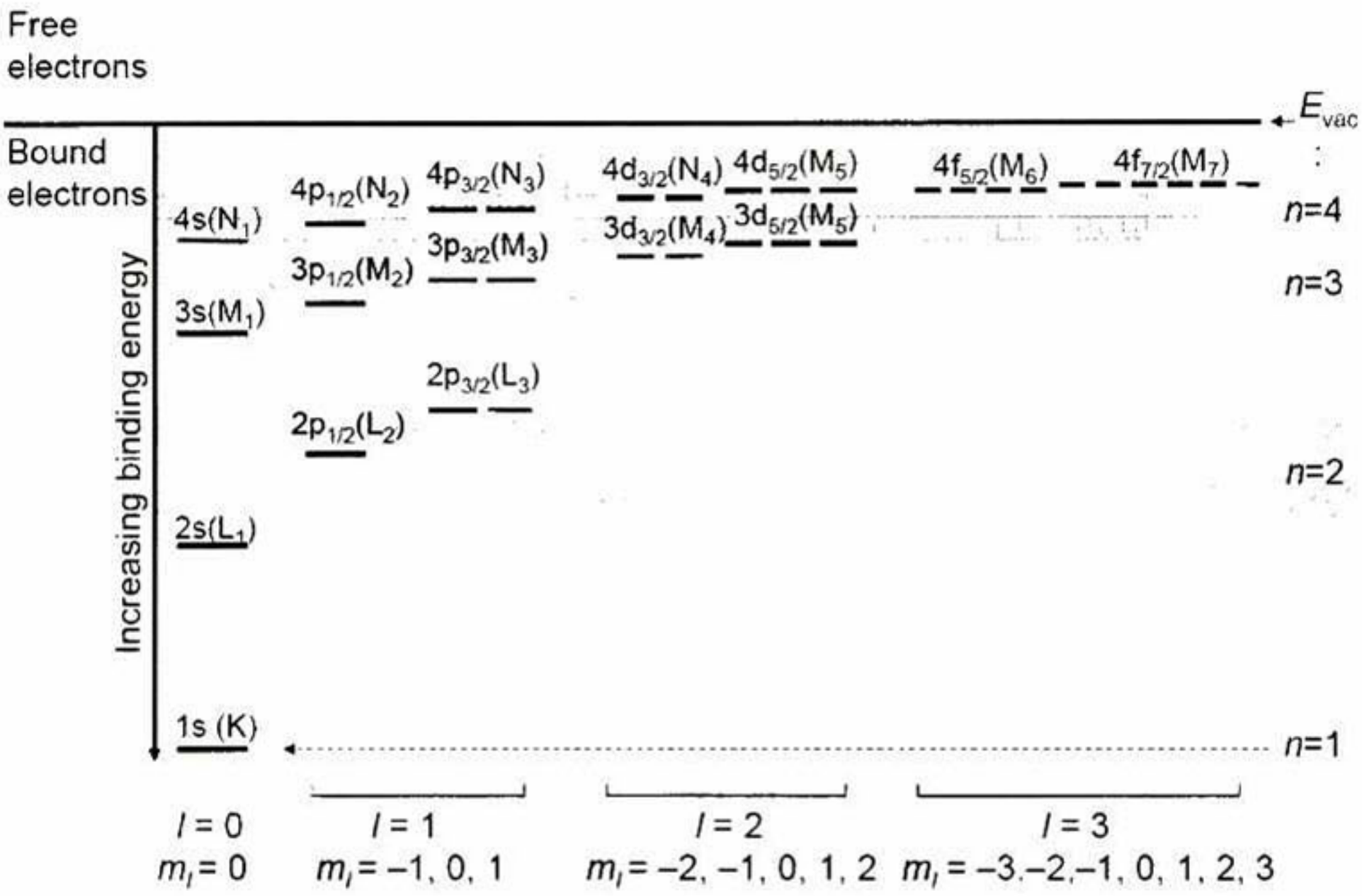

Figure 2.1 Energy level diagram of the stationary ground states of an atom. The quantum numbers in each state represent how electrons are described if present in a certain state. Description using spectroscopic notation is shown on top of the state, while X-Ray notation is in brackets. Source: Ref[5].

The XPS equipment does not follow expression (2.1) as straightforward. There are several energy terms that need to be taken into account. The spectrometer and the sample must be in electric contact to enable a reference energy to be used in the measurement of the electron energy, this reference is the Fermi energy (E_F) at which the binding energy is referenced to. The kinetic at which the photoelectron is expelled from the sample is

$$E_K^1 = h\nu - E_B - \phi_s \qquad (2.2)$$

Here, ϕ_s is the work function of the sample.

The relevant energy terms in the calculation binding energy are shown in Figure 2.3. It can be easily derived that the kinetic energy measured by the analyzer is given by

$$E_K = h\nu - E_B - \phi_s - (W - \phi_s) \qquad (2.3)$$

Thus, by simplification one obtains equation(2.1).[23]

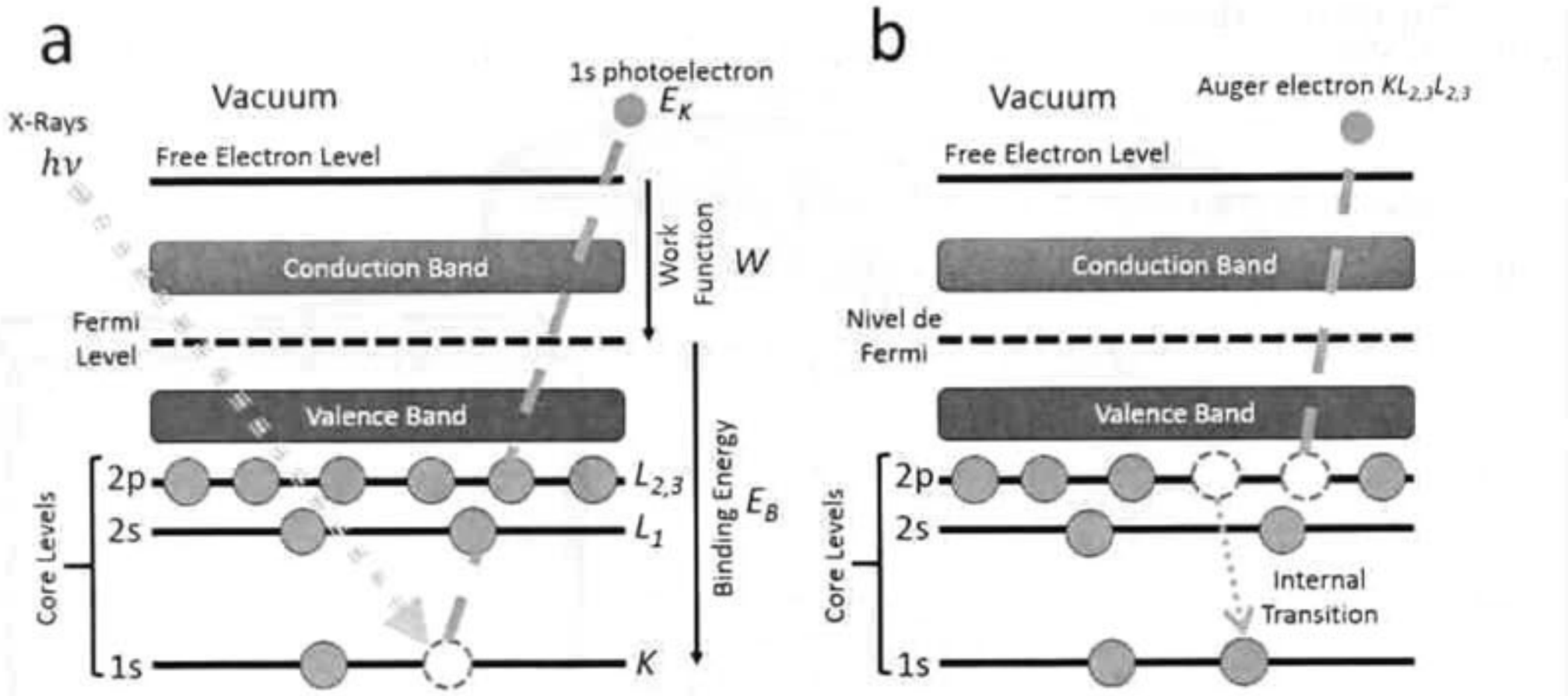

Figure 2.2 Scheme of the a) photoemission basic process were K or 1s electron is emitted and b) is the subsequent relaxation of the ionized atom via an Auger electron ejection.

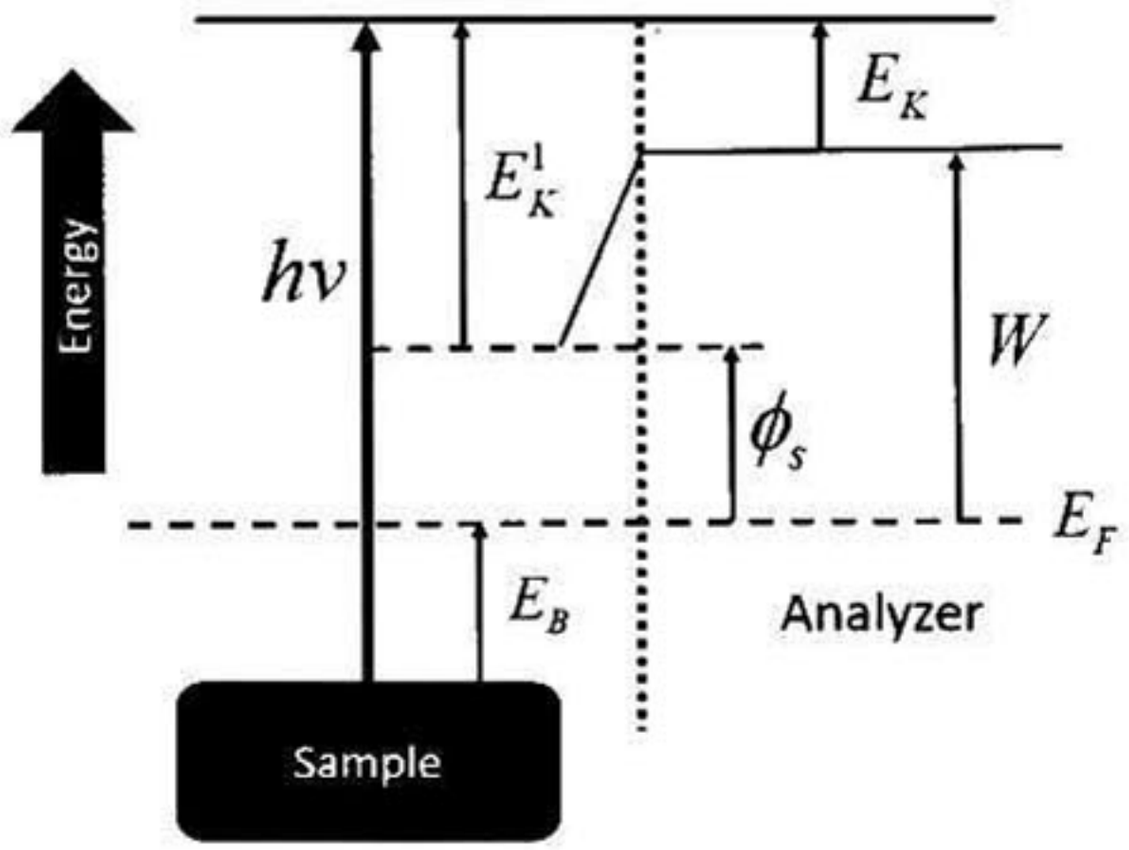

Figure 2.3 Scheme of the energy terms involved in the energy measurement in XPS. The emitted electron overcomes the work function of the sample ϕ_s and the analyzer measures the kinetic energy reduced by the difference between analyzer and sample work functions. Energy calculations are done referencing with respect to the Fermi level.[20,23]

Once calibration is done, the latter expressions can be further simplified dropping all the work function terms, however this is only valid for a conductive sample that in

electric contact has the same Fermi level as the analyzer. If not, a charge compensator must be used in order to correct shifts caused by insulator charging.
A schematic representation of the experimental arrangement of a XPS measurement is shown in Figure 2.4. We can observe the typical use of a monochromatized X-Ray source with angles that characterize the Rowland circle. There are several geometrical factors that affect the photoelectron intensity, these are further explained elsewhere.[24]

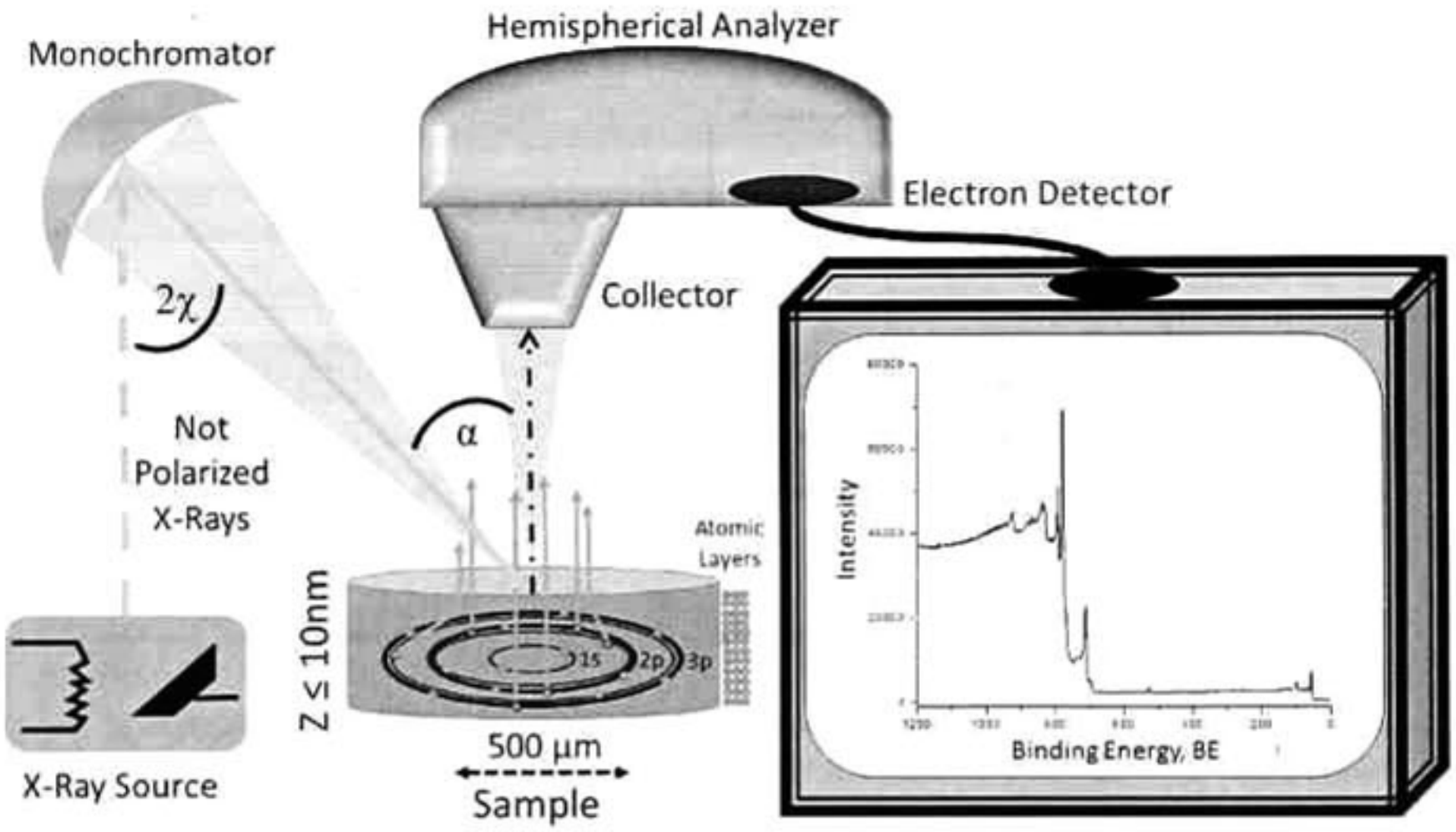

Figure 2.4 Typical experimental set-up of a XPS measurement. Non polarized X-Rays are produced and are later monochromatized before reaching the sample. After the photon-electron interaction, photoelectrons are ejected from the first 10nm. These photoelectrons are collected and recorded by a spectrometer that outputs the electron intensity in the form of a spectrum.

The typical sampling depth is no more than 10nm in general, despite X-Rays penetrate the sample several micrometers, sampling depth is limited by inelastic mean free path (IMFP) of electrons and the effective attenuation length (EAL); these are defined as the inherent probability electrons have to suffer energy losses and therefore reach the analyzer when inelastic and elastic scattering is taken into account following the photoelectron escape trajectory from the material. This is important because intensity is attenuated in function of the take-off angle and attenuation length the photoelectron has with respect to the material analyzed[19]
Also, if electrons suffer energy losses due to scattering, they will no longer form a peak in the spectrum and they will rather constitute a part of the photoemission background.[25]

2.1.2 Photoionization Cross Section

The photoabsorption cross section is one of the most important parameters in the photoemission process. The subshell photoionization cross sections is defined as the probability that a photon with a given energy has to be absorbed by a given subshell. In this sense, the cross section accounts for a fraction of photons that actually interact with the core levels and produce the photoemission phenomena, hence, the intensity of electrons in the final photoemission spectrum greatly depend on this parameter.

Using Hartree-Fock-Slater wave functions where the averaged initial states of a single electron are in a central field potential and summing over all final states; the atomic subshell photoionization cross section can be expressed as[26]

$$\sigma_{nl}(h\nu)=\frac{4\pi^2\alpha_0 a_0^2}{3}\frac{N_{nl}}{2l+1}h\nu\left[lR_{l-1}^2(\varepsilon_{kin})+(l+1)R_{l+1}^2(\varepsilon_{kin})\right] \qquad (2.4)$$

Where σ_{nl} is expressed in cm^2, a_0 is the Bohr radius, α_0 the fine structure constant, N_{nl} number of electrons in the nl subshell, energy corresponds to $\varepsilon_{kin}=h\nu$ and $R_{l\pm1}(\varepsilon_{kin})$ are one electron radial dipole matrix elements that can be expressed in terms of different dipole approximations.

There are several issues that affect the photoelectric cross section, a main one is the measurement outcome regarding the geometrical factor of the angle between X-Rays and electron analyzer that impacts the intensity seen in the spectrum,[27] therefore the chemical assessment of elements requires the use of differential cross sections, so that quantitative analysis may be done consistently across a probing depth and comparable with other XPS tools.

The angular dependence of the photoelectric differential cross section, for a single electron model after electric-dipole interactions are taken into account and for photons that are linearly polarized, is given by[28,29]

$$\frac{d\sigma_{nl}(h\nu)}{d\Omega}=\frac{\sigma_{nl}(h\nu)}{4\pi}\left[1+\beta_{nl}(h\nu)\frac{1}{2}\left(3\cos^2\gamma-1\right)\right] \qquad (2.5)$$

Where $\beta_{nl}(h\nu)$ is the asymmetry parameter and γ is the angle between the photon polarization vector and the direction of the photoelectron.

If the X-Ray source is unpolarized, like the majority of the XPS tools, the factor $\cos^2\gamma$ must be averaged over all the possible photon polarization vectors. When photons are emitted with no preferred polarization, one obtains that the averaged differential subshell photoelectric cross section is[27,30]

$$\overline{\frac{d\sigma_{nl}(h\nu)}{d\Omega}}_{U} = \frac{\sigma_{nl}(h\nu)}{4\pi}\left[1+\beta_{nl}(h\nu)\frac{1}{2}\left(3\frac{\sin^2\alpha}{2}-1\right)\right] \qquad (2.6)$$

Subindex "U" refers to unpolarized X-Rays and α is the angle between the electron analyzer axis and the X-ray source.

When a monochromatized source is used, the X-Ray beam is polarized by the effect of the Bragg reflection occurred at the monochromator. After the monochromator focuses the X-Ray beam, the electric field is polarized in two different ways; σ polarization corresponding an electric field parallel to the atomic Bragg planes and the π-polarization to the second polarization. The reflectivity of both polarizations are different where the π-polarized X-Rays is reduced by a factor of $\cos^2 2\chi$

The factor $\cos^2\gamma$, likewise the unmonochromatized case, must be averaged over possible polarizations. However, in this case a weighted averaged considering the partial reflection of the π-polarization must be computed. Therefore, when a monochromator is used, the differential subshell photoelectric cross section is given by[31]

$$\overline{\frac{d\sigma_{nl}(h\nu)}{d\Omega}} = \frac{\sigma_{nl}(h\nu)}{4\pi}\left[1+\beta_{nl}(h\nu)\frac{1}{2}\left(3\sin^2\alpha\frac{\cos^2 2\chi}{1+\cos^2 2\chi}-1\right)\right] \qquad (2.7)$$

Where 2χ represents the angle between the incident and reflected X-Rays at the monochromator. In this work, the use of a monochromatized X-Ray source demands the use of the latter expression.

2.1.3 Core Line Spectral Shapes

Using XPS as a quantifying technique requires peak fitting the spectra with diverse spectral line shapes in order to reproduce experimental data and calculate the photoelectrons intensity by means of peak area estimations.

Fundamentally an accurate experimental data reproduction, besides the quantitative analysis, gives an insight to the chemical state and behavior of the electronic structure in the process of photoemission that an atom will have in a certain material. It is common that peaks comprising the photoemission spectra are symmetric. One of the most typical line shapes is the Gaussian function. The function is given by[32]

$$G(E)=\frac{1}{\sigma\sqrt{2\pi}}e^{\frac{-(E-E_0)^2}{2\sigma^2}} \tag{2.8}$$

Where E_0 represents the peak center and σ is the standard deviation. The first part of the function is a constant scaling factor. The full width at half maximum (FWHM) is found by the next relationship[32]

$$FWHM=2\sqrt{2\ln 2}\,\sigma \tag{2.9}$$

Another important line shape is the often referred to as the Lorentzian function. The function can be expressed as[33]

$$L(E)=\frac{I}{1+\left(\frac{E-E_0}{\gamma}\right)^2} \tag{2.10}$$

Where I defines the amplitude or height of the function, in some special cases it can be expressed as a probability density function when $I=(\pi\gamma)^{-1}$ The FWHM of the Lorentzian function is defined by the scale parameter as 2γ

It is possible to produce a synthetic spectra using the pure above mentioned functions by themselves; but in XPS and various fields of spectroscopy, the signals presented in the spectra often occur by different broadening mechanisms. Therefore, we are interested in the Voigt profile; which is defined as the convolution between the Gaussian and Lorentzian functions. The Voigt profile is then,

considering both functions have the same peak center, given by the following expression:

$$V(E;\sigma,\gamma)=\int_{-\infty}^{\infty}G(E';\sigma)L(E-E';\gamma)dE' \qquad (2.11)$$

The Lorentzian function describes the finite lifetime at which the final vacancy state of the atom relaxes from the excited state, counting from the moment of its inception. It is an intrinsic property of every core subshell and generally lifetime decreases with an increase in binding energy.[1,34,35]

The Gaussian broadening mechanism can be referred to various factors related to the instrumental resolution of the XPS tool. The instrumental factors that contribute to the Gaussian broadening include the intrinsic broadness of the X-Ray source;[35] resolution, exit and entrance slits of the electron analyzer.[1,34]

The core line spectra shapes are often non symmetrical, especially in transition metal spectra. There has been several number of theories that explain peak asymmetries. Although, different in principle they all fundamentally deal with same problem, the creation of electron-hole pairs.[36–44] The core line asymmetry theory has a strong physical basis, but from the practical peak fitting standpoint, reproducing the asymmetries found in experimental XPS data is non-trivial and traditional line shapes present problems while reproducing experimental spectra.

In this work, peak asymmetries are reproduced employing the double-Lorentzian line shape.[45] This line shape is constructed first by taking a split Lorentzian function with different widths on each side of the function. The split function is of the following form:

$$L'(E;\gamma_1,\gamma_2)=\frac{I}{1+\left(\frac{E-E_0}{\gamma_i}\right)^2}\quad\begin{cases}L_1(E;\gamma_1) & -\infty<E\le E_0\\ L_2(E;\gamma_2) & E_0\le E<\infty\end{cases} \qquad (2.12)$$

Where $L'(E)$ is formed by two Lorentzian functions centered at E_0 but with different γ_i widths. A visual representation of equation (2.12) is shown in Figure 2.5 where the shaded area indicates the asymmetric characteristics of this mathematical

construct. The double-Lorentzian asymmetry parameter will therefore be the ratio between the widths of the left side Lorentzian to the right side Lorentzian function.

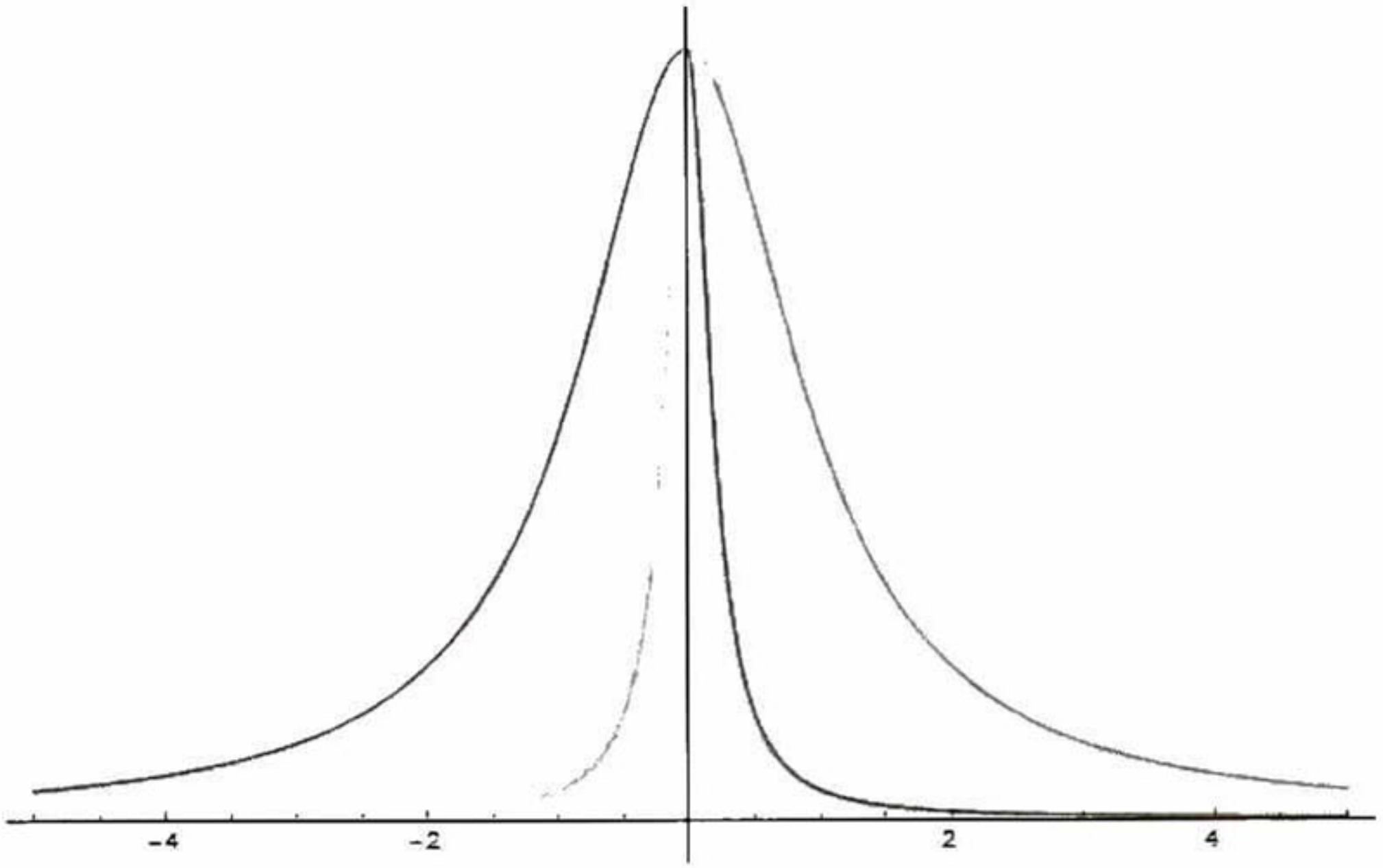

Figure 2.5 Plot of two Lorentzian functions that compose $L'(E)$. The shaded area represents the area under the split function $L'(E)$ that turns out to be an asymmetric function.

Then the double-Lorentzian function is the result of convoluting $L'(E)$ with a Gaussian function, given by

$$DL(E;\sigma,\gamma_{,}) = \int_{-\infty}^{\infty} G(E';\sigma) L'(E-E';\gamma_{,}) dE' \qquad (2.13)$$

An important property is that widths are dependent of each other in the fitting process. The double-Lorentzian function is also integrable, permitting its use in quantitative analysis and also produces very close fits of transition metal spectra.[45]

2.1.4 Brief Description of Photoemission Background Subtraction

Background subtraction consists of the evaluation of different background contributions to the photoemission spectra. Background subtraction in this work is done using the active method.[12]

The two most applied background models are the Shirley[46] and the Tougaard[47] backgrounds. The Shirley background to this day still lacks a strong physical explanation, but its use is necessary in quantitative studies,[12] while the Tougaard background possess a solid theoretical background[25] and in principle should be included in all photoemission studies.

The Shirley background reproduces the step like nature of photoemission peaks, were background in the lower binding energy side of the spectra is usually lower than the background in the higher binding energy side. The Shirley background[20,46,48,49] shape and intensity can be obtained through an iterative process where the formula is given by

$$S_i(E_B) = k_s \int_{E_B}^{+\infty} \{ j(E') - S_{i-1}(E') \} dE' \qquad (2.14)$$

Here i corresponds to each binding energy channel at which the spectrum is decomposed, where $i=0$ is the minimum binding energy value in the spectrum $(E_{B,\min})$, S_0 is a constant background and the background intensity S_i in each channel i is given by a proportionality factor k_s of the signal intensity $j(E') - S_{i-1}(E')$ in the previous energy channel. The formula converges when the background and photoemission intensity fulfill the condition $j_i(E_B) = S_i(E_B)$.

2.2 The Multilayer Model

The multilayer model is the fundamental model employed in this work to perform chemical assessment studies using calculated peak areas result of peak fitting. Its deduction follows the probability of no collision an electron will have in its path through the solid traveling a distance x is given by

$$dP(x) = 1 - \sigma \rho dx \qquad (2.15)$$

On the other side the probability of no collision traveling a distance $x+dx$ is

$$P(x+dx) = P(x)(1 - \sigma \rho dx) \qquad (2.16)$$

Using a Taylor expansion and reordering we obtain

$$dP(x) = -\sigma\rho P(x)dx \tag{2.17}$$

Integrating, evaluating at $x = 0$ and defining the effective attenuation length as $\lambda^{-1} \equiv \sigma\rho$ the latter equation obeys the Beer-Lambert relationship as

$$P(x) = e^{-\frac{x}{\lambda}} \tag{2.18}$$

The probability of no collision a photoelectron will have traveling through n atomic planes, a distance d from a depth x with an escape angle θ is schematized in Figure 2.6. The photoelectron probability of reaching vacuum will then be

$$d = x/\sin\theta \tag{2.19}$$

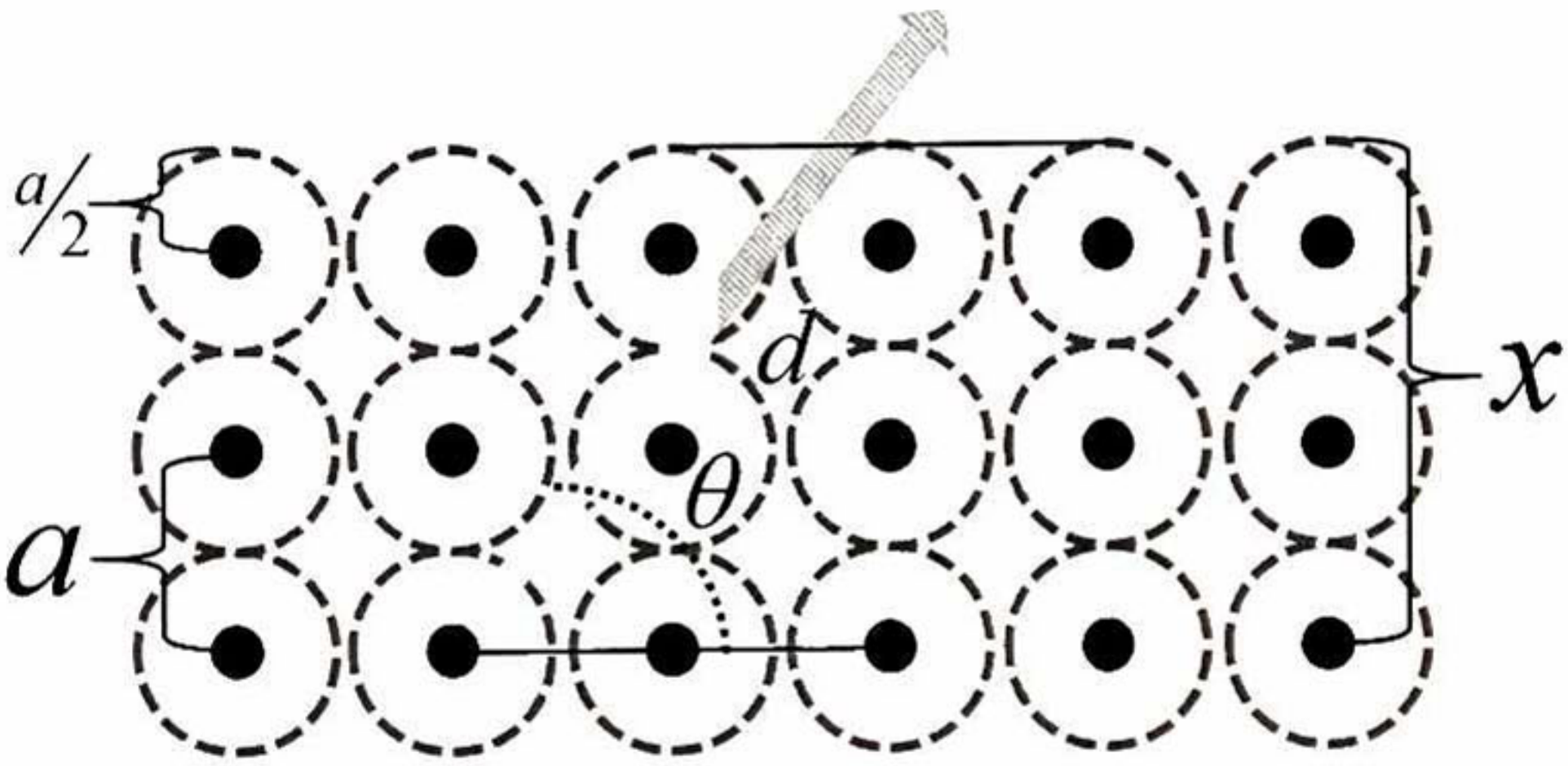

Figure 2.6 Schematic representation of the escape trajectory a photoelectron emitted from a depth x within the solid will have.

The photoelectron intensity is limited by the excitation of electrons located in different atomic planes; then the depth value that is associated to x accounting for N atomic planes is

$$x = \sum_{0}^{N} na + 0.5a \quad , \quad n = 0,1,2,...,N \tag{2.20}$$

Thus the photoemission intensity from an atomic layer is expressed as

$$I_n \propto e^{-\frac{(n+0.5)a}{\lambda\sin\theta}} \tag{2.21}$$

The latter equation is just a first approximation, hence an expression that approximates the photoelectron intensity measured by the XPS tool, involves accounting for several geometrical factors of the equipment.[24] Therefore, a more comprehensive approximation of the photoemission signal will be

$$I_n \approx sdA\frac{d\sigma}{d\Omega}d\Omega X(\vec{r})A(\kappa)aae^{-\frac{(n+0.5)a}{\lambda\sin\theta}} \tag{2.22}$$

Where s is the material superficial density, dA an area differential accounting for the X-Ray spot size, $\frac{d\sigma}{d\Omega}$ the differential photoionization subshell cross section, $X(\vec{r})$ is the X-Ray flux and $A(k)$ is the efficiency of the electron analyzer.

The X-Ray flux and electron-analyzer acceptance solid-angle can be modeled with Gaussian profiles given by

$$A(k) = A(\vec{r})\kappa \tag{2.23}$$

$$A(\vec{r}) = A_0 \exp\left[-\frac{d_x^2}{A_x^2} - \frac{d_y^2}{A_y^2}\right] \tag{2.24}$$

$$X(\vec{r}) = A_0 \exp\left[-\frac{d_x^2}{B_x^2} - \frac{d_y^2}{B_y^2}\right] \tag{2.25}$$

Where k is the photoelectrons kinetic energy, while d_x^2 and d_y^2 represents a distance with respect the axis of the analyzer.

It is possible to relate the above mentioned expressions using a constant, so we have that

$$c = X(\vec{r})A(\vec{r})aA \tag{2.26}$$

Now summing over the layers, the total photoemission intensity is given by

$$\frac{dI_T(\vec{r})}{dad\Omega} = \sum\frac{aI_n(\vec{r})}{dad\Omega} = c\frac{1}{k}s\frac{d\sigma}{d\Omega}e^{-\frac{a}{2\lambda\sin\theta}}\sum_0^N e^{-\frac{na}{\lambda\sin\theta}} \tag{2.27}$$

2.2.1 Photoemission Intensity from an Infinite Solid

The approximation considering that photoelectrons come from an infinite solid is valid because the substrate layer in general is larger than the XPS probing depth.

So, it is possible to define for a single layered material, the following change of variable:

$$\sum_{0}^{\infty} e^{-\frac{na}{\lambda \sin\theta}} = \sum_{0}^{\infty} b^n \tag{2.28}$$

Rewriting the last equation we obtain

$$\sum_{0}^{\infty} b^n = 1 + \sum_{1}^{\infty} b^n = 1 + b\sum_{1}^{\infty} b^{n-1} = 1 + b\sum_{0}^{\infty} b^m \tag{2.29}$$

The change of variable consisted in $m = n - 1$ and now it is easy to get

$$\sum_{0}^{\infty} b^n = \frac{1}{1-b} \tag{2.30}$$

It is then possible to express the equation for the intensity for an infinite solid is given by

$$\frac{dI_T(\vec{r})}{da\,d\Omega} = c\frac{1}{k}s\frac{d\sigma}{d\Omega}\frac{1}{1-e^{-\frac{a}{\lambda\sin\theta}}}e^{-\frac{a}{2\lambda\sin\theta}} \tag{2.31}$$

2.2.2 Photoemission Intensity from a Multilayered Material

For a material with a finite dimension, the change of variable follows:

$$\sum_{0}^{N} e^{-\frac{na}{\lambda \sin\theta}} = \sum_{0}^{N} b^n \tag{2.32}$$

Subtracting 1 to the last equation, it is possible to define:

$$\sum_{0}^{N} b^n - 1 = b\left(\sum_{0}^{N} b^n - b^n\right) \tag{2.33}$$

Rearranging,

$$\sum_{0}^{N} b^n (1-b) = 1 - b^{n+1} \tag{2.34}$$

$$\sum_{0}^{N} b^n = \frac{1-b^{n+1}}{1-b} \tag{2.35}$$

Thus, the photoemission intensity for a solid composed of N atomic planes is

$$\frac{dI_T(\vec{r})}{dad\Omega} = c\frac{1}{k}s\frac{d\sigma}{d\Omega}e^{-\frac{a}{2\lambda\sin\theta}}\sum_{0}^{N}\left(\frac{1-e^{-\frac{(n+1)a}{\lambda\sin\theta}}}{1-e^{-\frac{a}{\lambda\sin\theta}}}\right) \tag{2.36}$$

When the material conforms a multilayered material, we need to take another consideration. If the emitting layer has more layers on top, the photoelectron will travel through them, hence the latter equation needs to be multiplied by the probability of no collision the photoelectron will have while travelling the subsequent layers on top. The approximation used to quantify the intensity attenuation caused by the layers on top is the Beer-Lambert factor given by

$$e^{-\int_0^d -\frac{dz}{\lambda\sin\theta}} \tag{2.37}$$

Here we have redefined d as layer thickness and integrating over this thickness we obtain the expression for the photoemission intensity of a material with layers on top:

$$\frac{dI(\vec{r})}{dad\Omega} = c\frac{1}{k}s\frac{d\sigma}{d\Omega}e^{-\frac{a}{2\lambda\sin\theta}}\left(\frac{1-e^{-\frac{d}{\lambda\sin\theta}}}{1-e^{-\frac{a}{\lambda\sin\theta}}}\right)\prod_{j=1}^{L}e^{-\frac{d_j}{\lambda_j\sin\theta}} \tag{2.38}$$

Where d is the emission layer thickness that often tends to infinity and d_j is the thickness of the L layers on top of the emission layer.

It is possible to consider that the measured material is continuous, this means that when the distance between atomic planes a is much less than the effective attenuation length $a/\lambda << 1$, then the following Taylor expansion is valid:

$$1-e^{-\frac{a}{\lambda\sin\theta}} = 1-\left(1-\frac{a}{\lambda\sin\theta}+\ldots\right)\approx\frac{a}{\lambda\sin\theta} \tag{2.39}$$

This leads, when $\rho = s/a$, to the final expression for a continuous multilayered system photoelectron intensity:

$$\frac{dI(\vec{r})}{dad\Omega} = c\frac{1}{k}\frac{a\sigma}{d\Omega}\rho\lambda\sin\theta\left(1-e^{-\frac{d}{\lambda\sin\theta}}\right)\prod_{j=1}^{L}e^{-\frac{d_j}{\lambda_j\sin\theta}} \tag{2.40}$$

2.3 Previous Work

This thesis work deals with the quantification of the Co 2*p* photoemission spectra. There are several reports using XPS as an analysis technique of Co under different chemical environments that go far to late 1960's with the works of Fadley and Shirley[50] and other reports in the 1970's.[51–54] However the information extracted is of qualitative character.

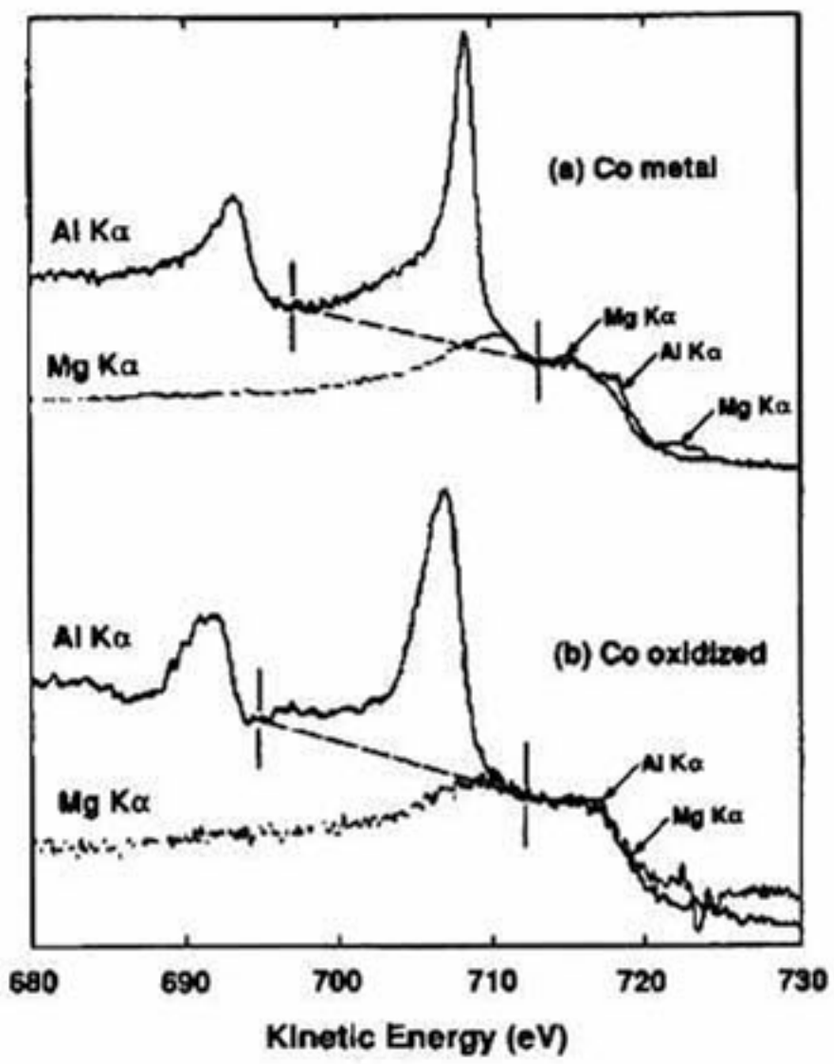

Figure 2.7 Co 2p photoelectron spectra obtained with Al Kα excitation and with the Auger superimposed spectra with Mg Kα radiation for a) metallic cobalt and b) cobalt oxide. Taken from Ref.[7].

One of the most common X-Ray sources is the Al $K\alpha_1$ radiation, but in the XPS analysis of Co Auger LMM lines have a strong interference with the Co $2p_{3/2}$ photoemission peak. Farr and Griesser[7] measured the Auger contribution to the spectra and estimated about 15% errors in peak area calculations if the Auger lines are not considered, but peak fitting was not performed and the precise peak contributions were not determined. Although the situation can be solved using a Mg X-Ray source or even synchrotron radiation, it is necessary to accurately determine the Auger contributions using Al $K\alpha_1$ radiation in order to able to compare quantitative studies performed in different XPS tools. These results are shown in Figure 2.7 where a linear background subtraction is employed.

One of the first studies of a metallic Co thin film and its oxidation by oxygen exposure was done by McIntyre et al.[55] in the early 1990's; peak fitting was performed and satellite structures were identified in the spectra of CoO and Co_3O_4. Several reports[56–59] have identified a satellite peak in the O 1*s* spectrum, the nature of the two peak or satellite features in the O 1*s* spectra of cobalt oxides has been explained to be caused by structural defects or a surface effect that causes a loss in the covalency of the bond. The evolution of this peak is shown in Figure 2.8 alongside the Co 2*p* spectra.

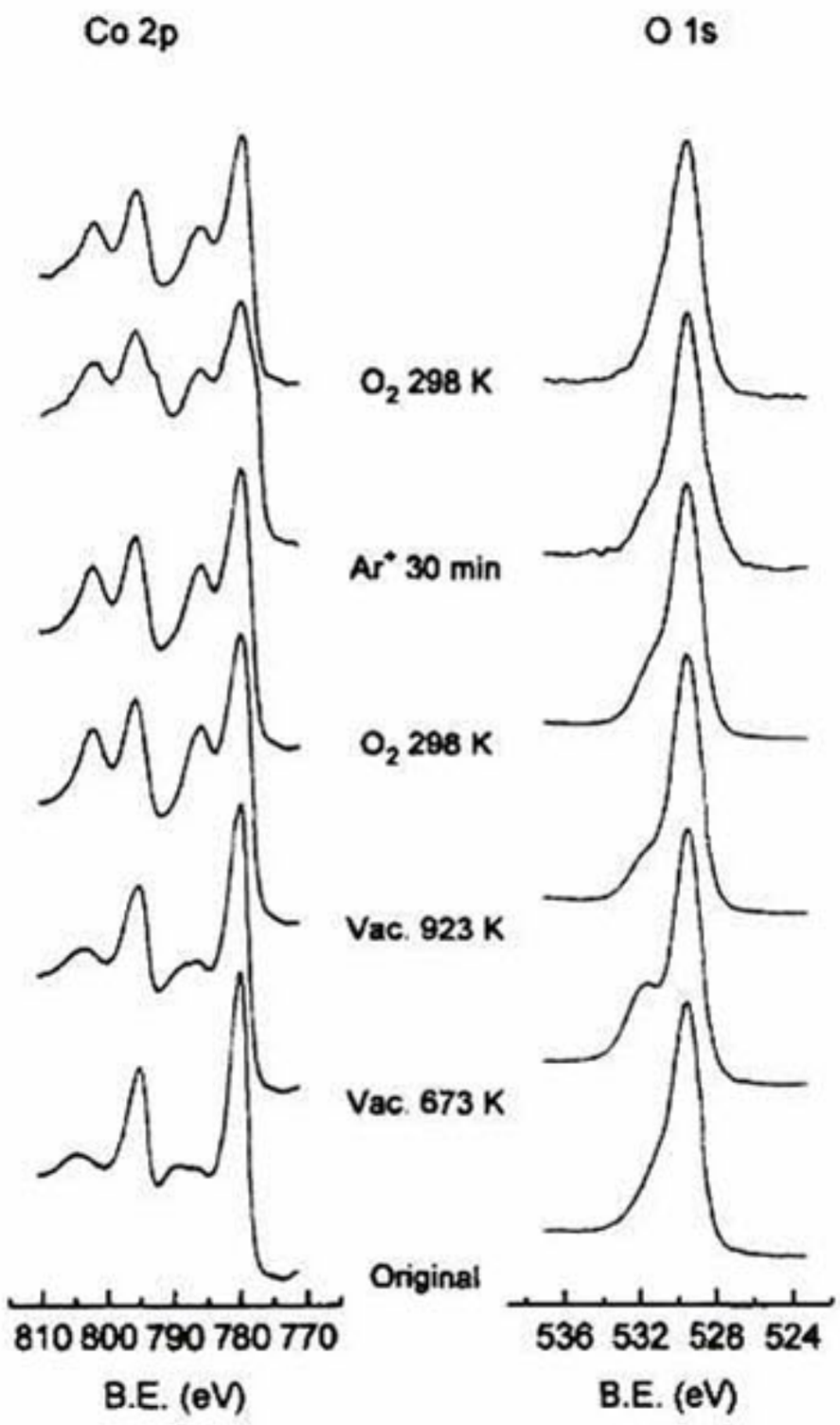

Figure 2.8 O 1s and Co 2p spectra of Co_3O_4 submitted to different heat treatments and Ar^+ bombardments. Taken from Ref.[59].

The true nature of satellites in the photoemission spectra of Co [53,60–63] still remains an open question. Even though that from the inception of XPS as a surface analysis technique, several explanations have been developed.[64–66]

The satellite feature in the metallic Co 2*p* spectra has been treated as a plasmon-loss as indicated by the experiments performed by Grosvenor et al.[67] and the peak fitting procedure issued by Biesinger et al.[6] The results are shown in Figure 2.9. Sharma et al.[2] also adds an additional peak to the spectra to accurately reproduce experimental data. Inspite of the close fits they obtain, the peak fitting procedure is only performed in the Co $2p_{3/2}$ photoemission branch and the loss of information, from a quantitative standpoint, is possible even though that for the purpose of their work, the peak fitting performed worked successfully.

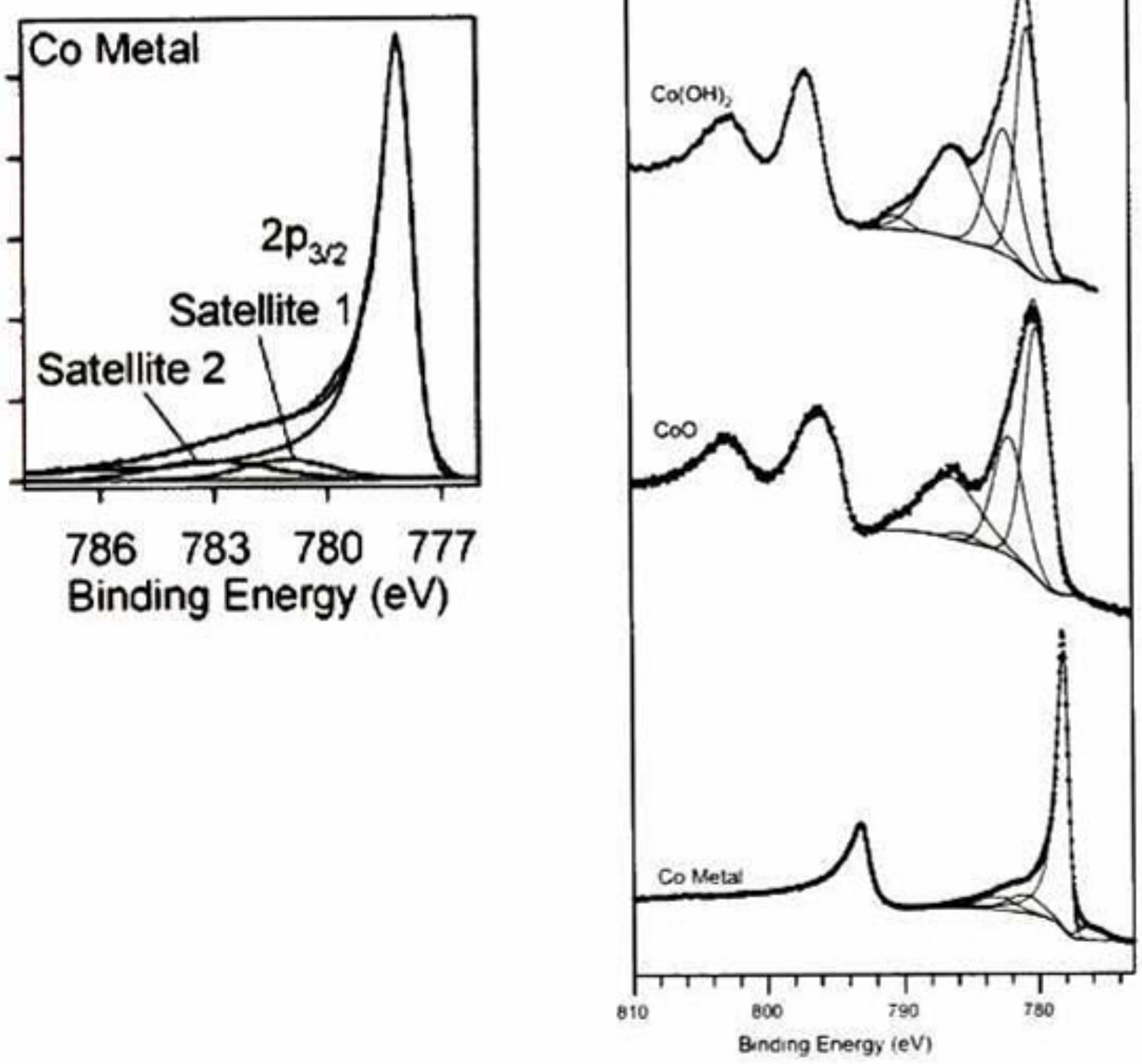

Figure 2.9 Co $2p_{3/2}$ XP spectra of cobalt and cobalt compounds. Taken from Ref.[6,67].

The explanation of satellite features in the photoemission spectra of cobalt oxides has been more successful. Cluster model calculations[68,65,69] have been employed to predict satellite peaks that originate from a crystal field effect that enables strong electron correlations between valence electrons and final core hole states.

Chapter 2. Background

Key aspects of the Co 2*p* photoemission spectra that remain unresolved is the peak contribution to the Auger LMM structure, the nature of the metallic Co satellite features, XPS data quantification accompanied of peak area uncertainties and an accurate determination of the background intensities.

3 *Experimental Procedures*

3.1 Equipment

All the experiments presented in this work were performed in the experimental setup observed in Figure 3.1. It consists of an XPS tool equipped with a loading chamber conditioned for thin films deposition.

The XPS tool is a VG-Thermo-Fisher instrument (Thermo Fisher, East Grinstead, UK). The main components are a VG Scientific Standard Mono Analysis Chamber, a seven-channel hemispheric detector electron analyzer model XPS110 operated in the MONOXPS lens mode with an acceptance angle of 16° and a monochromatized Al Kα X-Ray source model XR5/55. There exists an angle of 41°between the incident X-Ray beam and the electron analyzer axis.

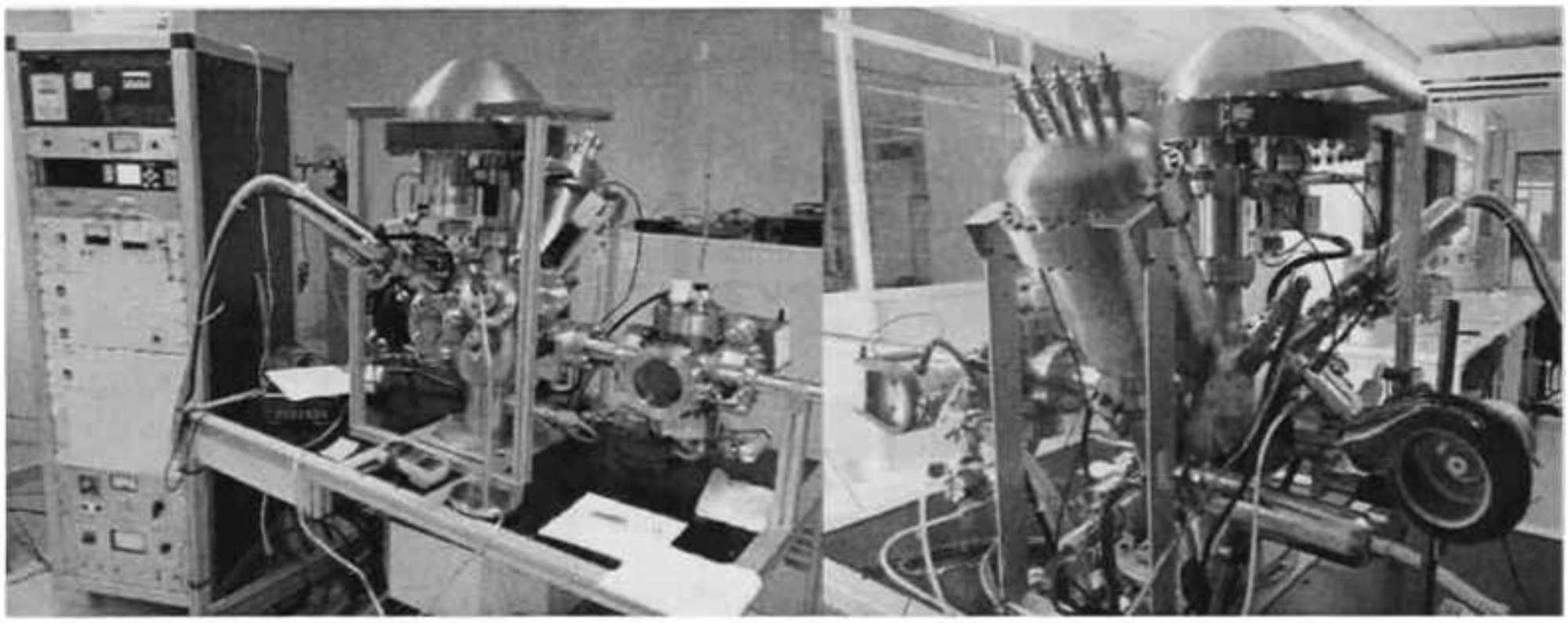

Figure 3.1 Experimental set-up used for XPS analysis and thin films deposition.

One of the most important aspects involving a film deposition and a XPS measurement is the conservation of vacuum. In this sense, the XPS tool and loading chamber are interconnected. Vacuum in the last, is achieved by means of an Adixen DRYTEL 1025 roughing pump and an Adixen ATP 80 turbomolecular pump from which pressures in the order of 10^{-4} and 10^{-8} Torr are respectively acquired.

At the XPS analysis chamber, pre-vacuum is achieved rough pumping with the vacuum system located in the loading chamber and the establishment of ultra-high

vacuum is obtained with the use of a RIBER Model 401_1000 ion pump and a RIBER Model 304 titanium sublimation pump. The pressures enabled by this system are in the order of 10^{-11} Torr.

3.2 Thermal Evaporation of Cobalt

Cobalt thin films were deposited in the loading chamber. Deposition is achieved taking advantage of the Joule heating effect that arises from the circulation of current through a metal coil. With the released heat, under the loading chamber pressure, cobalt melts and then evaporates generating a vapor that deposits onto a substrate producing a thin film. A sketch of thermal evaporation can be found in Figure 3.2, also a picture of the metal coil-cobalt arrangement is shown.

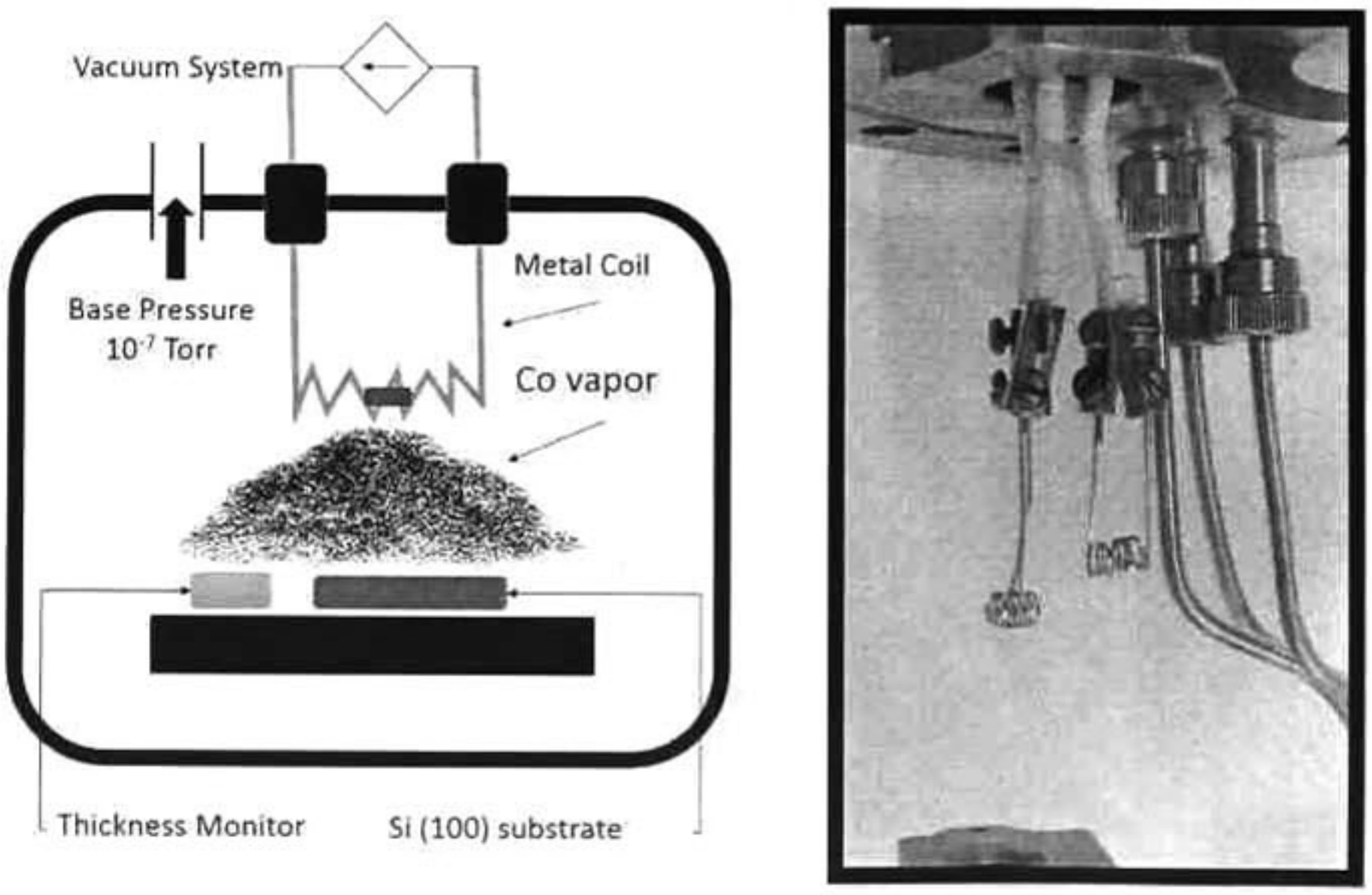

Figure 3.2 Sketch of the thermal sublimation process and the arrangement of filament thermal sources.

The metal coil can also be called a filament and in this work Tungsten (W) and Zirconium (Zr) were employed as filaments. The use of this metals is due to their high melting point compared with Co, however Co alloys with refractory metals, making this operation to be dealt with extreme care when applying an electrical current to the filament.

The substrate used in the film deposition was Si (100). A standard cleaning procedure consisting of subsequent ultrasonic baths in acetone, methanol and isopropyl alcohol were applied in order to degrease the surface of the wafer, also RCA clean[70] was used to remove any contaminants from the surface.

The evaporation of cobalt was controlled with a current source Xantrex XFR 150-18 DC Power Supply, making a sweep in applied current to the filament from 0 to 15.1 A. At the same time, estimation of the film thickness, with a piezoelectric monitor Maxtek Thickness Monitor Model TM-350/400, was held. The base pressure in the loading chamber at the moment of deposition was $2.1x10^{-7}$ Torr.

Problems regarding the melting of the filament arose in the evaporation operation with both coils; electric current in the chamber was not precisely controlled and for the W filament a 20nm film was deposited, while the Zr coil permitted the deposition of a 21nm film until breakdown. Despite this facts, it was possible to perform the chemical characterization of the films.

3.3 Oxidation of Thin Films

Cobalt oxides were formed regulating the exposure of the metallic film to an oxygen atmosphere. Control over this process was issued measuring Langmuir ($1L \equiv 10^{-6}$ Torr sec) as a unit of pressure and time.

With the film deposited using the W coil, oxidation was reached at 400GL. Oxidation of the film obtained with the Zr filament was achieved in atmospheric pressure at 823K during 5 minutes. Impurity oxides were obtained keeping an oxygen dosage in intervals of one order of magnitude per stage of oxidation at 21±2°C of temperature. The oxygen employed was ultra-high purity grade provided by Infra.

3.4 The XPS Measurement

The XPS data was taken with a monochromatized Al Kα X-Ray source measuring the Co 3p and the complex 2p region. High resolution spectra consisted of measurements with 10 eV as pass energy, having take-off angles of 90° The O1s

and C1*s* regions were also scanned utilizing high resolution spectra; this in order to produce data for chemical quantification of the film upon oxidation. Traces of the thermal sources appeared on both spectra; W in the film could not be accurately distinguished from noise, but for the Zr deposit, the Zr 3*d* and Zn 2*p* regions were analyzed. The film's compositional depth profile was assessed in the metallic and full oxidation stage applying ARXPS technique with take-off angles of 85°, 65°, 45° and 35°. Pressure in the analysis chamber was kept at 1E10^{-9} Torr.

3.5 Data Analysis

The correct evaluation of the XPS data produced is one of the most important aspects in this thesis. A correct curve fitting process enables us to determine every hidden contribution within a certain spectrum. Thus, permitting the true assessment of the material analyzed.

As it was commented before, the XPS spectrum, especially in metals, has many complex contributions that may lead to inconsistent results and the data analysis methodology used is a key factor associated to the discrepancy in results among different curve fitting methods[71,72]

The XPS spectrum may be considered as a function, that in order to extract information it must be deconvoluted. In some cases, especially dealing with compounds with relative small proportions, the overlapping peaks may not be resolved using a traditional method like the Fourier Transform technique[73,74]. A way to solve this issue, is to perform deconvolution via an iterative algorithm[75,76].

Another way to determine peak parameters is through the generation of data sets from ARXPS, in which peak shape changes correlated with angle may help discriminate the contributions and parameters of the XPS spectra. But, because of the lack of peak fitting standards, the use of methods like the sequential fitting, averaged method and sum of the data for all angles fitting does not accurately solve the problem[77]

3.5.1 Peak Fitting Method

Approach to a robust curve fitting process of XPS data is performed with the software AAnalyzer®. This program uses the Method of Least Squares as the maximum likelihood estimator for peak parameters and the Levenberg-Marquadt Method to search for the optimal values that correctly fit a peak envelope to the experimental data.

The fitting process optimizes a set of parameters $\{a_1,...,a_M\}$ that completely characterize a synthetic spectrum. These include intensity, position, background and line-shape specific variables.

The parameter optimization is based on making the synthetic spectrum accurately reproduce experimental data by means of the minimization of χ^2 as defined as:

$$\chi^2 = \sum_{i=1}^{N}\left(\frac{I_i - I(E_i;a_1,...,a_M)}{\sigma_i}\right) \qquad (3.1)$$

Where I_i is the experimental intensity at a certain energy E_i, σ_i is the intrinsic standard deviation and I is an intensity at energy E_i defined by previously assumed true parameters that characterize the synthetic spectrum.

This software in general terms deals with ARXPS data by fitting the spectrum for each angle simultaneously, taking into account the shared parameters hypothesis in terms of peak center and width[77].

AAnalyzer® has the capacity to convolute different line profiles such as Gaussians and Lorentzians; this permits the fitting to experimental data of an array of functions; such as a Voigt function and the double-Lorentzian line-shape, which is one that is integrable and with low uncertainty describes peak asymmetries encountered in the spectra obtained from metals[45]

Background modeling is done by means of the active method, which consists of enabling the background to be composed of different background types[12] The background profiles in this software are a base-line, n^{th} order polynomial, Shirley-Proctor-Sherwood (SPS) background[46,49], Shirley-Végh-Salvi-Castle (SVSC) background[78–80] and a Tougaard[81] type background called the Slope background[82].

The known parameter introduced in the experimental data modelation, is the branching ratio, which is one corresponding to the ratio between the subshell photoelectric cross sections of the *j=1/2* and *j=3/2* branches respectively. Values for these and subshell parameters are found elsewhere[29,83].

3.5.2 Calculation of Uncertainties

Uncertainties are calculated assuming Poisson statistics, requiring that data must be treated in total counts, which means that normalized data in counts/s is multiplied by the acquisition time (dwell time) and the number of scans used to produce the spectrum. For the XPS tool used the dwell time has a value of 0.2s. The number of scans are 20 for the Co 2*p* region, 25 for the Co 3*p* region, 35 for the Zr3*d* region and 20 for the O1*s*, C1*s* and Zn2*p* region.

Having the latter into consideration, it is assumed through the peak fitting process that the set of parameters $\{a_1,...,a_M\}$ at an energy E_i are true and correctly reproduce the experimental data. Then a curvature matrix is constructed following Equation (3.2)[13]:

$$\alpha_{k,l} = \frac{1}{2}\frac{\partial^2 \chi^2}{\partial a_k \partial a_l} \approx \sum_{i=1}^{N} \frac{1}{\sigma_i^2} \frac{\partial I(E_i;\mathbf{a})}{\partial a_k} \frac{\partial I(E_i;\mathbf{a})}{\partial a_l} \tag{3.2}$$

With the result, the covariance matrix is defined in terms of the curvature matrix as follows:

$$C \equiv \alpha^{-1} \tag{3.3}$$

Which happens to give the parameters' uncertainty with the next relation:

$$\Delta a_k = \sqrt{C_{k,k}} \tag{3.4}$$

The software AAnalyzer® uses this procedure to calculate uncertainties in terms of standard deviations. Having these interval for each parameter, it is possible to propagate the peak area uncertainty to the subsequent film compositional analysis.

3.5.3 Quantification

Quantification in terms of structure and composition of the films was assessed using a multilayer model[84] Peak normalization is used to eliminate the need for

geometrical factors in quantification. The strong assumption in this approach is that the electron transport parameters through the layered film are well known alongside the depth distribution of the substrate; therefore the model has strong restrictions and results comply under this consideration.

The multilayer model is fed of standardized effective attenuation lengths that were obtained from the NIST Standard Reference Database 82[85].

The methodology applied to assess the film composition consists of using a reference peak from which all other peaks will be normalized. The product of normalization will be the reference that the multilayer model is fitted to, through the minimization of relative errors as expressed in Equation(3.5):

$$R_{err} = \sum_{n=1}^{N} \left[\frac{A_n}{A_{RP}} - \frac{T_n}{T_{RP}} \right]^2 \tag{3.5}$$

Here R_{err} is the relative intensity error, A_{RP} is the reference peak area values obtained from fitting of experimental data, T_{RP} is the multilayer model theoretical reference peak area values constructed from thickness and composition parameters and finally A_n and T_n correspond to peak area values, satisfying the same criteria, but for the remaining peaks included in the peak envelope.

The relative intensity error minimization is achieved using the Generalized Reduced Gradient Method varying values for film thickness and atomic density for each chemical species according to several proposed film structures. The correct assessment is considered to be when stoichiometry and a minimum in relative errors comply.

Important to say is that the last is an indicative of how well the multilayer model reproduces the relative peak intensities and the composition interval corresponds to an error propagation from peak area uncertainties right to a composition interval.

4 Results

In this section the XPS spectra obtained from the Co metallic film and subsequent spectra corresponding to the film oxidized states are presented. The information obtained corresponds to the deconvoluted peak values for binding energies (BE); spin-orbit splitting (SOS), that is the BE difference between the *j=3/2* and *j=1/2* photoemission branches; peak widths and double-Lorentzian (DL) asymmetry. Quantitative analysis is based on a multilayer model scheme computing the resulting fitted peak areas.

4.1 The Cobalt Deposition Result

Upon performing a thermal evaporation with coils (W and Zr) Co presents much difficulties while setting a deposition rate and specially in producing films surpassing the 20nm mark. The deposition system fails by forming alloys at 13 and 5A for the W and Zr coils respectively. This enables the deposition of only 20nm films until the system breaks down.

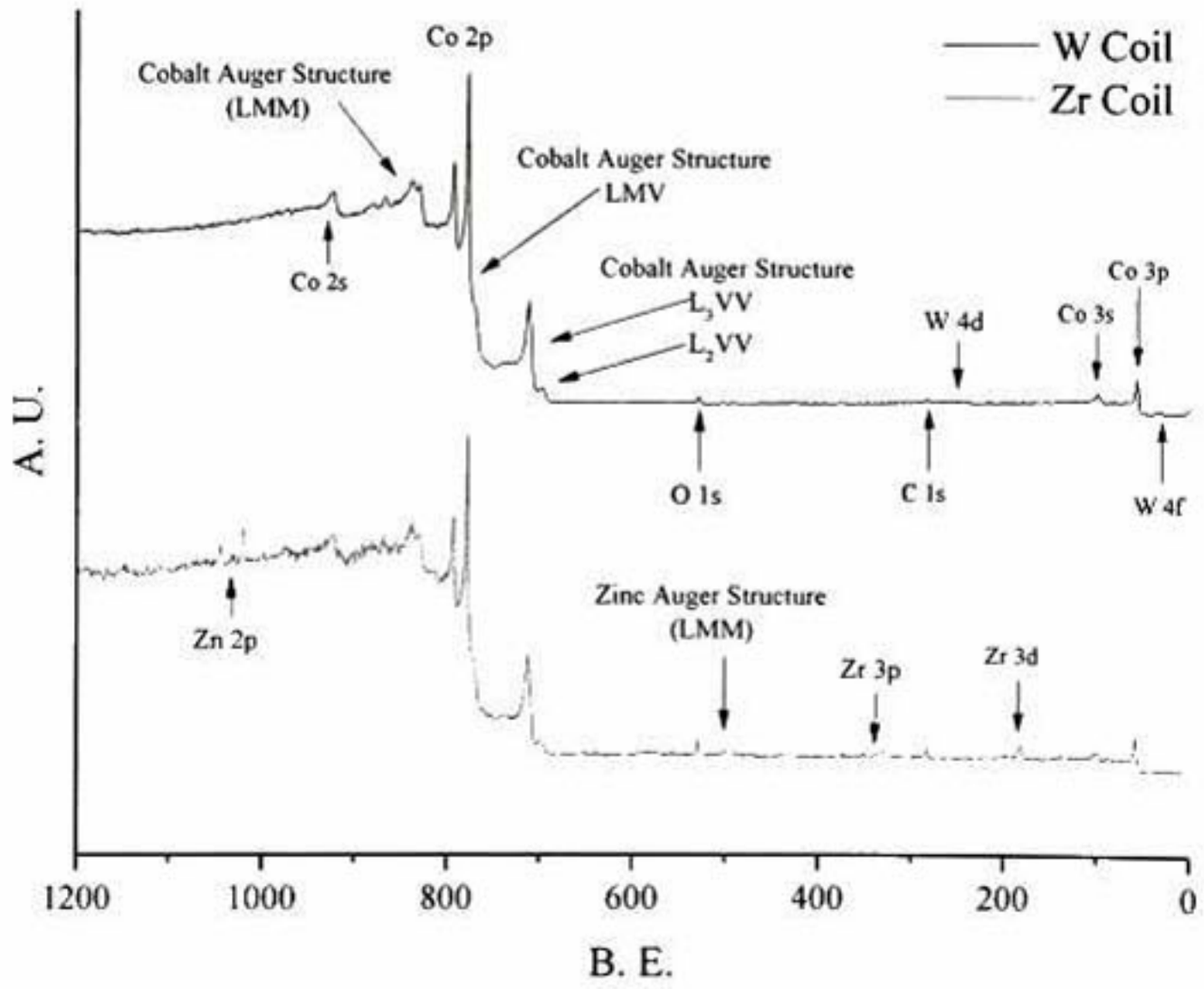

Figure 4.1 Wide scan spectra of Co metallic films obtained from W and Zr Coil thermal evaporation.

A qualitative analysis may be performed using the wide scan spectrum obtained from the metallic films shown in Figure 4.1. It can be seen that for the W coil deposition, a relatively pure metallic film is obtained with impurity signals that cannot be distinguished from noise. For the Zr coil deposition, impurity signals corresponding to Zr and Zn appear in the spectrum, that in terms of relative intensity, these have to be accounted more rigorously.

4.2 The Metallic Cobalt X-Ray Photoemission Spectra

The metallic film XPS analysis is performed producing high resolution (10 eV of pass energy) spectra of the Co 2*p* and 3*p* region.

In Figure 4.2 the Co 2p XPS spectrum of both coils is shown together with normalized spectra. By comparison, a slight difference between these can be noticed at the point where the background contribution is more intense; meaning that the Co signal per se is the same for both coils. Peak parameters are presented in Table 4.1; this correspond to the ones obtained for the W coil deposit and later fitted to the Zr coil spectrum; where only the background parameters happen to differ for the two deposition coils used.

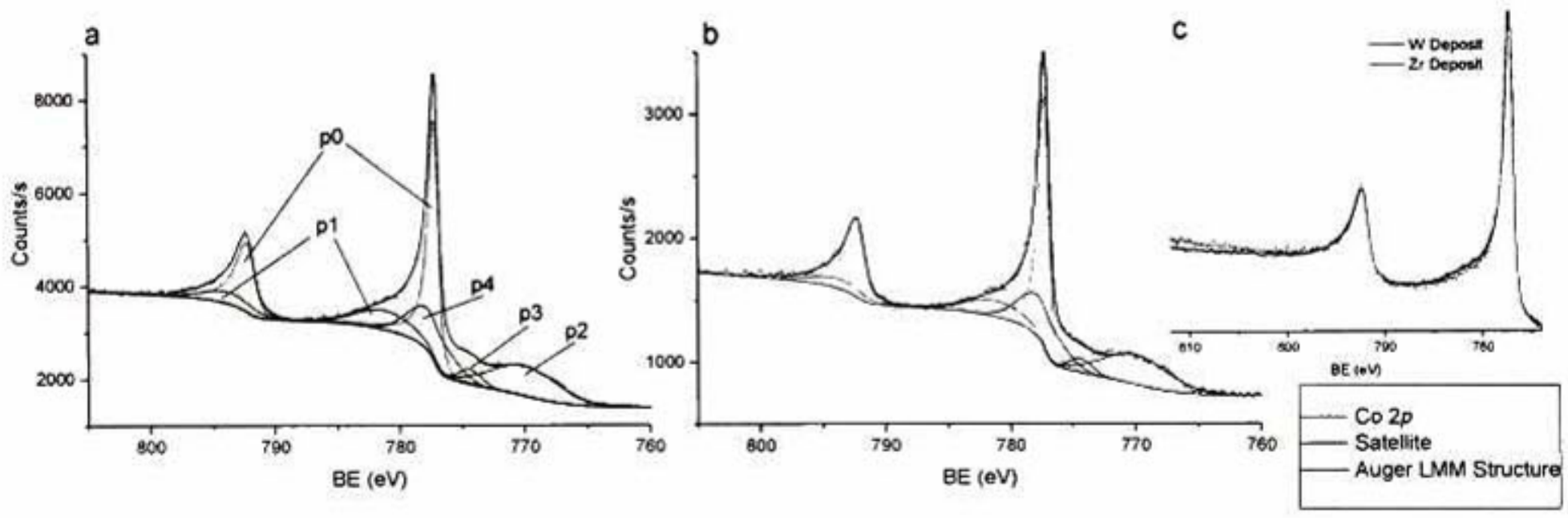

Figure 4.2 Co 2p XPS spectrum produced with a a) W coil evaporation of Co and b) Zr coil evaporation of Co; c) shows a comparison between these in terms of a normalized spectrum.

Peak parameters corresponding to the Zr deposit are obtained from ARXPS spectra shown in Figure 4.3. Through the simultaneous peak fitting performed, the shape parameters found correspond to the same as the previous ones; it can be seen that the Co 2*p* signal has no modulation across a depth profile, meaning that the film is in fact metallic Co. Same parameters indicate that the set obtained from two different

samples with different chemical environments, but containing Co metal are the ones that define the metallic Co 2*p* XPS features.

Table 4.1 Peak Parameters of the Co 2p XPS region according to data in Figure 4.2.

Peak	***$2p_{3/2}$ BE eV***	***SOS eV***	***Peak Width***		***double-Lorentzian Asymmetry***	***Line-shape***
			Gaussian eV	*Lorentzian eV*		
p0	777.10	-14.96	0.436	0.386 0.789[a]	2.910 2.964[a]	double-Lorentzian
p1	781.16	-12.57	5.413 4.628[a]			Gaussian
p2	770.08		6.330			Gaussian
p3	774.40		2.181			Gaussian
p4	777.63		3.951			Gaussian

Background Parameters	*Shirley type Background*		*Slope*	
	SVSC	0.0896	*W coil*	*Zr coil*
			7.1e-05	1.8e-04

a Denotes the corresponding value for the $2p_{1/2}$ branch.

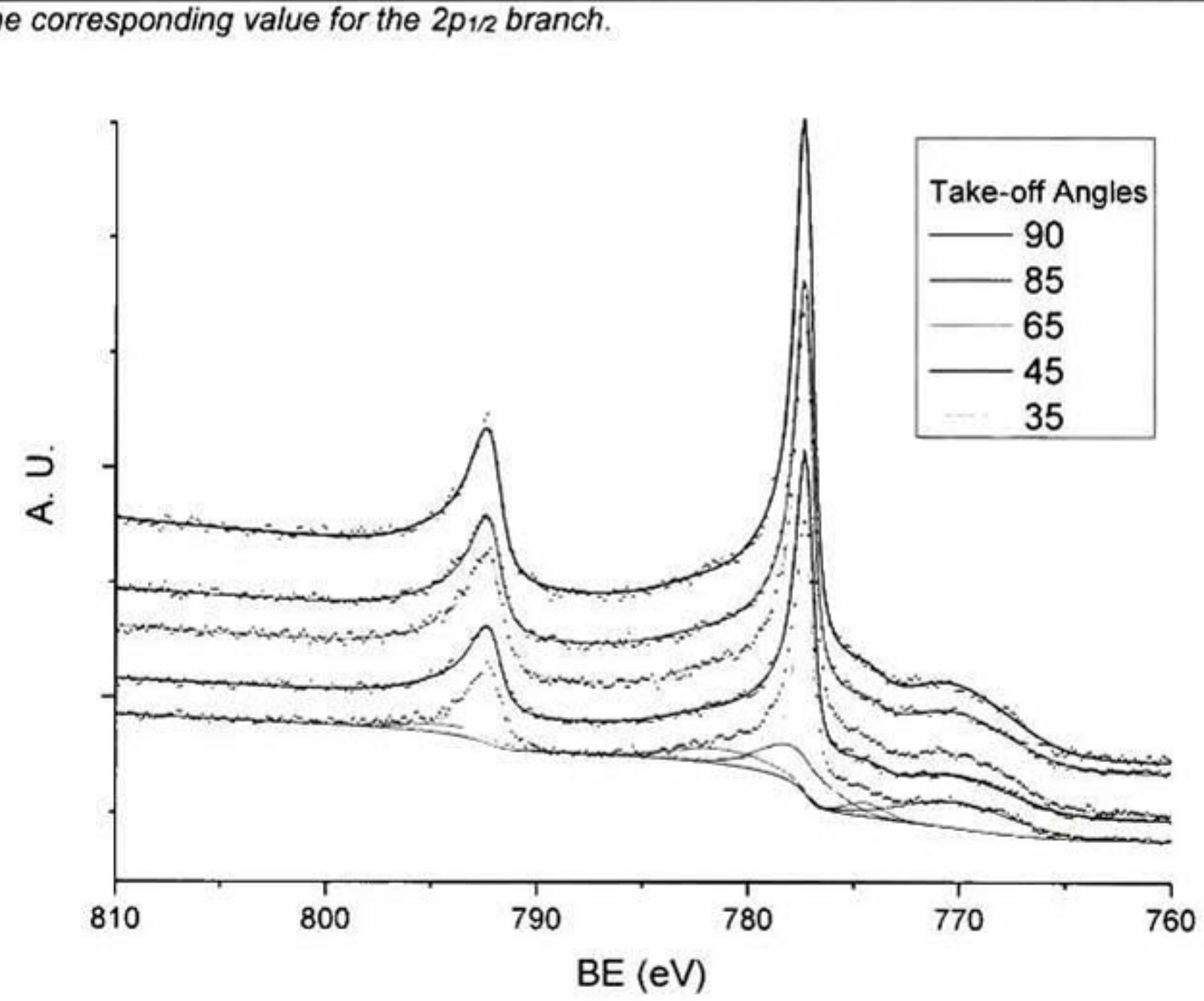

Figure 4.3 ARXPS Co 2p data obtained from the Zr coil thermal evaporation.

The Co 3*p* XPS spectra corresponding to the W coil Co film and the Zr coil angular measurements is presented in Figure 4.4. Parameters are found in Table 4.2. The parameters used to fit to experimental data, indicate that the Co spectra, either measured from a film evaporated from a W or Zr coil, prove to be statistically the same. The spectra does not feature de Auger LMM structure, leading to a far simpler

spectrum to fit. Also, background modelation is achieved, instead of using a SVSC type background, a SPS type background is used in both cases.

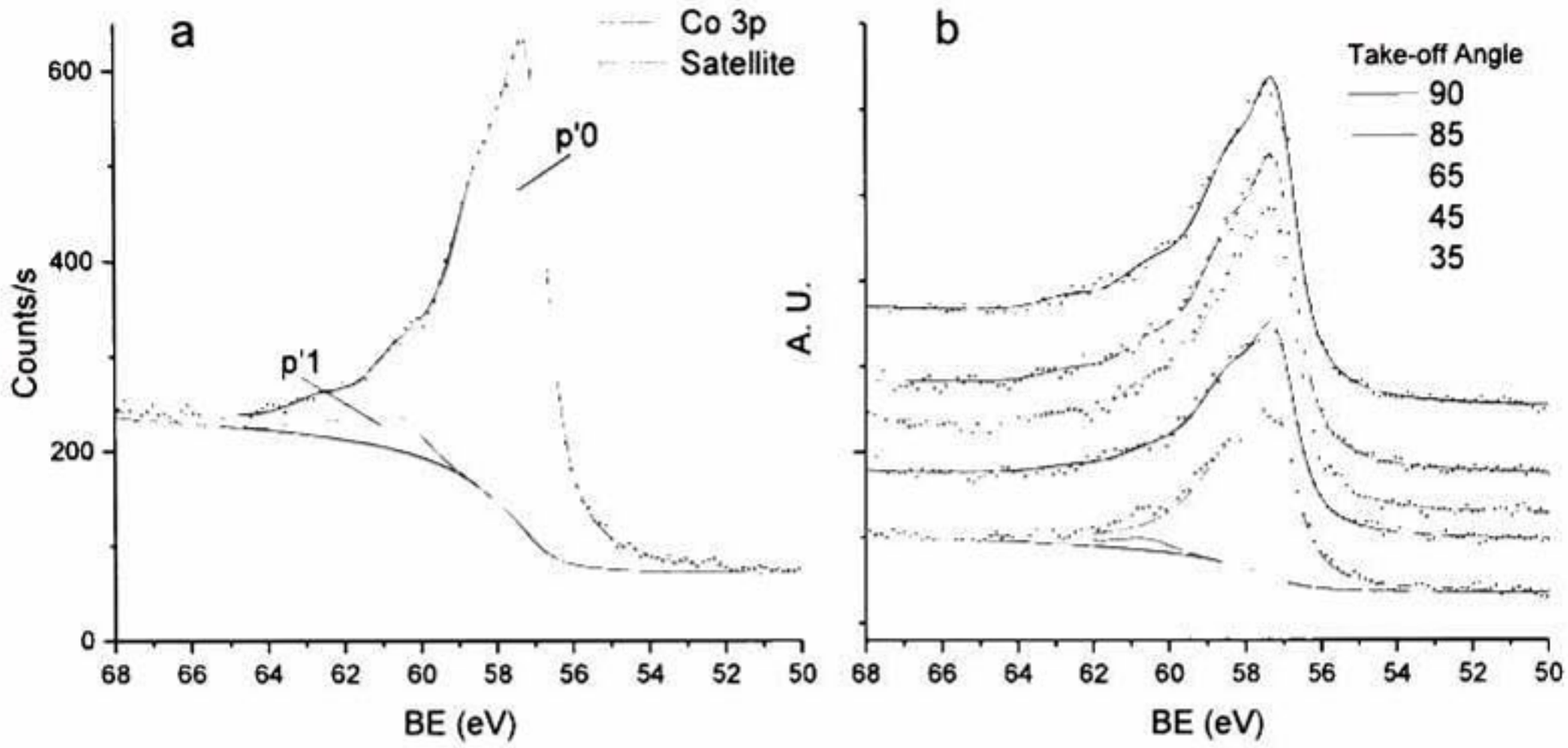

Figure 4.4 Co 3p XPS spectra obtained from a) W coil evaporation and b) ARXPS measurements for the Zr coil evaporation.

Table 4.2 Peak Parameters of the Co 3p XPS spectra according to data in Figure 4.4.

Peak	***3p3/2 BE eV***	***SOS eV***	***Peak Width*** *Gaussian eV*	*Lorentzian eV*	***double-Lorentzian Asymmetry***	***Line-shape***
p'0	57.16	-1.32	0.511	0.997 1.345[a]	1.786 1.752[a]	double-Lorentzian
p'1	60.65	-1.92	1.612 1.755[b]			Gaussian

Background Parameters	*Shirley type Background*		*Slope*	
	SPS	0.08866	*W coil*	*Zr coil*
			4.6e-04	4.4e-04

b Denotes the corresponding value for the $3p_{1/2}$ branch.

4.3 The Cobalt Oxides XPS Spectra

The Cobalt(II) oxide photoemission spectrum is determined through a partially oxidized film that features the Co metal XPS characteristics. In this sense, Figure 4.5 shows the Co 2*p* region of the partially oxidized film, in which metallic Co peak parameters, previously obtained, have been introduced and oxide parameters have been determined through fitting. Peak parameters are shown in Table 4.3. The corresponding O1*s* spectrum is presented in Figure 4.6. It features two discernible oxygen peaks with peak parameters found in Table 4.4.

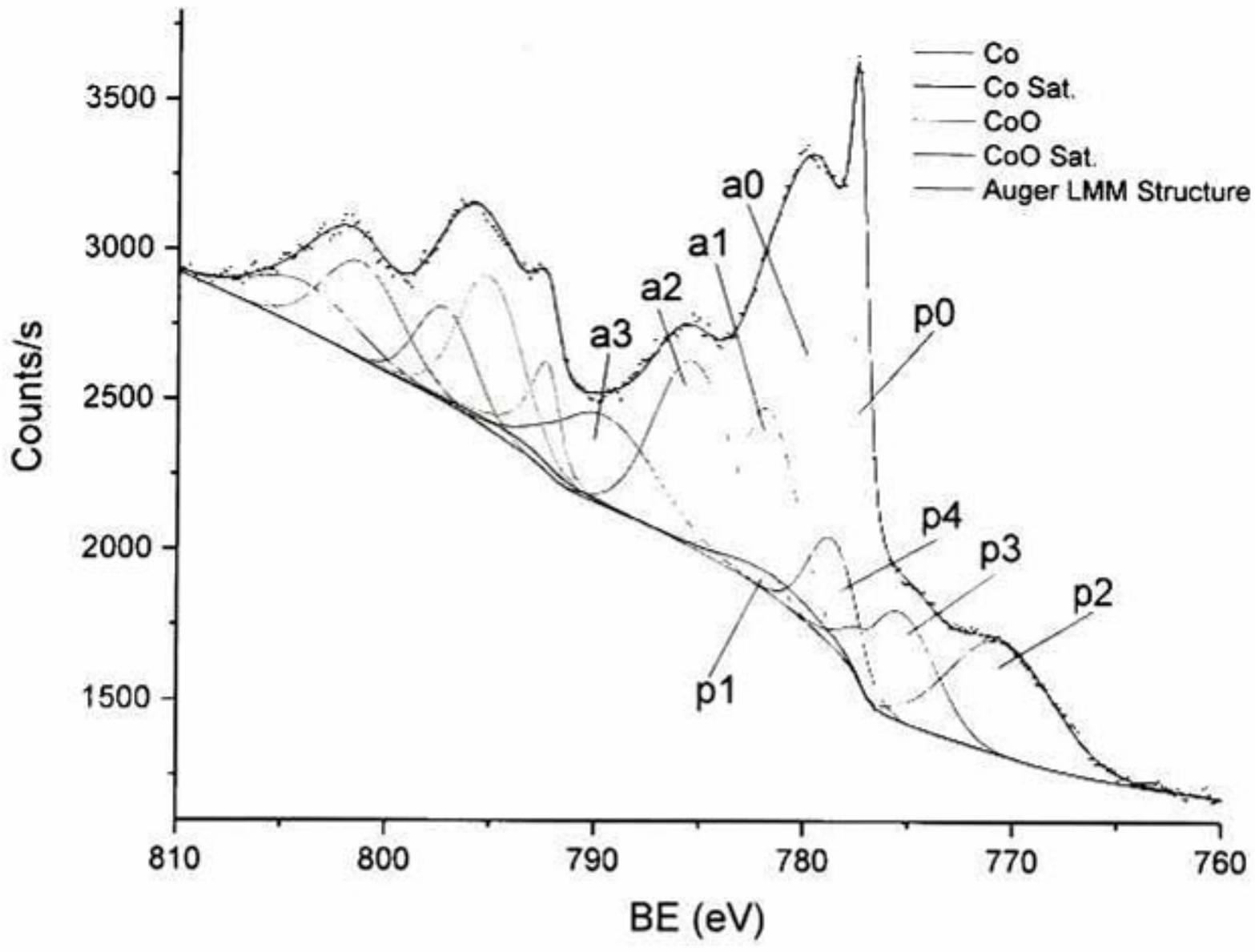

Figure 4.5 Co 2p XPS spectrum for a partially oxidized Co film.

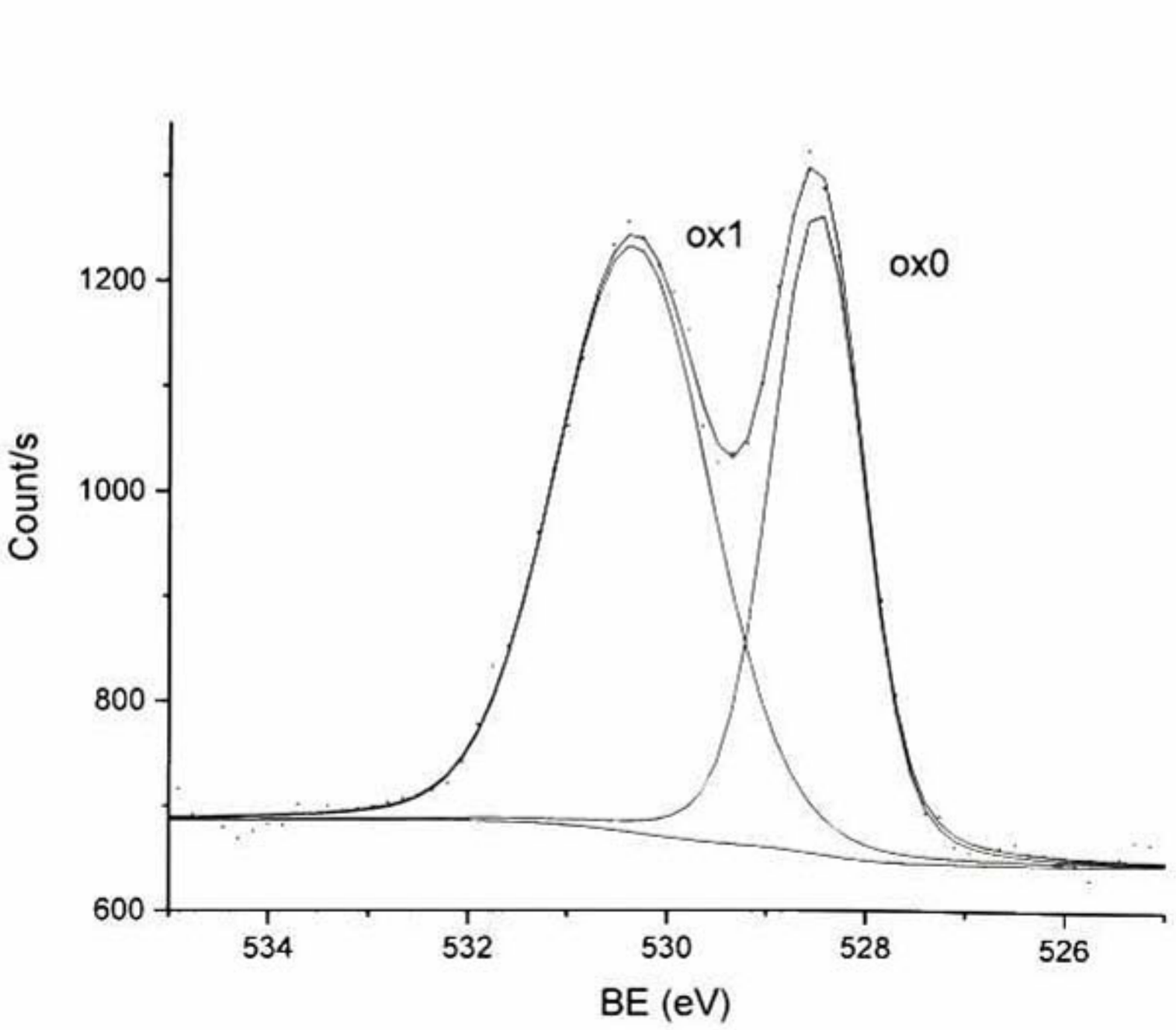

Figure 4.6 O 1s spectrum obtained from a partially oxidized film having CoO. Two peaks are observed because of the presence of polycrystalline cobalt oxide.

Table 4.3 Peak parameters for the partially oxidized Co 2p spectrum in Figure 4.5.

Peak	***2p3/2 BE eV***	***SOS eV***	***Peak Width***		***double-Lorentzian Asymmetry***	***Line-shape***
			Gaussian eV	*Lorentzian eV*		
a0	779.41	-15.56	3.284	0.449		Voigt
a1	781.67	-15.50	3.259			Gaussian
a2	785.25	-15.91	4.450			Gaussian
a3	789.58	-14.35	5.795			Gaussian
p2	770.57		5.828			Gaussian
p3	775.37		3.945			Gaussian
p4	778.57		2.772			Gaussian
Background Parameters			*Shirley type Background*			*Slope*
			SVSC		0.02354	0.0003

Table 4.4 Peak parameters of the O 1s spectrum from a partially oxidized film.

Peak	***BE eV***	***Peak Width***		***Line-shape***
		Gaussian eV	*Lorentzian eV*	
ox0	528.50	0.931	0.25	Voigt
ox1	530.35	1.669	0.25	Voigt
Background Parameters		*Shirley type Background*		*Slope*
		SPS	0.022	-

While producing the full oxidized film at a temperature of 823K, all impurities evaporated leaving a pure Cobalt oxide film. The resultant XPS spectrum is typical of the cobalt(II) dicobalt(III) oxide. The Co *2p* XPS spectra of Co_3O_4 are shown in Figure 4.7; the spectra shows a much less intense satellite feature when it is compared to CoO; also, the oxide peak sharpness characterizes a qualitative fingerprint for the Co 2*p* core level of Co_3O_4.

The corresponding Co *3p* spectra are presented in Figure 4.8. The peak fitting results have more uncertainties with respect to the Co 2*p* results; for the reason that the peak envelope is composed of closely lying peaks with broad intrinsic line widths which are difficult to accurately resolve within the spectra. With these regards, the majority of peak parameters had to be correlated, in order to avoid diverging values with no physical coherence whatsoever.

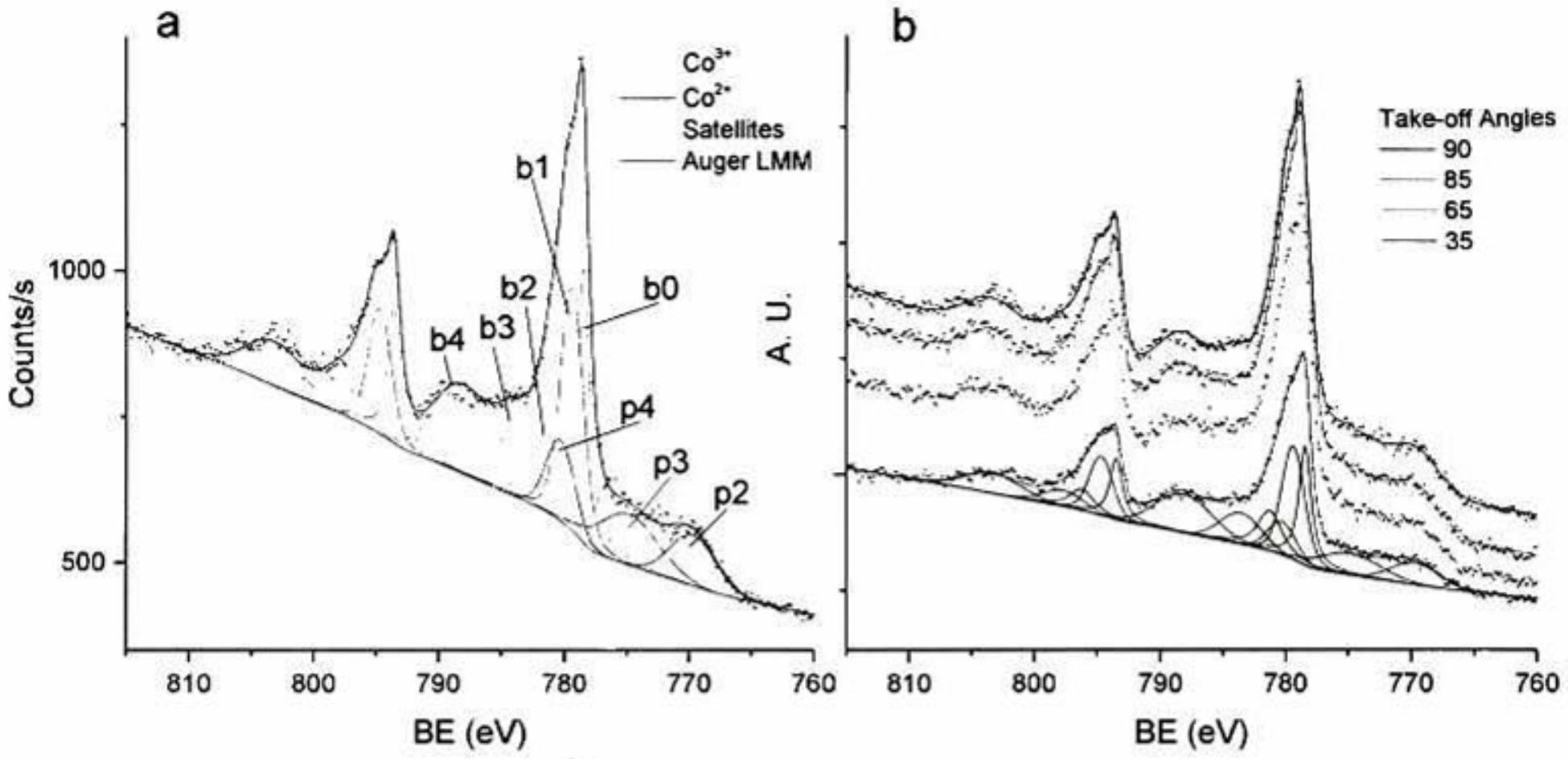

Figure 4.7 Co 2p XPS spectrum corresponding to Co_3O_4. a) Peak identification and b) ARXPS measurement of the fully oxidized film presenting Co_3O_4 homogeneously distributed across depth.

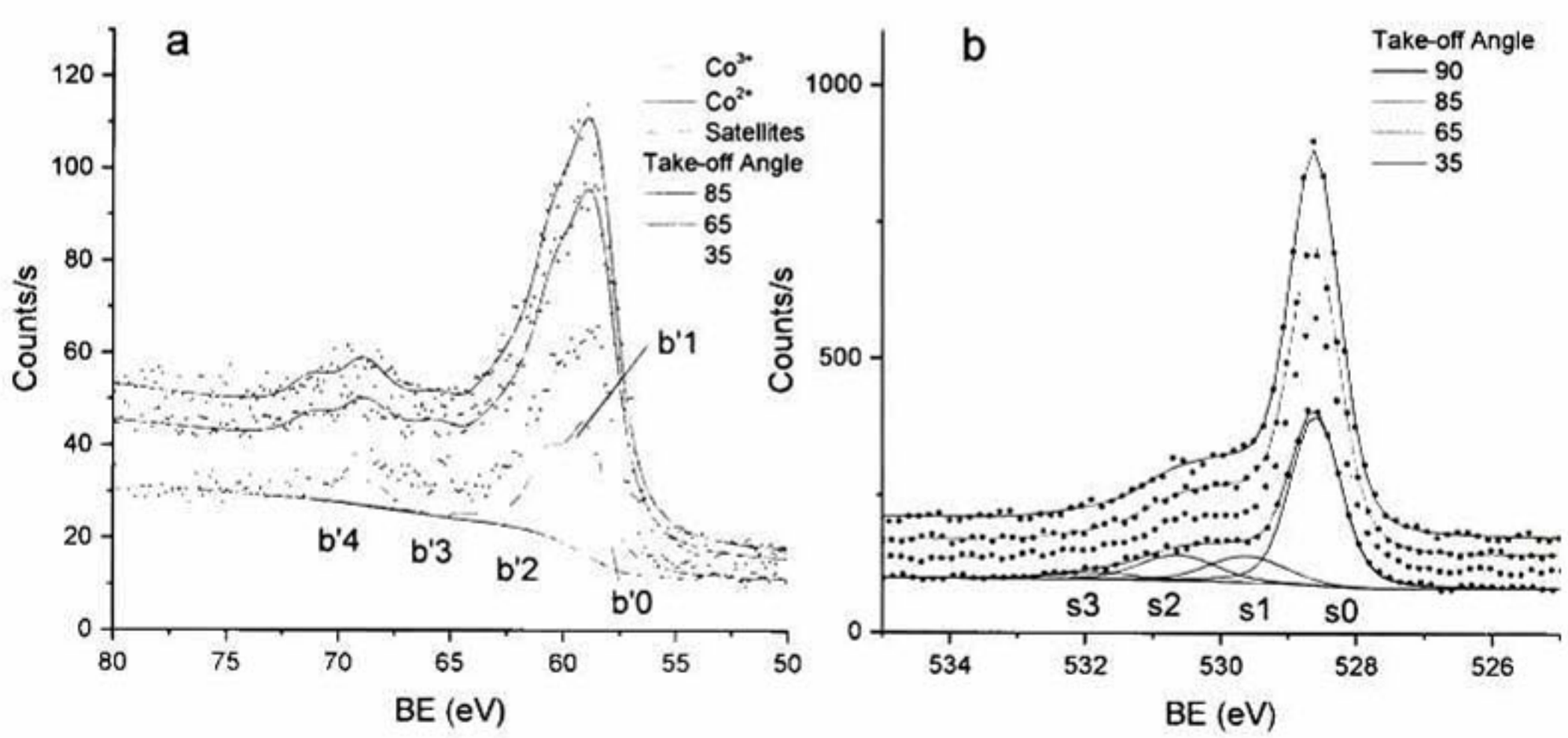

Figure 4.8 a) Co 3p ARXP spectra and b) the O1s ARXP spectra of Co_3O_4.

Observing the O *1s* spectra in Figure 4.8, it can be seen that it consists of three peaks, with an additional peak centered at 531.85 eV that can be attributed to chemisorbed oxygen. Peak parameters for the Co_3O_4 spectra are found in Table 4.5, Table 4.6 and Table 4.7

Table 4.5 Peak parameters for the Co 2p XPS spectra of Co_3O_4.

Peak	***2p3/2 BE eV***	***SOS eV***	***Peak Width***		***double-Lorentzian Asymmetry***	***Line-shape***
			Gaussian eV	*Lorentzian eV*		
b0	778.38	-15.07	0.211	1.101		Voigt
b1	779.35	-15.31	1.859	0.449		Voigt
b2	781.23	-14.95	0.920	1.852		Voigt
b3	783.61	-14.11	3.798			Gaussian
b4	788.16	-15.11	5.272			Gaussian
p2	769.68		4.345			Gaussian
p3	774.85		5.671			Gaussian
p4	780.29		2.727			Gaussian
Background Parameters			*Shirley type Background*			*Slope*
			SVSC	0.0221		0.00021

Table 4.6 Peak parameters for the Co 3p XPS spectra of Co_3O_4.

Peak	***3p3/2 BE eV***	***SOS eV***	***Peak Width***		***double-Lorentzian Asymmetry***	***Line-shape***
			Gaussian eV	*Lorentzian eV*		
b'0	58.21	-1.69	0.932	1.467		Voigt
b'1	58.92	-1.73	0.932	1.467		Voigt
b'2	61.85	-1.34	1.344	1.467		Voigt
b'3	65.52	-1.77	1.344	1.467		Voigt
b'4	68.84	-2.25	1.344	1.467		Voigt
Background Parameters			*Shirley type Background*			*Slope*
			SVSC	0.055		0.00069

Table 4.7 Peak parameters of the O 1s XPS spectrum of Co_3O_4.

Peak	***BE eV***	***Peak Width***		***Line-shape***
		Gaussian eV	*Lorentzian eV*	
s0	528.58	0.716	0.25	Voigt
s1	529.60	1.179	0.25	Voigt
s2	530.62	1.179	0.25	Voigt
s3	531.85	1.179	0.25	Voigt
Background Parameters		*Shirley type Background*		*Slope*
		SPS	0.033	0.00071

4.4 Impurity Assessment

As it has been stated before, the resultant films presented multiple impurities that need to be analyzed for further compositional analysis. The purpose of this section is to show the data analysis required to perform a chemical assessment of a film with multiple chemical species forming different compounds.

The metallic films showed presence of carbon, the spectra for each film are found in Figure 4.9. Data appear to be noisy on both deposits, because the quantity of carbon lies close to the equipment resolution for carbon. In the measurements carbon is barely distinguished from noise and their peak areas are calculated with a relatively high uncertainty.

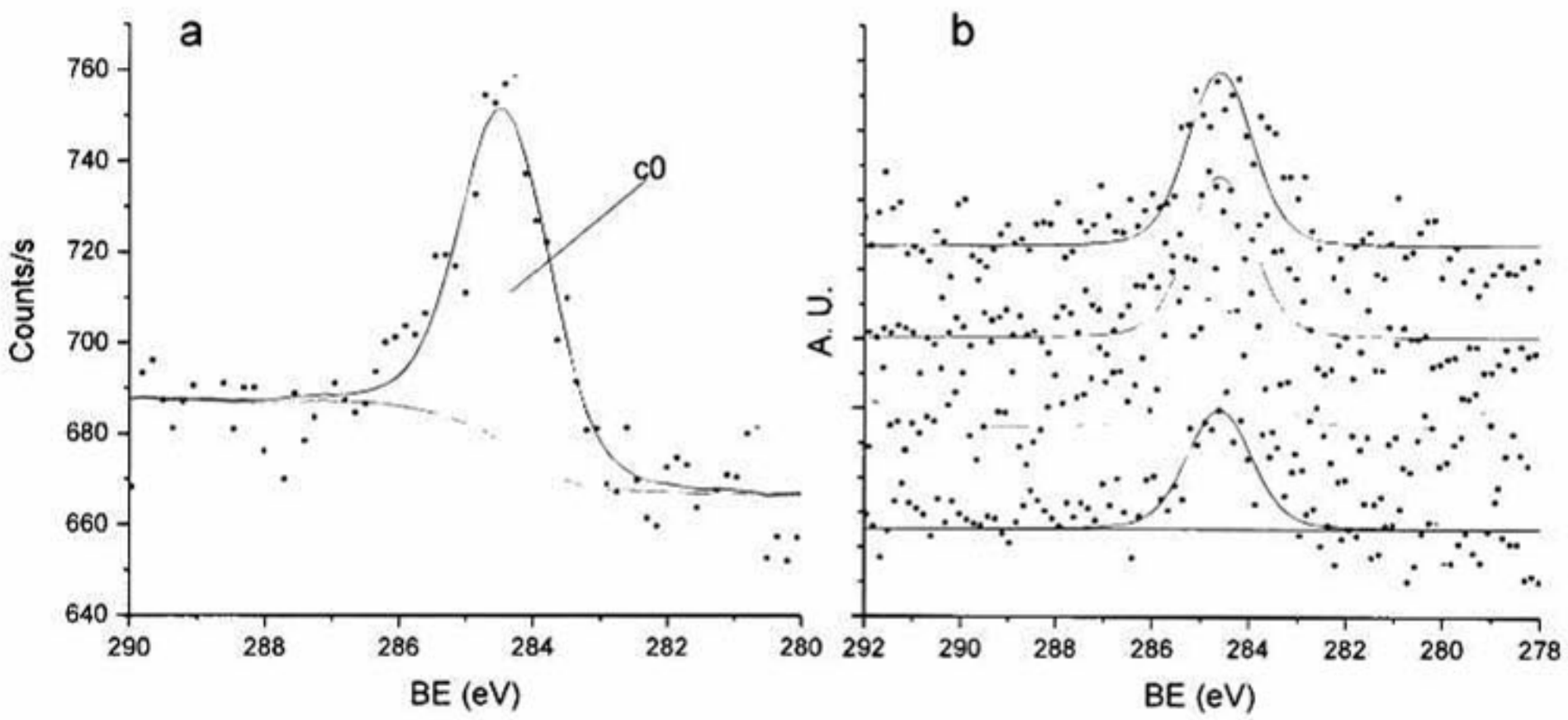

Figure 4.9 C 1s spectra for the a) W coil deposition and the b) Zr coil deposition.

For the Zr coil deposition, several more impurities were found. These correspond to Oxygen, Zinc and Zirconium. In Figure 4.10 the impurity Oxygen spectra is shown. Experimental data modelation requires three peaks with an additional peak centered at 532.52 eV accounting for chemisorbed Oxygen. Peak parameters are found in Table 4.8. The Oxygen spectra did not required the use of a background profile and only a base line was used in peak fitting.

The Zirconium impurity spectra is shown in Figure 4.11. It consists of Zr metal and a strong zirconium oxide signal. Peak parameters are located in Table 4.9. It can be seen that the Zr metal signal is much less intense than the oxide signal. This is in correspondence with the high susceptibility of Zr to bond with O[86]. An issue with this

result is the peak parameters corresponding to Zr metal, which due to the small contribution to the spectra, is difficult to resolve when the strong oxide signal lies in close proximity. So the Zr metal parameters are not completely reliable.

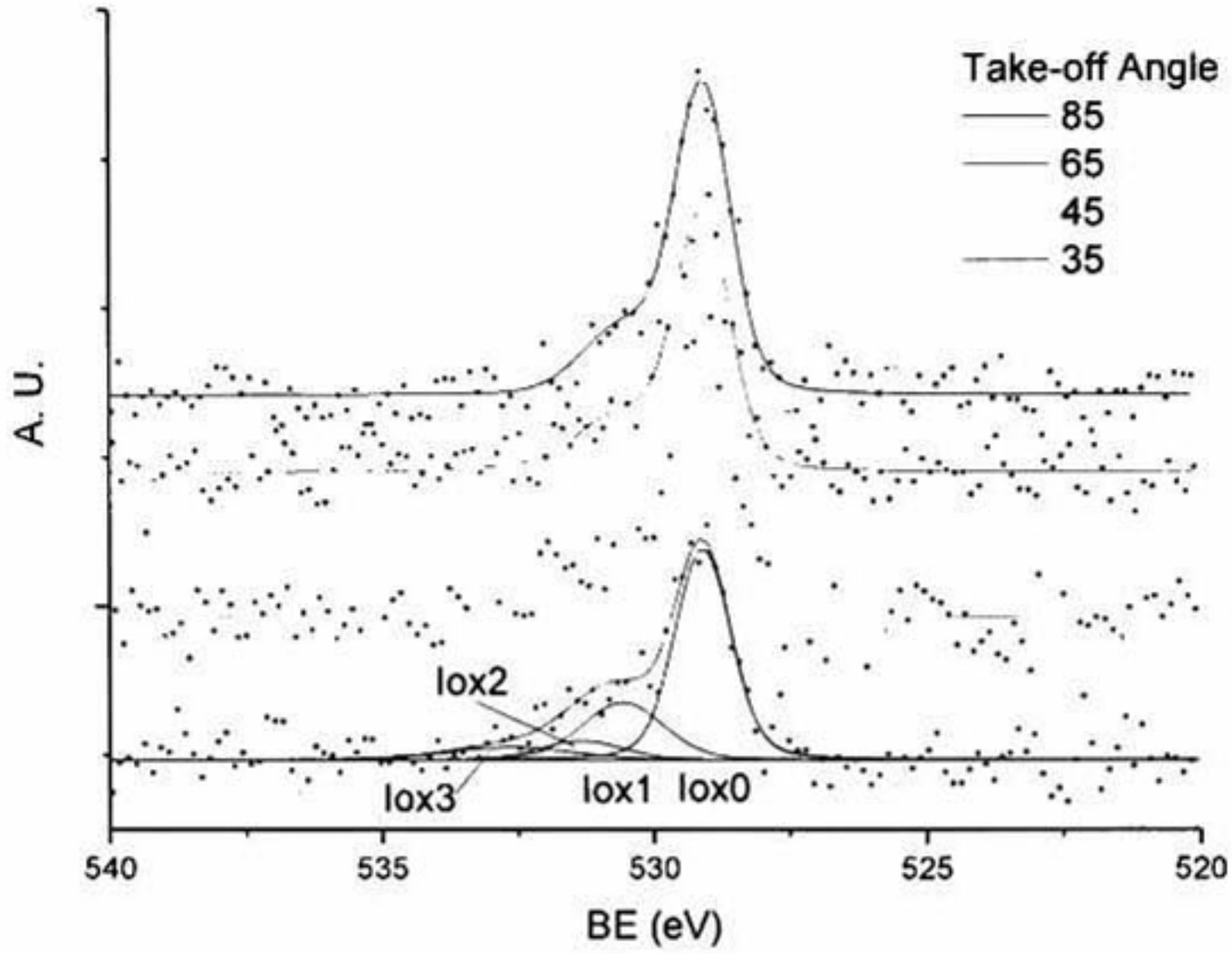

Figure 4.10 O 1s spectra of impurity Oxygen in a Co metallic film.

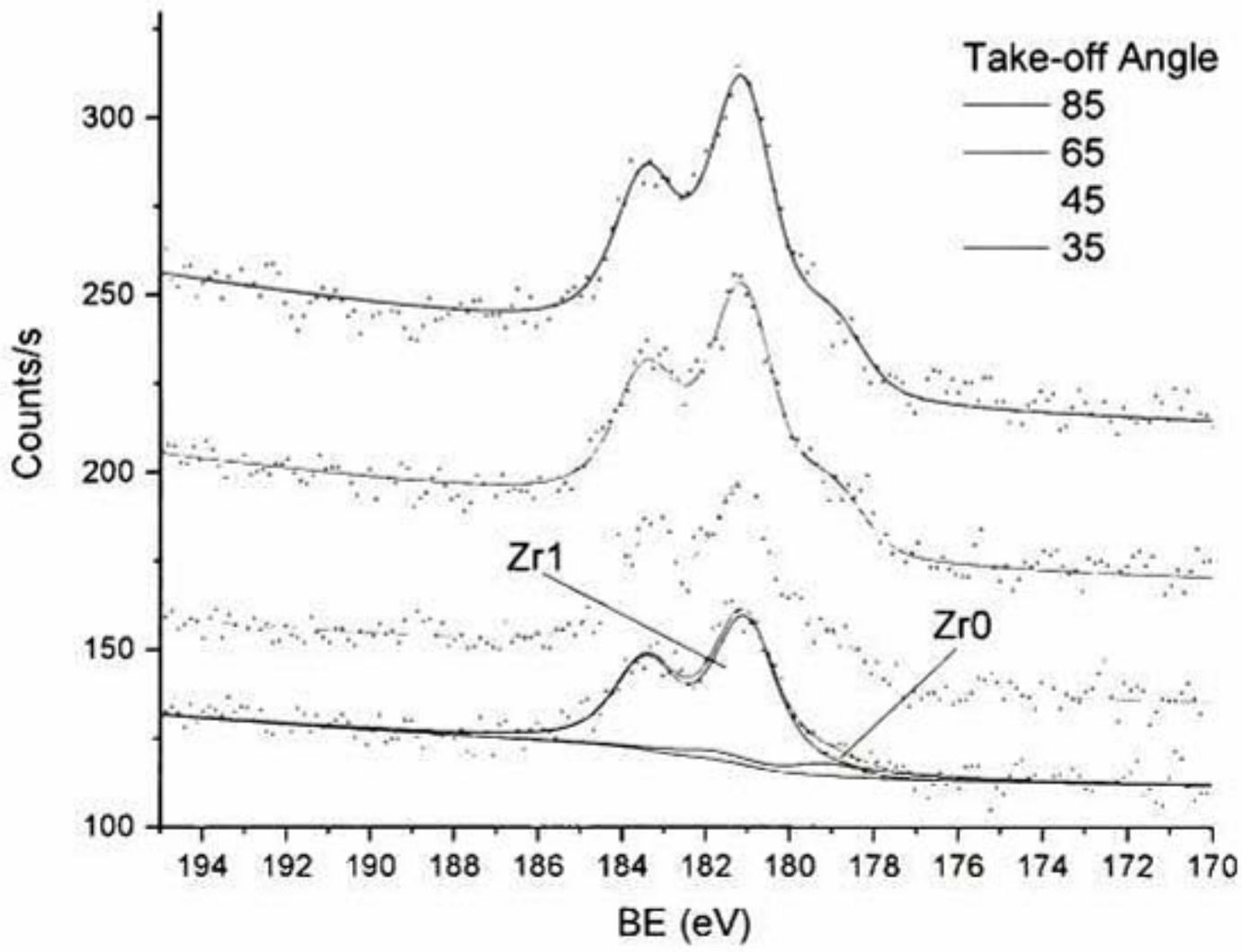

Figure 4.11 Zr 3d spectra of impurity Zirconium in a Co metallic film.

Table 4.8 Peak parameters for the impurity Oxygen in a Co metallic film.

Peak	***BE eV***	***Peak Width***		***Line-shape***
		Gaussian eV	*Lorentzian eV*	
lox0	528.95	1.048	0.25	Voigt
lox1	530.43	1.600	0.25	Voigt
lox2	531.19	1.600	0.25	Voigt
lox3	532.52	2.531	0.25	Voigt

Table 4.9 Peak parameters for the impurity Zirconium in a Co metallic film.

Peak	***$3d_{3/2}$ BE eV***	***SOS eV***	***Peak Width***		***double-Lorentzian Asymmetry***	***Line-shape***
			Gaussian eV	*Lorentzian eV*		
Zr0	178.77	2.82	1.261	0.570	2.831	double-Lorentzian
Zr1	181.04	2.39	1.015	1.146		Voigt
Background Parameters			*Shirley type Background*			*Slope*
			SVSC		0.046	0.00147

4.4.1 Oxidation of Impurities

In the process of controlled oxidation, interesting behavior occurred with the impurity spectra. The metallic Co remained unchanged throughout the whole experimental run as seen in Figure 4.12, giving rise to the question of why the oxidation of Co metal was not possible.

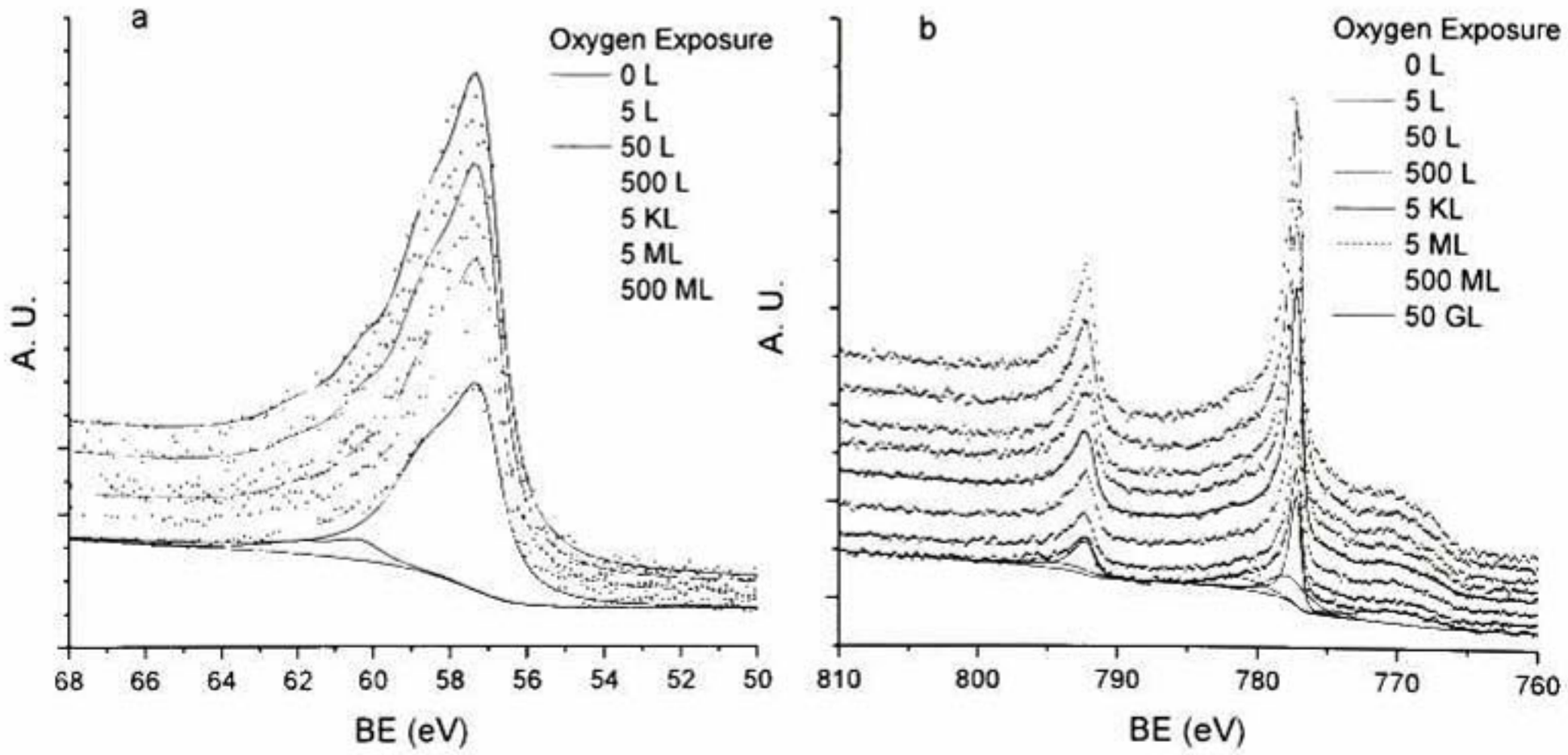

Figure 4.12 Co metal XPS spectra for a) Co 3p and b) Co 2p core level. The Co metal film remained constant upon oxidation; which leads to Co metal film despite O_2 exposure.

The answer to the last question relies in the impurity assessment; observing the corresponding spectra for Zr and Zn in Figure 4.13, the respective metal signal upon further O_2 exposure declines, and the oxide signal increases. This behavior was the pretended one for Co, but Zr and Zn had more affinity to oxygen. Peak parameters for the oxidation of Zr are the same as in Table 4.9, while parameters for Zn can be found in Table 4.10.

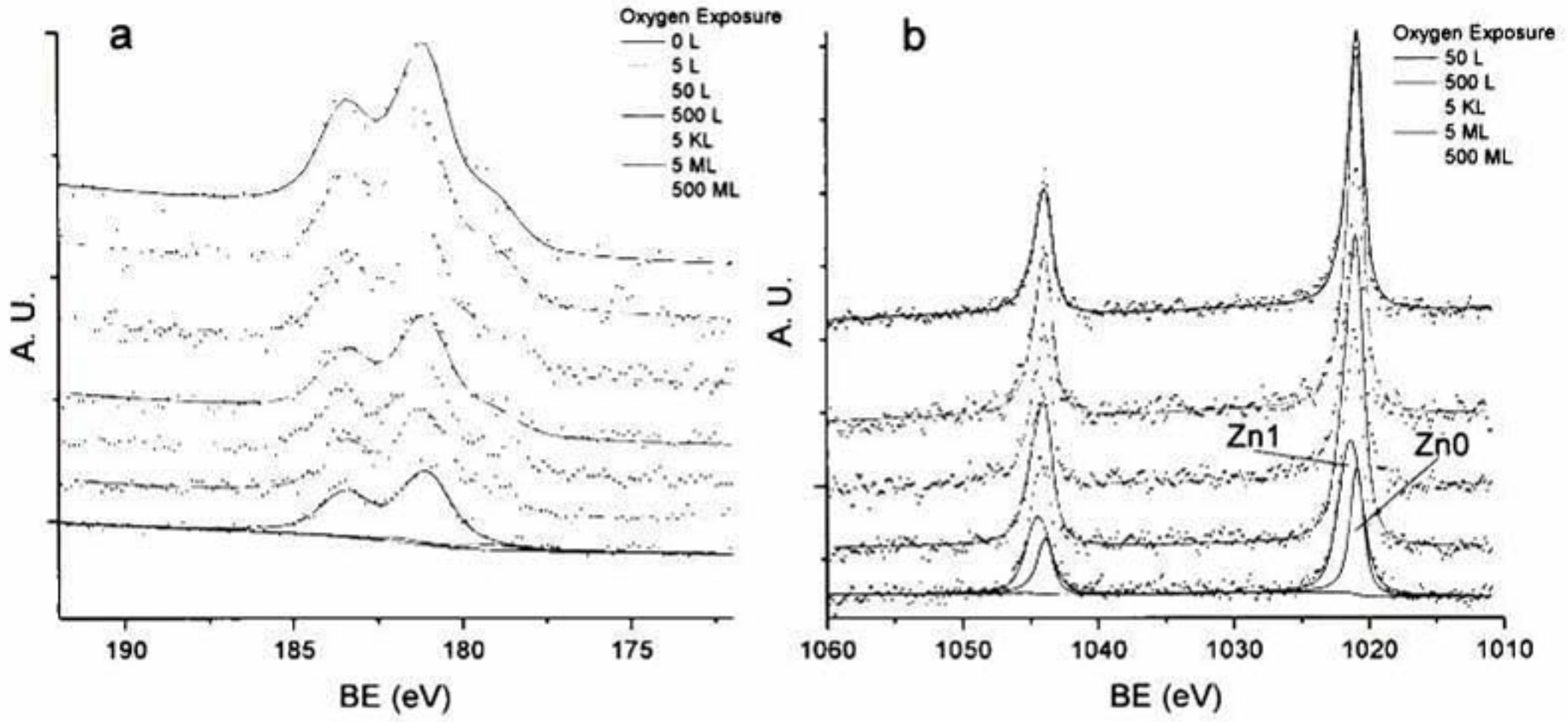

Figure 4.13 Impurity spectra for a) Zr 3d and b) Zn 2p upon different O_2 exposures.

Table 4.10 The impurity Zn peak parameters issued for the film oxidation.

Peak	***$2p_{3/2}$ BE eV***	***SOS eV***	***Peak Width***		***double-Lorentzian Asymmetry***	***Line-shape***
			Gaussian eV	*Lorentzian eV*		
Zn0	1021.01	22.99	0.666	0.735 0.846[c]	1.159 1.420[c]	double-Lorentzian
Zn1	1021.51	23.10	1.490	0.926 0.977[c]		Voigt
Background Parameters			*Shirley type Background*			*Slope*
			SVSC		0.0278	-

c denotes the corresponding value for the $2p_{1/2}$ branch.

In the peak fitting analysis of the Zn 2*p* core level spectra, it was found that the metal and oxide signals lie closely together with a peak separation of only 0.5 eV. The background modeling is rather different in Zn *2p*, whilst the SVSC background is still used, the slope background is not needed and instead a linear background is accommodated in order to fit to experimental data. The reason for this treatment is

that this core level is situated on the final background tail of the Co *2p-2s* core level region that produces a negative slope in the region where the Zn 2*p* core level is situated.

Finally, the impurity spectra for O *1s* and C *1s* can be found in Figure 4.14. The peak associated to chemisorbed oxygen (lox3) clearly increases with parity to increasing O_2 exposure. Aside from the principal oxygen peak (lox0), all peaks increase in intensity and this may help discriminate these peaks (lox1 and lox2) to oxygen bounded to Zn and peak lox0 oxygen bounded to Zr.

The C *1s* spectra through the whole experimental run, remained statistically the same and an evolution related to O_2 exposure is not detected, meaning there was no chemical change in the state of carbon in the film.

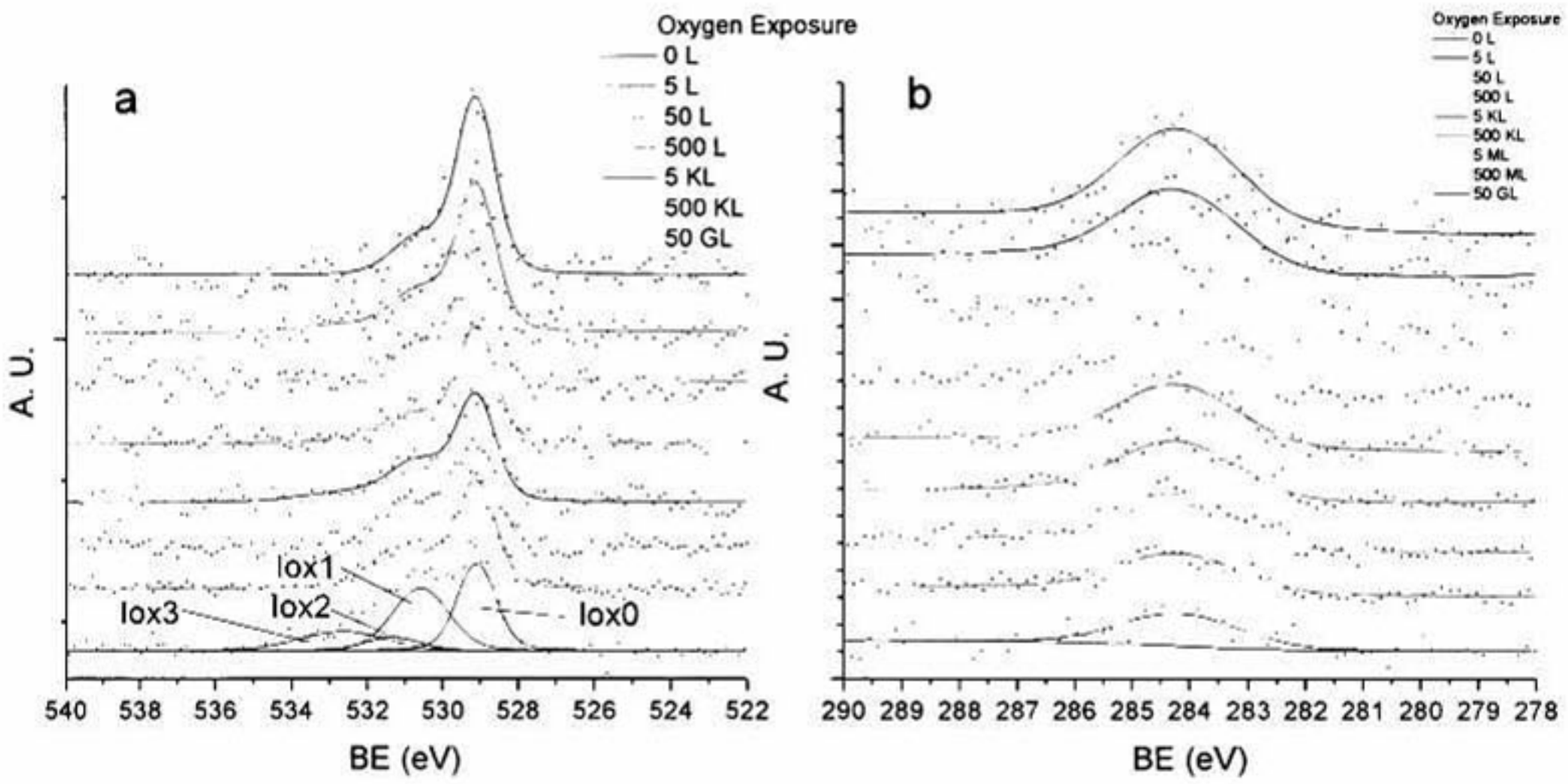

Figure 4.14 Impurity spectra for different O_2 exposures of a) O 1s and b) C 1s.

4.5 Composition Results

4.5.1 Film with Impurities

With the information enclosed in every area calculation performed in the latter spectra, composition for every film can be determined. First in Figure 4.15 the results corresponding to the chemical assessment throughout the oxidation process,

performed to the film evaporated with a Zr coil are shown. Peaks used in this calculation correspond to p0 and p1 in Co 2*p*; Zr0 and Zr1 in Zr 3*d*, Zn0 and Zn1 in Zn 2*p*, c0 in C 1*s* and lastly lox0, lox1 and lox2 in O 1*s*.

Results show that Co percentage consistently declines, due to the formation of ZnO, indicated by the increment of Zn and O in the sample. The amount of oxygen found in the film is coherent with ZrO_2 and ZnO. The last two oxidation stages, where the amount of oxygen related to Zr surpasses the ideal stoichiometric value, can be due to the formation of several sub oxides[86] that could not be resolved peak fitting, limited by the quality of data in terms of noise. High uncertainties in these calculations arise from the information extracted from the O 1*s* spectra; although the obtained intervals in the ZrO_2 composition are reasonable, the calculated uncertainties for ZnO are quite large because peaks lox1 and lox2 are smeared by the other signals that conform the peak envelope in O 1*s* making the area calculation unstable. This is alongside with the relative small amount of zinc oxide, that when the compound increases in quantity, uncertainties decrease.

4.5.2 Partially and Fully Oxidized Co Thin Films

The results are shown in Figure 4.16. The film exposed to 400GL shows the presence of a thin Carbon layer on top. The multilayer model shows that the film is composed of an oxide layer on top of the Co metal film. The chemical assessment of the oxide layer is $CoO_{1.00\pm0.02}$ having a thickness of 23±1.2 Å.

For the fully oxidized film, the results correspond to a spinel compound Co_3O_4. The composition result obtained from the Co *2p* core level is $Co_3O_{4.0\pm0.2}$, while with the information extracted from the Co *3p* core level, composition result is $Co_3O_{4.1\pm0.5}$. For this film, contamination due to Carbon was not present, but a small amount of chemisorbed Oxygen was detected and left out of the calculations.

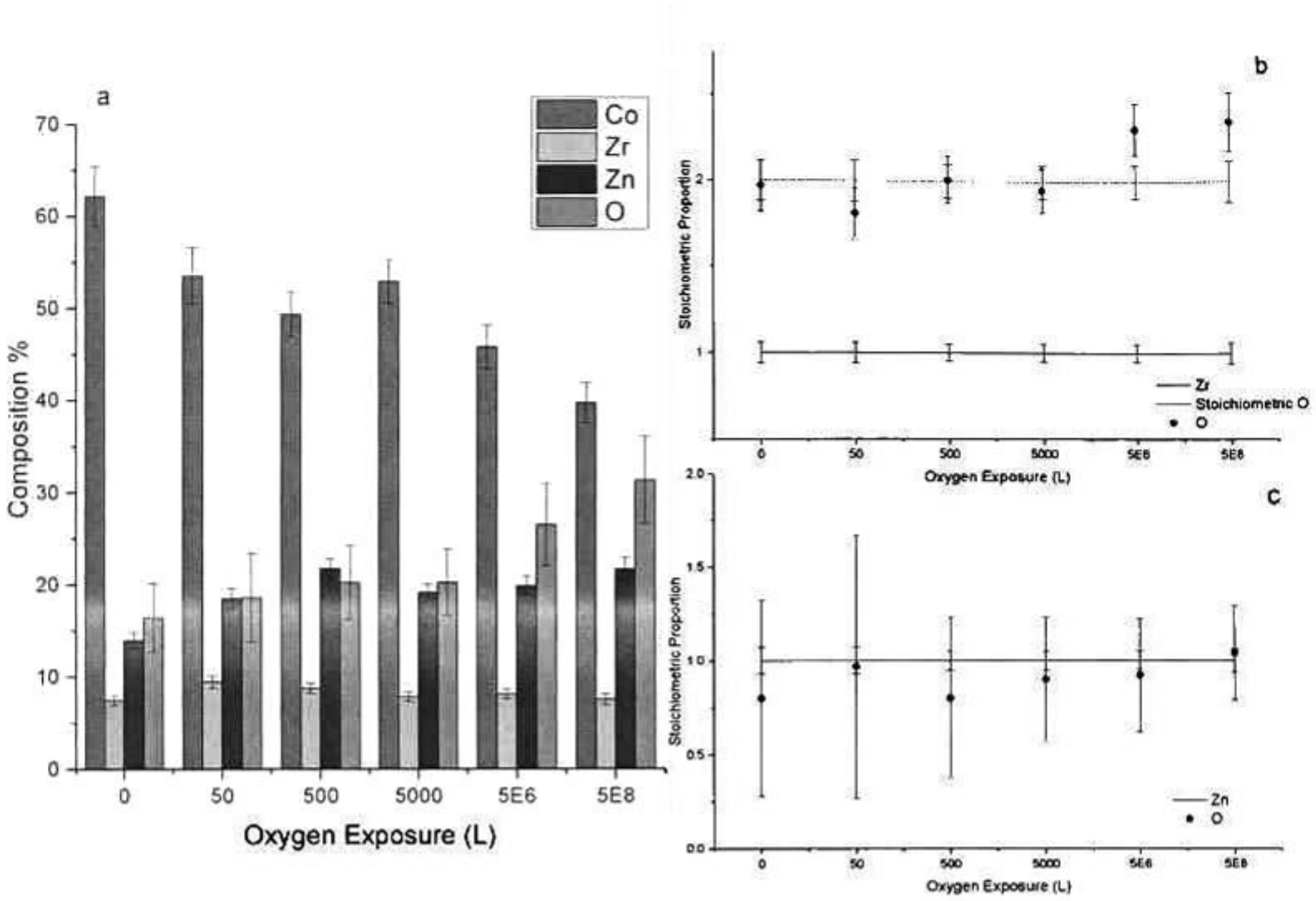

Figure 4.15 Composition results for the impure Co film across different oxygen exposures. a) Composition in terms of total percentage for each chemical specie, b) composition results for Zirconium Oxide where Zr and O are indicated for separated while the dotted line represents stoichiometric oxygen in ZrO_2 and c) shows the stoichiometric proportion obtained for ZnO.

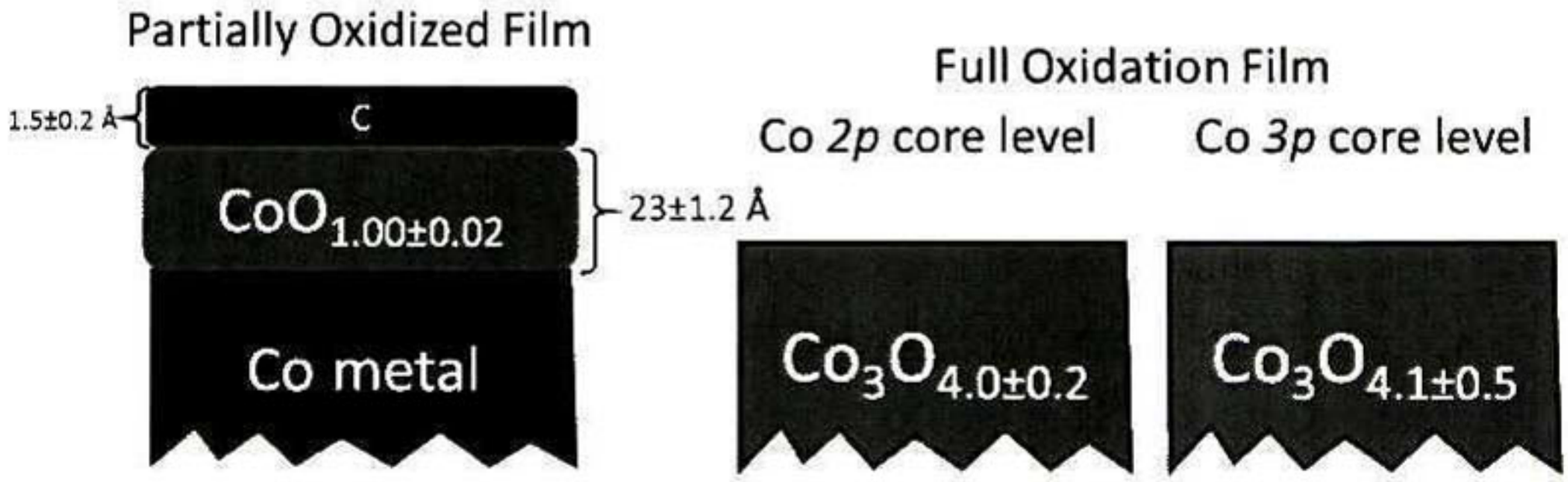

Figure 4.16 Composition results for the partial and fully oxidized films.

5 Analysis and Discussion of Results

5.1 Details of the Cobalt Metal Photoemission Spectra

The Co metal XPS spectra presents a couple of interesting features that need further examination. It is remarkable that the peak shape parameters for each deposition are the same, meaning that in fact the obtained spectra correspond to the Co 2*p* core level of Co metal. The only differences between the spectra produced from the two coils used is the background modeling, where the film produced with the Zr coil has a more intense background contribution to the higher binding energy side of the spectra.

The result of different background contributions can be explained when the impurities involved in one set of films are taken into account. Following the Tougaard-Sigmund theory[25,82], the parameter k_{slope} which refers to the slope of the λK function (inelastic mean free path and differential inverse inelastic mean free path respectively), in the near peak regime accounts for the involved transport process the electron suffers. The optimized value of k_{slope} found for the set of films issued with the Zr coil, leads to think that impurities produces greater photoelectron energy losses that derive in a more pronounced change in slope from the lower binding energy side to the higher side. It may thought that the attenuation length for Co metal is larger than the weighted effective attenuation length of Co with impurities, but for Co metal we have a value of 9.16 Å and for Co with impurities the value is 10.37 Å. It is then that the larger energy losses attributed to Co with impurities, are due to a larger value for the differential inverse inelastic mean free path function corresponding to Zr and Zn; effectively producing in this case a stronger background contribution.

5.1.1 Intrinsic Line Width

Photoemission lines are described via the convolution of a Gaussian and Lorentzian function that refer to the experimental resolution and lifetime broadening respectively. The latter defines the intrinsic line width that obeys the over generalization of the time-energy uncertainty principle as follows[35]:

$$\Delta t\, \Delta E \sim \hbar \tag{5.1}$$

Where mean lifetime is Δt and ΔE is the peak broadness. In this sense, lifetime is susceptible to the various channels in which the photoemission excited final state achieves relaxation.

The results show that the Co 2*p* and 3*p* core levels have very distinct widths. The most obvious reason is that the Co 3*p* core lines have a spin-orbit splitting of 1.32 eV that produces an overlap of the Co $3p_{3/2}$ and $3p_{1/2}$ peaks. Aside, in terms of lifetime broadness this core level is broad when compared to Co 2*p*. The differences can be well rationalized considering relaxation channels via Auger transitions.

The Co $2p_{3/2}$ core level is the sharpest with a width of 0.386 eV; this value is coherent because it lies on the highest occupied subshell of the corresponding principal quantum number. This property, conceptually, does not make possible a Coster-Kronig transition. In contrast, the $2p_{1/2}$ subshell photoemission line, lifetime width of 0.789 eV, has the $L_2L_3M_{45}$ Coster-Kronig decay[87] available.

Coster-Kronig transitions are faster due to the subshell overlap and overlap is enhanced with increasing principal quantum number and decreasing spin-orbit splittings. That is why the Co $3p_{3/2}$ core level results in a Lorentzian width of 0.993 eV related to the $M_3M_{45}M_{45}$ transition, while the $3p_{1/2}$ subshell presents an additional $M_2M_3M_{45}$ super Coster-Kronig decay that results in a 1.324 eV lifetime width.

5.1.2 Core-Line Asymmetry

One of the most characteristic features of the photoemission spectra of metals, is an asymmetric line shape describing the core level signals. Extensive theoretical work has been done trying to elucidate the true nature of these phenomena[39–41,88]; where asymmetry is considered to be an effect of a perturbation of the conduction electrons

caused by the core hole which leads to the creation of electron-hole pairs[36–38,43]. It is shown from data in Table 4.1 and Table 4.2 that the asymmetry value obtained for the Co *2p* and *3p* core levels is different. From the Kotani-Toyozawa model a simpler physical picture can be used to describe this difference, instead of only just using the argument of a different core level spectral function as in the case of the Doniach-Sunjic model[41]. Both models are different, but in principle both deal with the scattering of the conduction electrons as described by Mahan-Nozières-Dominicis[39,40,88]. However, the physics described by this theories are more likely to describe a type of background.

The results indicate that the Co metal *2p* core level has a larger asymmetry compared to the value registered for the *3p* core level. In the creation of a core level photoelectron, the core hole left behind with a certain potential pulls the *d* band immersing it in the wide *s* conduction band where it acts as a scattering center for the conduction electrons. It is possible to think that the *2p* core hole potential produces such a perturbation in the conduction electrons, that when it is compared to the *3p* core hole induced excitations, leads to more electron-hole pairs created. This argument is solely based on the core line asymmetry theory previously mentioned. The double-Lorentzian line shape is just a mathematical construct used to account for asymmetry and only produces the best experimental fits; so the latter analysis is based on the existing consensus of the physical interpretation of asymmetry, although the true physical origin is still open to further discussion; another mechanism that describes asymmetry is the creation of multiplet states and itself compels with the double-Lorentzian line-shape.

The asymmetry found in metallic peaks can therefore also be explained in terms of a multiplet structure and not the creation of electron-hole pairs. The multiplet splitting hypotheses follows the idea that an open valence sub-shell couples in such a way with the excited core level that several mainline peaks in the photoemission spectra are created[89]. The coupling scheme fundamentally will depend on the angular momentum of the electrons left behind in the photoemission process, where distinct states are formed depending on whether the final hole state is located in the $np_{3/2}$ or

the $np_{1/2}$ core level. The different asymmetry values can be an indication of specific splitting magnitudes for each core level upon photoemission.

5.1.3 Co Metal Satellite Peak

The interpretation of the satellite (p1 and p'1) signal is piled up with controversy. There is a lack of evidence that explains the true nature of this peak. Interpretations fundamentally vary; the Kotani-Toyozawa[36–38] model has been used to account for a mainline and satellite peaks related to individual screening final states.[62]

This individual screening of final states is schematically presented in Figure 5.1. It describes the Kotani-Toyozawa model, it is also called the two-hole theory where one hole corresponds to photoemission and the other to a hole in the 3d band in one of the final screening states. The main photoemission peak and a satellite are created by two final states where the binding energy from each will depend on whether an electron remains in the 4*s* sublevel or it is transferred to the 3*d* sublevel.

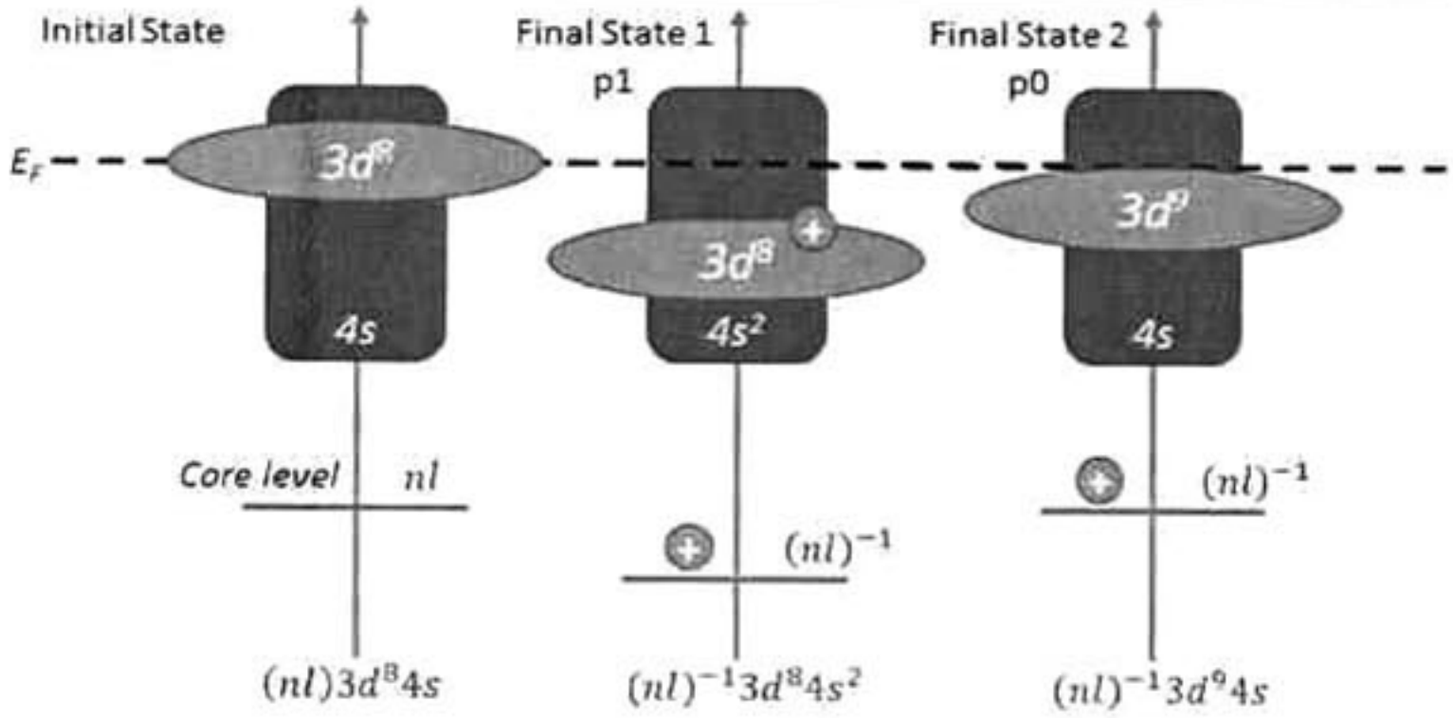

Figure 5.1 Representation of the Kotani-Toyozawa model applied to Co. Final state 1 and 2 refer to two different screening states created after photoemission.

In principle the applied framework seems reasonable, but the unfilled valence band in Co leads to correlation effects that are not taking into account in this picture. Experimentally, it is possible the discard the model, that is been successful with other metals, because a contribution of this nature has been found to be weak or non existent[63,90]

Another interpretation for this peak is that it is caused by plasmon losses. The interpretation is based on reflective energy loss spectroscopy (REELS) data[6,67],

where resonances are found, using a beam energy of 0.3 KeV, close to the satellite position. Inconsistences arise because scattering in REELS data do not necessarily correspond to a photoemission spectra; intrinsically the resultant photoemission spectra is affected by the core hole left behind and extrinsically the beam energy and the photoelectron kinetic energy are rather different, doubled.

The elucidation of a plasmon-loss feature or any feature related to scattering requires a proper background treatment. As stated by Tougaard & Chorkendorff[91] all loss features due to scattering can be resolved into the photoemission spectra using REELS data with a correct elastic peak subtraction and correcting for multiple scattering. Taking the basic physical idea that the XPS background is generated by photoelectron collisions in the escape trajectory from the material[25]; it is possible to assume that a certain photoelectron has a probability to scatter that is proportional to the distance traveled.

Generating a first order approximation of the probability a photoelectron will have of colliding one time in a certain escape trajectory we have:

$$P_1 = P_{no\ collision} P_{collision} P_{no\ collision}$$

$$P_1 = \left(1-\frac{dx}{\lambda}\right)^m K(E_0,T)\,dx dT \left(1-\frac{dx}{\lambda}\right)^{n-m-1} \tag{5.2}$$

Here we have divided the whole escape trajectory in n intervals and m defines the intervals until the first collision, λ is the effective attenuation length and $K(E_0,T)dxdT$ is the probability of collision and lose a certain energy T within a given interval that an electron has and E_0 is the energy at which the photoelectron was emitted. Computing the probability of an electron with energy E_0, losing energy T, when $n \to \infty$ in any given point of an escape trajectory R we have:

$$P_1 = K(E_0,T)\,dT R e^{-\frac{R}{\lambda}} \tag{5.3}$$

With the last expression it is possible to obtain a first order Tougaard background approximation that assumes that a component of the XPS background can be defined by all the generated photoelectrons that have collided one time. To construct this relationship we have to know that the photoemission signal depends on several

geometrical factors[24,31] and that photoemission can occur over any depth limited by inelastic mean free path; integrating the product of all emitted photoelectrons by the first order collision probability across depth, we obtain the following expression for the first order Tougaard background approximation:

$$B_1(E) = I_0(E_0)\lambda K(T)dT \tag{5.4}$$

Where $I_0(E_0)$ is the initial photoemission intensity that corresponds to the mainline peak in the photoemission spectra. At this point we have to integrate over all possible lost energy due to the collision and defining this lost energy as:

$$T = E_0 - E \tag{5.5}$$

Integrating we have,

$$B_1(E) = \int_0^\infty I_0(E+T)\lambda K(T)dT \tag{5.6}$$

Where $\lambda K(T)$ for metallic Co film corresponds to the differential inelastic electron scattering cross section function defined through REELS data that has the elastic peak subtracted via the Tougaard-Chorkendorff recursion formula[91] The latter is shown in Figure 5.2.a. Using Eq.(5.6), two outputs have been calculated; one corresponding to the Co main photoemission line and the other accounting for the Auger lines contribution. The addition of both outputs is expressed as $B_1(E)$ in Figure 5.2.b. From what it seen around 705 eV the experimental data is not accurately reproduced, meaning that p1 is not a loss feature due to scattering. Introducing a Shirley background contribution for the main and Auger photoemission lines and a Tougaard type for each, the background modeling is very close to experimental data, with the exception of the contribution of the satellite peak p1 to the spectrum.

It is noteworthy, that the satellite peak position differs whether photoemission originates from the Co $np_{3/2}$ *or the* $np_{1/2}$ core level. The results show that the satellite peak is located 4.06 eV from the Co $2p_{3/2}$ mainline and 1.68 eV from the $2p_{1/2}$ peak. This correspondence does not apply to n=3, where satellite position with respect to Co $3p_{3/2}$ is 3.49 eV and 4.10 eV from the $3p_{3/2}$ mainline. These results are not found

elsewhere, because is not common to peak fit both photoemission branches and with the results it is shown that valuable information is lost when peak fitting only the $np_{3/2}$ branch.

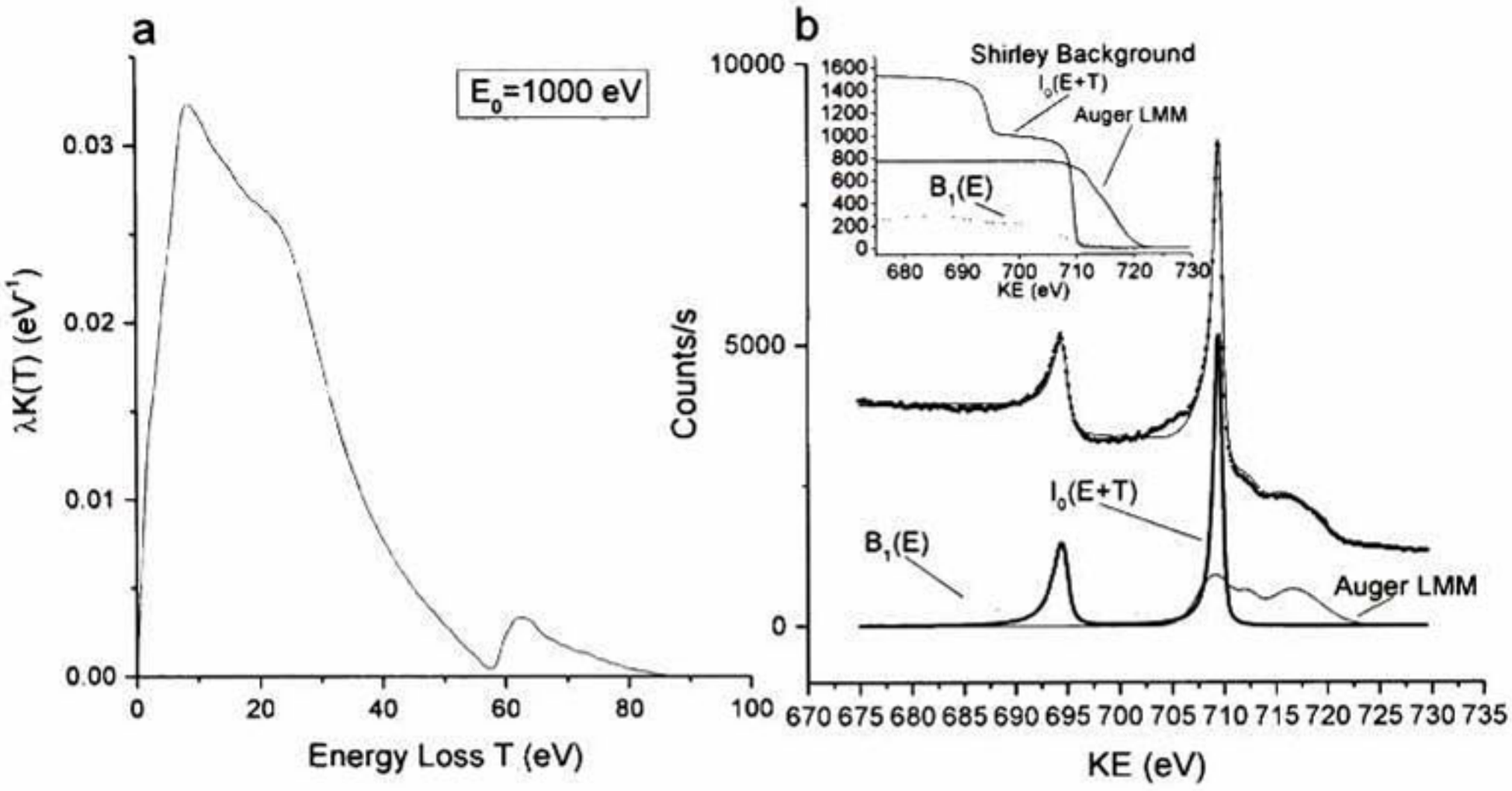

Figure 5.2 First order Tougaard background approximation. a) Differential inelastic electron scattering cross section obtained from REELS data using the Tougaard-Chorkendorff recursion formula and b) Resultant spectrum using the Tougaard background approximation. The insert shows the Shirley background contribution from the mainline and Auger peaks alongside the Tougaard background.

At the moment, the screened hole state and the plasmon loss explanations do not account for the p1 contribution entirely. It is then that the true nature of satellite peak p1 remains an open question and several correlation effects need to be studied in order to accurately determine the reason that originates this signal in the photoemission spectra.

It is possible that p1 is originated by a shake-up feature that has a strong dependency on angular momentum. The peak shape parameters strongly indicate that different coupling schemes occur between core levels and the valence band. Taking this argument as true, we can think that the core holes left behind will breakdown the degenerate states of the valence band into different discrete states. The perturbation created by the core hole, in principle, will have a strong dependency with angular momentum and thus we can observe p1 with different positions with respect to each main $np_{3/2,1/2}$ photoemission branch.

In this sense, the shake-up feature can also be related to the valence band coupling. Experimentally, it can be observed that the shake-up peak is closer to a more

asymmetric main peak; apart from having different intensities, the shake-up peak in the Co 3*p* core level is different from the shake-up feature seen in the 2*p* core level, because p1' is closer to the $3p_{3/2}$ branch and p1 is closer to the $2p_{1/2}$ branch, so they involve transitions that depend on how the valence band is rearranged in the photoemission process.

5.1.4 Auger LMM Contribution

An important feature of the Co 2*p* XPS region when using Al *K*α X-ray source is the Auger LMM photoemission lines. Auger peaks are labeled as p2, p3 and p4 because they are non-existent in the Co 3*p* core level photoemission spectrum. The Auger structure is found across all the Co 2*p* spectra and are needed for one to be able to estimate peak areas accurately, otherwise all the fits presented in this work are not possible. The contribution by Auger lines strongly contributes to the spectra and an accurate peak area estimation also requires a precise background treatment[7]
When the Auger peaks are not taken into account, peak areas are overestimated[7]
In other reports, it is typical to issue peak fitting starting from 770 eV of binding energy, in Figure 5.3 a typical peak fitting of the Co 2*p* core level is shown. Peak parameters change in order to reproduce experimental data, despite this fact, the analysis of the XPS features comply with the results previously obtained with the fit results including the Auger structure.
In terms of a qualitative analysis, with caution it may be possible to extract the same conclusions whether the Auger peaks are or are not included in peak fitting; however, dealing with a quantitative problem the peak areas rather differ and not including the Auger peaks causes that peak area calculations produce results overestimating the area of p0 in 14.52% and the complete Co metal signal is overestimated in 41.06%. These values strongly indicate that the three peak Auger structure must be taken into account in order to obtain precise results. The idea of considering Auger lines in quantification is stated elsewhere[7], but it is practiced poorly and reports showing the quantity of peaks composing the Auger structure, at the moment, are not found; despite the fact that the Auger peaks have strong contributions that need to be accounted for while modeling the experimental XPS data.

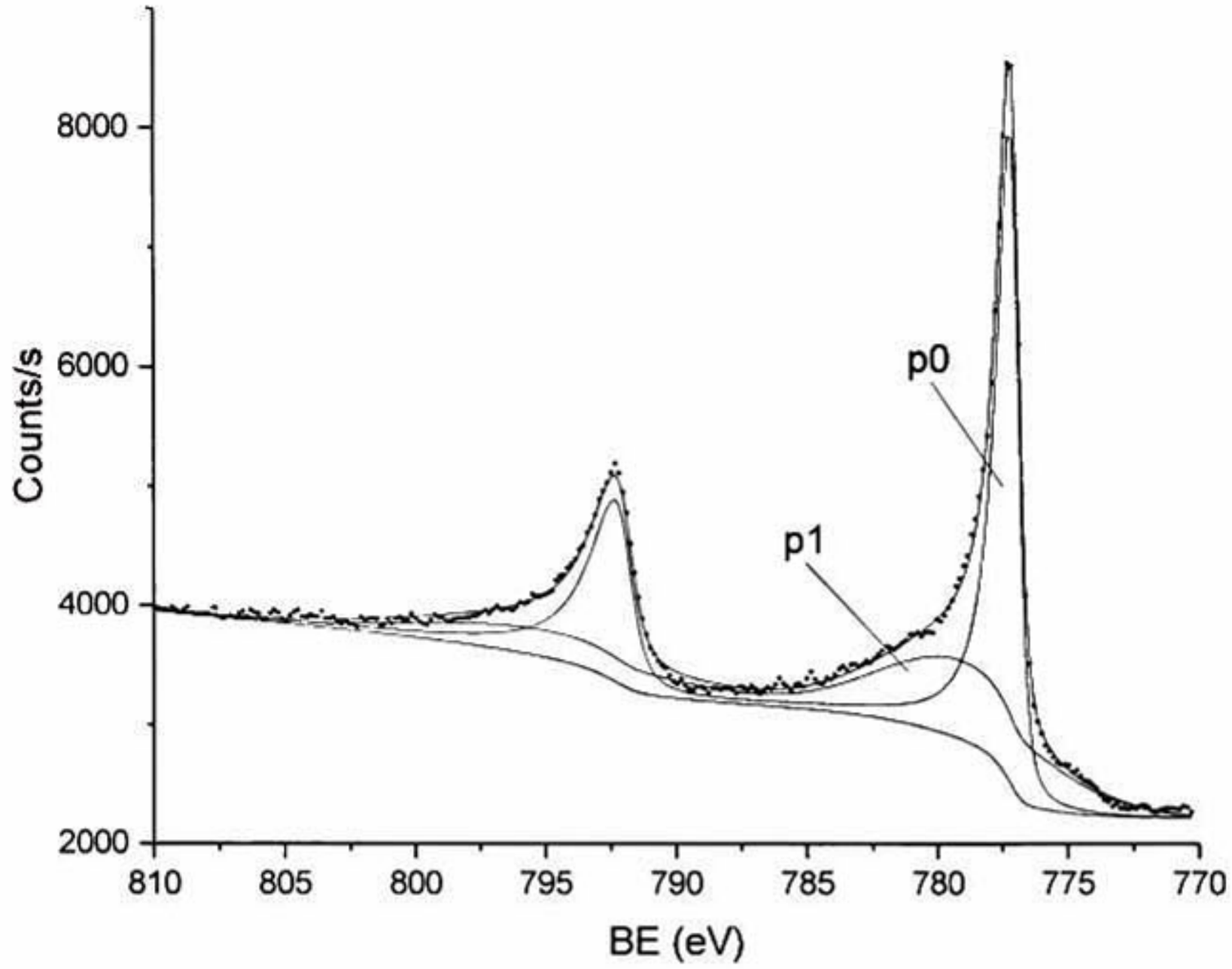

Figure 5.3 Co 2p core level peak fitted excluding the Auger LMM peaks. Energy range is typical of what is seen in other reports.

Extracting the Auger peaks contribution to the spectra and shifting them by 233.1 eV to account for the X-ray source energy difference, these peaks can be peak fitted to experimental data taken with a Mg Kα X-ray source. Figure 5.4 shows the result. The insert on top shows direct comparison between the fit obtained for the Co 2*p* core level and the Auger experimental data, readily it can be seen that these two have a different Shirley intensity, but still the approximation is fair between both.

The background signal in Figure 5.4 is accurately modeled. It is seen that p2, p3 and p4 do compose the Auger LMM experimental data. Peak S is due to the X-ray source satellite. Additionally, p5 is needed for an accurate reproduction of experimental data; but this peak is difficult to resolve in the underlying Co 2*p* core level photoemission spectra. The reasons for this issue is that p5 is the less intense peak of the Auger structure and is located just below p0 and p1, where the background intensity of these cover the contribution of p5. So, in the Co 2*p* core level the p5 contribution to the spectrum is already taken into account within the background

modeling. The results also indicate that the Mg Kα X-ray source produces a Shirley background with greater intensity when compared to the Al Kα radiation.

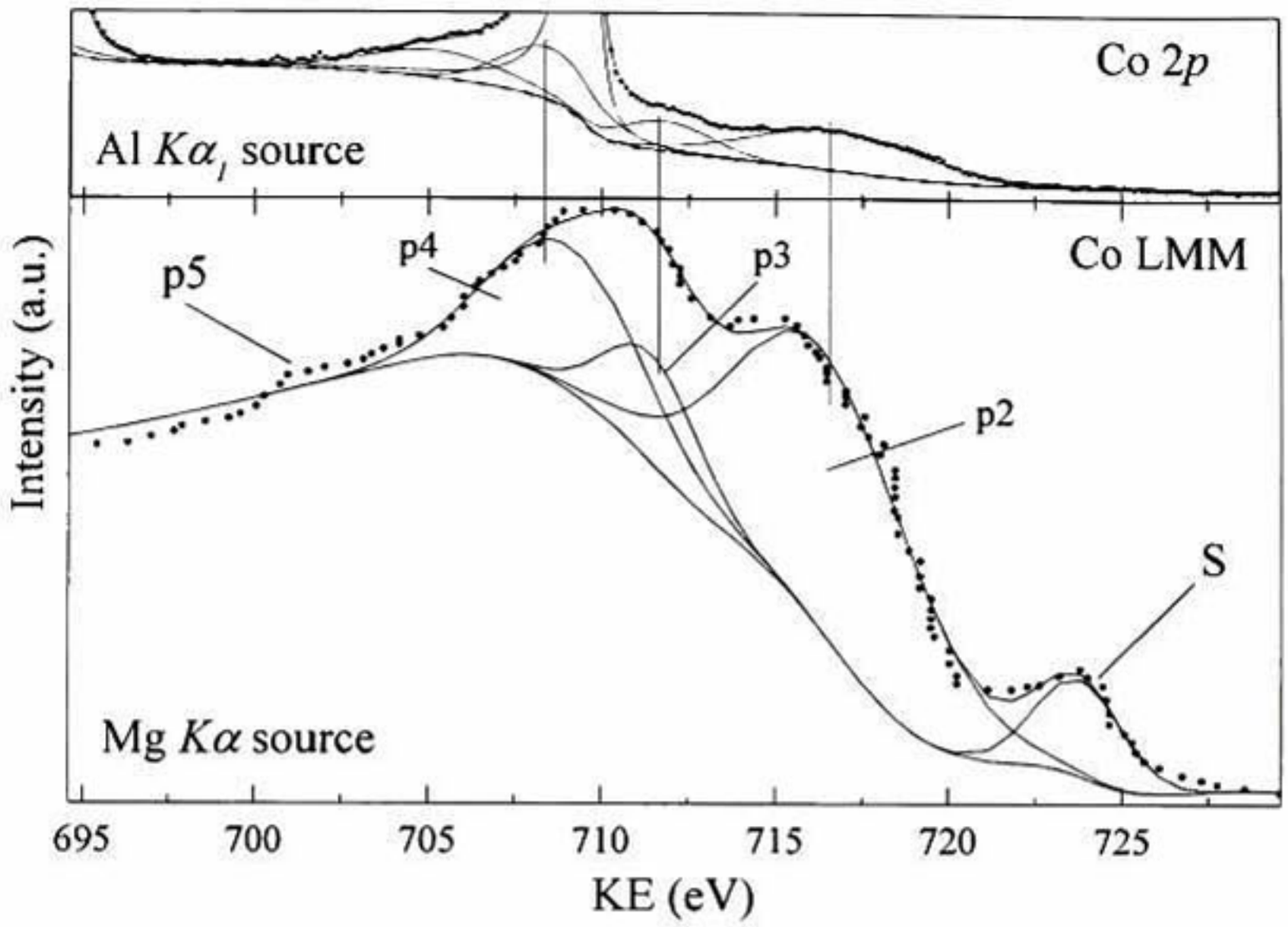

Figure 5.4 Co LMM spectrum taken with a Mg Kα X-ray source. Insert on top shows the Co 2p core level measured with monochromatized Al Kα radiation. There is a direct correspondence between peaks on both spectra. An expanded view of the background modeling issued in the 2p core level is also shown; this is a clear indication that the Mg Kα X-ray source produces a more intense Shirley background.

5.2 The Cobalt metal-CoO Photoemission Spectra

The purpose of the partially oxidized film is to show the XPS features of Co metal alongside the CoO ones. An important characteristic in Figure 4.5 is the background modeling where all the contributions related to CoO have been found through peak fitting. This background signal is far away from experimental data and makes imperative that peak fitting is done evaluating both photoemission branches, if not, peak underestimation is straightforward.

We have to note that each photoemission line present in the spectrum possess different Shirley background intensities. For this reason, background modeling required the use of the SVSC background. The Co metal signal issues a 0.0920 Shirley value, Co^{2+} has a 0.0235 Shirley parameter while the Auger peaks have a

0.0255 Shirley intensity. From these results, the Shirley intensity decreases with the increase in the oxidation state of a certain chemical specie.

The peaks comprising the CoO signal in the Co 2*p* core level is composed of a broad mainline (a0 in Figure 4.5) and several satellite peaks (a1, a2 and a3 in Figure 4.5). Intense satellite peak a2 has been explained in terms of a charge transfer satellite. Cluster model calculations indicate that strong electron correlations occur when the core hole is created and with the crystal field effect of an octahedral symmetry in the 3*d* sublevel imposing a $t_{2g}^5 e_g^2$ electronic configuration, it is energetically possible the electron transfer from the O 2*p* sublevel to a 3*d* t_{2g} orbital[56,68,65,69], thus closing the subshell.

Peaks a1 and a3 can be thought of being result of linear combinations of charge transfers between the O 2*p* sublevel and the different orbitals comprising the 3*d* sublevel[68]. To prove that the satellite features are intrinsic to the Co 2*p* core level of CoO it is necessary to analyze pure CoO. Photoemission data has been taken from other reports, digitalized and peak fitted the spectra. A clean photoemission spectra of CoO without the Auger LMM structure is taken from the work of Shen et al.[92] where the X-Ray source consists of synchrotron light with a photon energy of 1253.6 eV and data featuring the Auger LMM structure corresponds to work presented by Kim[93] using a typical Al $K\alpha_1$ X-Ray source. These are shown in Figure 5.5 and peak fitting shows that the four peaks comprising the CoO XPS features in the partially oxidized film, do appear likewise in the experimental data recorded in other reports. Background modeling in data from Shen et al. was issued with a SPS background obtaining a Shirley intensity of 0.0235, data from Kim, due to the Auger peaks with different background intensity required the use of the SVSC background where the Auger peaks have a 0.0508 Shirley contribution and outstanding result is that the Shirley value for the CoO XPS features is 0.0235. These values correspond to the same Shirley intensity obtained from data recorded from the partially oxidized film. Despite the photon energy used or the presence of Auger peaks, the analysis strongly suggests that the Shirley type background is an effect caused by an intrinsic property of each chemical specie that has repercussion on the final photoemission signal.

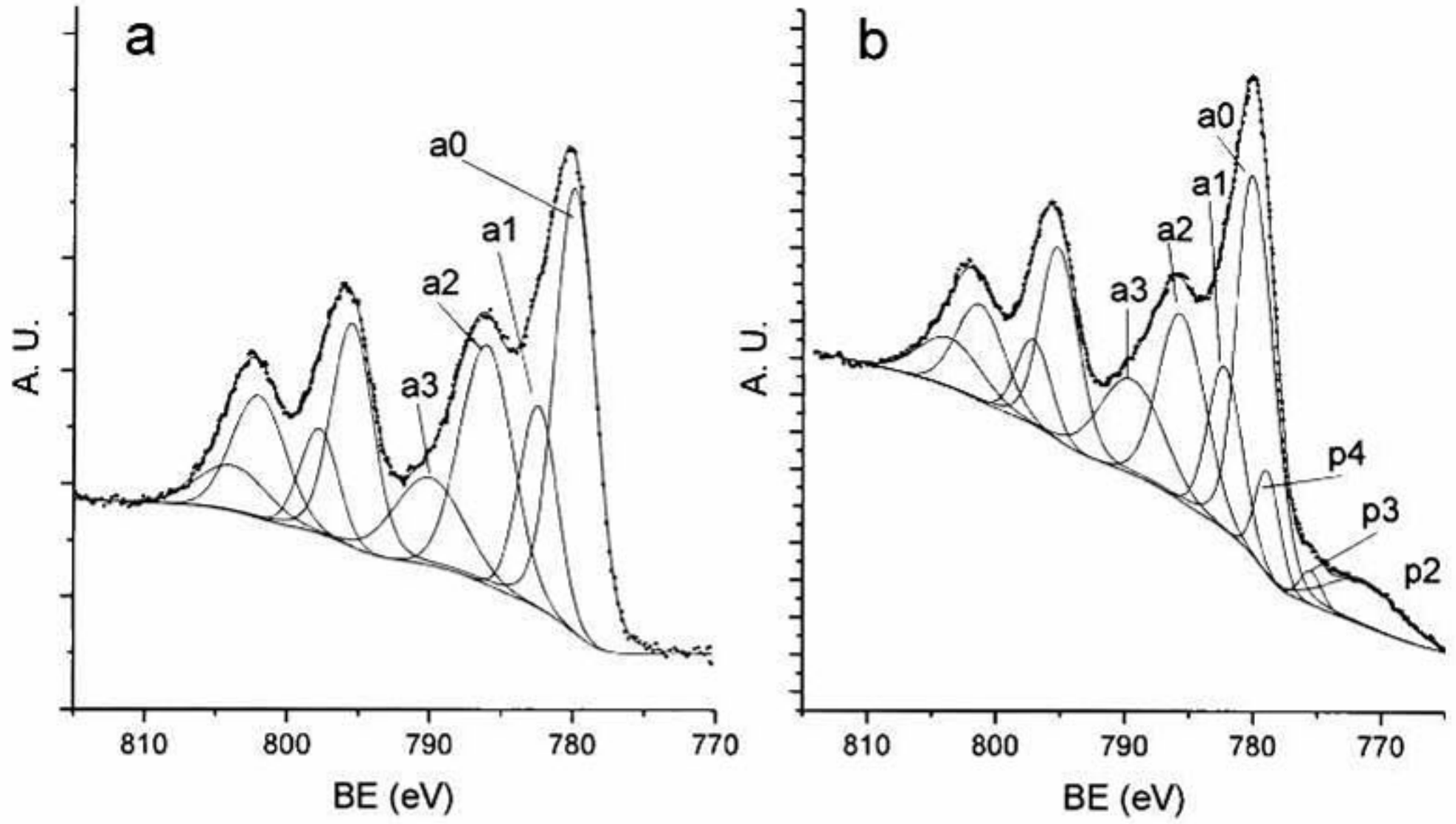

Figure 5.5 Photoemission spectra of CoO a) using a photon energy of 1253.6 eV while measuring the CoO (001) face reported by Shen et al. and b) powder CoO spectrum obtained with an Al $K\alpha_1$ X-Ray source reported by Kim.

The intrinsic linewidth of 0.45 eV is found in each CoO spectra. This result demonstrates that peak fitting is a powerful tool that enables the consistent extraction of information regardless of the XPS tool; the only difference is in terms of Gaussian broadness which is an aspect related to the electron analyzer resolution that logically differs in each XPS equipment.

Analyzing the position of the satellite peaks we can observe that a1 and a2 have a similar spin-orbit splitting as to the mainline splitting. Satellite peak a3 shows lower spin-orbit splitting. Calculations dealing with both photoemission lines at the moment have not been developed and the splitting characteristics are not reported elsewhere. The most accurate peak position determination can only be done via peak fitting.

Results showing distinct spin-orbit splittings for each satellite signal indicates that correlation effects related to angular momenta deal a great matter on these features. Following the charge transfer model, it may be possible to think that different core hole potentials affect the coupling between the core hole and the *d* band causing distinct charge transfers from the O 2*p* sublevel. Further calculations considering the $2p_{3/2,1/2}$ mainlines are necessary to theoretically determine the nature of these peaks;

although high uncertainty in the peak position calculations still remain a problem to overcome. So, the most accurate and practical method to determine the satellite features is via peak fitting using the parameters reported in this work.

Dealing with the cobalt oxide counterpart, the O 1*s* spectrum in Figure 4.6 shows two very discrete peaks. The presence of two peaks is noteworthy because they are in fact components of CoO. Peak ox0 can be referred as the normal oxygen photoemission peak coming from atoms arranged in a typical Co-O_6 octahedral symmetry. This kind of arrangement is typical of a bond that is predominantly ionic; in this sense, ox1 is a peak where the bond starts to acquire a degree of covalence. In XPS analysis an increasing peak shift is a qualitative indicative of an increase in the degree of covalence the bond of certain compound has. Thus, ox0 is a photoemission line coming from oxygen with a predominant ionic bond, while ox1 comes from oxygen bonded with a higher degree of covalence.

The key issue here is what causes the covalence in the CoO bond. It has been proposed that is a surface effect[94] that causes oxygen vacancies, thus increasing covalence. Reports show that the O 1*s* spectra is susceptible to the local environment of the compound, where lower coordination numbers shift the oxygen peaks to higher binding energy values[57,58] The ideal coordination of cobalt oxide (II) is 6, but several factors may decrease the coordination; the most important is an amorphous film and the procedure used to grow the thin oxide layer, where a simple surface to gas reaction is susceptible to the formation of many point defects at the surface[57–59] The partially oxidized film was exposed only to oxygen with no additional sintering techniques whatsoever, so the strong contribution of ox1 to the O 1*s* spectrum is rational when the oxide growing technique is taken into account. Reports showing a single peak O 1*s* spectra of CoO[92,93,95] shows that the material measured has a reduced amount of defects or oxygen vacancies at the surface, in contrast to the partially oxidized film produced in this work.

5.3 The Co_3O_4 Photoemission Spectra

The photoemission spectrum of the Co 2*p* core level of the fully oxidized film, shown in Figure 4.7, qualitatively assures that the film is in fact Co_3O_4. The sharper peak and less intense satellite feature in comparison with CoO, is a fingerprint for Co_3O_4. In this case, angle resolved data is presented where no angular modulation demonstrates that Co_3O_4 is firmly distributed across depth.

The peak fitting procedure is very complex compared to the previous ones; complexity is due to many peaks lying closely together. Characteristics that are consistent in all the spectra correspond to the presence of the three peak Auger structure and the Lorentzian width of 0.449 for the Co^{2+} peak.

As seen in the partially oxidized film, the final of strong Auger LMM peaks as well produces a linear component to the fully oxidized film spectra. The linear background characteristic is a feature that is present on the lower binding energy side of all the Co 2*p* core level photoemission spectra measured with an Al $K\alpha_1$ X-ray source.

The contribution of the three peak Auger structure (p2, p3 and p4) is slightly modified in the fully oxidized spectra. In this case, we observe that these peaks are shifted towards higher binding energies and Gaussian widths modified. This peak parameter modulation may be related to the chemical environment; for the partially oxidized films, Auger contributions consisted of overlapping transitions coming from Co metal and Co^{2+} 2*p* core levels, while for the fully oxidized film spectra, Auger lines come from Co^{2+} and Co^{3+} 2*p* core levels, thus eliminating the Co metal contribution. The peak shape parameters found for the Auger structure allow an accurate modeling of the background contribution, that besides reproducing experimental data, they are an important feature that has direct repercussion in the chemical assessment calculations.

The photoemission lines are fitted as doublets and both Co $np_{3/2,1/2}$ branches are accurately peak fitted by correlating peak parameters. Two sharp peaks are resolved in the spectra, b1 and b0 that are related to Co^{2+} and Co^{3+} respectively. These are accompanied by an intricate weak satellite feature, complexity rises due to closely lying peaks that overlap and make the peak fitting procedure difficult. Peaks b2, b3

and b4 are the peaks required to obtain an accurate data reproduction. The nature of these peaks can be ascribed to charge transfer satellites. The relative peak position and intensity of b0, b1, b3 and b4 is justified by cluster model calculations performed elsewhere[69]. Peak b2 is not seen in other reports, but besides the need for it to reproduce experimental data it is also needed to obtain chemical assessment results that comply with stoichiometric values. A reason for this peak not appearing in other reports, could be poor resolution and inadequate background treatment when peak fitting the spectra.

We can observe that the satellite peaks have distinct spin-orbit splitting values, a characteristic only seen when both photoemission branches are peak fitted. These results strongly suggest that the charge transfer phenomena in photoemission, has a dependence related to angular momenta. The correlation effects produced whether photoemission comes from the Co n$p_{3/2}$ or n$p_{1/2}$ core level have a direct repercussion in the different satellite separations, as seen experimentally. However, the exact correlation effects that explain these differences, at the moment are not yet known.

The associated oxygen of the fully oxidized film consists of three peaks s0, s1 and s2. Peak s4 is attributed to a small amount of chemisorbed oxygen. The weak satellite feature, s1 and s2, can also be an effect in photoemission of structural defects in the film or even as Van Elp et al.[65] stated; the oxygen surrounding the cobalt ions can have several different final states distributed across the compound. It may be possible that because of the compound's strong crystal field, upon photoemission the final states in oxygen are produced. To support this idea, it is necessary to obtain X-ray absorption data where the excited core level electrons are promoted to the final states created in the hybridized valence band of Co_3O_4. If these signals readily appear in the absorption spectrum, then the satellite features in the photoemission spectra of oxygen are in fact oxygen final states.

6 Conclusions

With the reproduction of the experimental XPS data, it was possible to evaluate the chemical state of Co ultra-thin films. Calculated peak areas were introduced to the multilayer model with results close to stoichiometric values. Also, interesting XPS features were observed, like satellite peaks and background intensities that can only be seen peak fitting both photoemission branches comprising the Co 2*p* core level spectra.

Upon the completion of this work, the following statements can be concluded:

- An accurate estimation of the Co 2*p* photoemission spectra measured with an Al *K*α X-ray source requires the incorporation of three Auger peaks on the lower binding energy side of the spectra.
- With a proper background treatment using the active method, the peak fitting results strongly indicate that the Al *K*α X-ray source produces a Shirley contribution less intense than the Shirley intensity recorded with a Mg *K*α X-ray source.
- Spectral shapes of the main photoemission lines in the metallic Co 2*p* spectra indicate that asymmetry is caused by a multiplet splitting effect with different coupling schemes depending whether the core hole is created in the Co $np_{3/2,1/2}$ core level.
- When both the Co $2p_{3/2}$ and $2p_{1/2}$ branches in the XPS spectra are peak fitted, it is possible to observe characteristics of the satellite peaks that cannot be seen by just fitting the $np_{3/2}$ photoemission branch.
- The satellite peaks in the metallic Co photoemission spectra, as experimental evidence shows, concerns a shake-up feature that strongly depend on a correlation effect related to angular momentum.
- The Co 2*p* photoemission spectra of CoO has a strong satellite peak and two additional weak satellite peaks. These have different spin-orbit splitting values

that serve as evidence to further consider angular momenta correlation effects to explain satellite positions.

- The Co_3O_4 photoemission spectra presents a weak satellite feature with three distinctive satellite peaks. Also different satellite positions are observed and evidence indicates a strong dependency with angular momentum.
- The multilayer model is proved to be an accurate model to evaluate the chemical state of ultra-thin films.
- Assigning different Shirley background intensities to a spectrum composed of different chemical species, peak area calculations will result in close to stoichiometric chemical assessment results.
- Evaluation of the Shirley intensity across the oxidation process indicates that the Shirley intensity decreases with increasing oxidation state.
- An accurate experimental data reproduction alongside a precise background treatment outputs results for every compound measured that comply with stoichiometric values.

PERSPECTIVES

An accurate experimental data reproduction is important in the use of XPS as a quantitative technique. A precise background modeling is also imperative in peak area calculations. The methods used in the determination of the last issues is fundamental in the technological development of electronic devices where the characterization of multilayered systems is a key factor.

In this work a chemical assessment of Co ultra-thin films having stoichiometric oxide compounds was performed, the spectra analysis shows that precise chemical compositions are calculated by means of accurate experimental data reproduction and background modeling; however, from the basic science standpoint, several XPS features still require a comprehensive explanation of their true nature. Therefore the following work is proposed to try and resolve the issues encountered.

- Perform photoemission studies at the Co 2*p* and 3*p* thresholds in order to study the behavior of the shake-up features.
- Evaluate the photoemission spectra of metallic Co at different photon energies with the purpose of studying the Shirley background contribution to the spectra.
- Perform nuclear magnetic resonance studies to evaluate the different correlation effects produced in metallic Co.
- Perform early oxidation stages study of a metallic Cobalt thin film.
- Evaluate the photoemission spectra of cobalt oxide thin films with different crystalline phases.
- Perform XPS studies of partially oxidized films accompanied of REELS data with the aim of modeling the Tougaard contribution to the spectra.
- Develop more robust numerical methods with the purpose to explain the angular momentum dependency of satellite features, possibly using time dependent perturbation theory accompanied of time resolved photoemission studies.

REFERENCES

1. Suga, S. & Sekiyama, A. *Photoelectron Spectroscopy: Bulk and Surface Electronic Structures*. (Springer, 2014). doi:10.1007/978-3-642-37530-9

2. Sharma, A., Tripathi, S. & Shripathi, T. X-ray photoelectron study of annealed Co thin film on Si surface. *Appl. Surf. Sci.* **256,** 530–535 (2009).

3. Pappas, S. Facts About Cobalt. *Live Science* at <http://www.livescience.com/29275-cobalt.html>

4. Zhang, G., Scott, B. L. & Hanson, S. K. Mild and Homogeneous Cobalt-Catalyzed Hydrogenation of C□C, C□O, and C□N Bonds. *Angew. Chemie Int. Ed.* **51,** 12102–12106 (2012).

5. Van der Heide, P. *X-ray photoelectron spectroscopy: An introduction to principles and practices*. *JOHN WILEY & SONS, INC.* (Wiley, 2012).

6. Biesinger, M. C. *et al.* Resolving surface chemical states in XPS analysis of first row transition metals, oxides and hydroxides: Cr, Mn, Fe, Co and Ni. *Appl. Surf. Sci.* **257,** 2717–2730 (2011).

7. Farr, N. G. & Griesser, H. J. XPS excitation dependence of measured cobalt 2p3/2 peak intensity due to auger peak interference. *J. Electron Spectros. Relat. Phenomena* **49,** 293–302 (1989).

8. Biesinger, M. C., Payne, B. P., Lau, L. W. M., Gerson, A. & Smart, R. S. C. X-ray photoelectron spectroscopic chemical state Quantification of mixed nickel metal, oxide and hydroxide systems. *Surf. Interface Anal.* **41,** 324–332 (2009).

9. Seah, M. Background subtraction: I. General behaviour of Tougaard-style backgrounds in AES and XPS. *Surf. Sci.* **420,** 285–294 (1999).

10. Seah, M., Gilmore, I. & Spencer, S. Background subtraction: II. General behaviour of REELS and the Tougaard universal cross section in the removal of backgrounds in AES and XPS. *Surf. Sci.* **461,** 1–15 (2000).

11. Seah, M. Background subtraction III: The application of REELS data to background removal in AES and XPS. *Surf. Sci.* **471,** 185–202 (2001).

12. Herrera-Gomez, A., Bravo-Sanchez, M., Ceballos-Sanchez, O. & Vazquez-Lepe, M. O. Practical methods for background subtraction in photoemission spectra. *Surf. Interface Anal.* (2014). doi:10.1002/sia.5453

13. Herrera-Gomez, A. *A rigorous approach to the calculation of the uncertainties in XPS analysis*. (2014). at <http://www.qro.cinvestav.mx/~aherrera/reportesInternos/uncertaintiesXPS.pdf>

14. Hertz, H. . *Ann. Phys. U. Chem.* **31,** 421 (1887).

15. Einstein, A. . *Ann. Phys.* **17,** (1905).

16. Rutherford, E. *Philos. Mag.* **28,** (1914).

17. Rutherford, E., Robinson, H. & Rawlinson, W. F *Philos. Mag.* **18,** (1914).

18. Siegbahn, K. *ESCA-Atomic, Molecular and Solid State Structure Studied by Means of Electron Spectroscopy*. (1967).

19. Watts, J. F & Wolstenholme, J. *An Introduction to Surface Analysis by XPS and AES*. (John Wiley & Sons Ltd, 2003).

20. Hofmann, S. *Auger-and X-Rat Photoelectron Spectroscopy in Material Science.* (Springer-Verlag Berlin Heidelberg, 2013). doi:10.1007/978-3-642-27381-0

21. Condon, E. U. & Shortley, G. H. *The theory of atomic spectra. The University Press* (Cambridge, 1959). doi:10.1016/S0016-0032(35)90160-0

22. Haken, H. & Wolf, H. C. *The Physics of Atoms and Quanta*. (Springer, 2005). at <http://books.google.at/books?id=RBospa0ovKQC>

23. Chusuei, C. C. & Goodman, D. W. X-Ray Photoelectron Spectroscopy. *Encyclopedia of Physical Science and Technology* 921–938 (2002).

24. Herrera-Gomez, A. *et al.* Instrument-related geometrical factors affecting the intensity in XPS and ARXPS experiments. *J. Electron Spectros. Relat. Phenomena* **184,** 487–500 (2011).

25. Tougaard, S. & Sigmund, P. Influence of elastic and inelastic scattering on energy spectra of electrons emitted from solids. *Phys. Rev. B* **25,** 4452–4466 (1982).

26. Manson, S. T. & Cooper, J. W. *Phys. Rev.* **165,** (1968).

27. Reilman, R. F., Msezane, A. & Mansor, S. T. *J. Electron Spectros. Relat. Phenomena* **8,** 389–394 (1976).

28. Cooper, J. & Zare, R. N. Lectures in Theoretical Physics, Atomic Collision Processes. *J. Chem. Phys.* **48,** 942–943 (1969).

29. Yeh, J. & Lindau, I. Atomic subshell photoionization cross sections and asymmetry parameters: 1< Z< 103. *At. data Nucl. data tables* **32,** 1–155 (1985).

30. Cooper, J. W. & Manson, S. T. . *Phys. Rev.* **177,** 157–163 (1969).

31. Herrera-Gomez, A. Effect of monochromator X-ray Bragg reflection on photoelectric cross section. *J. Electron Spectros. Relat. Phenomena* **182,** 81–83 (2010).

32. Weisstein, E. W. Gaussian Function. *MathWorld--A Wolfram Web Resource* (2015). at <http://mathworld.wolfram.com/GaussianFunction.html>

33. Weisstein, E. W. Lorentzian Function. *MathWorld--A Wolfram Web Resource* (2015). at <http://mathworld.wolfram.com/LorentzianFunction.html>

34. Hüfner, S. *Photoelectron Spectroscopy: principles and applications*. (Springer-Verlag Berlin Heidelberg, 2003). doi:10.1007/978-3-662-09280-4

35. Carlson, T. A. *Photoelectron and Auger Spectroscopy*. (Plenum Press, 1978). doi:10.1007/978-1-4757-0118-0

36. Kotani, A. & Toyozawa, Y. Optical Spectra of Core Electrons in Metals with an Incomplete Shell. II. Numerical Calculations of Overall Line Shapes. *J. Phys. Soc. Japan* **35,** 1082–1088 (1973).

37 Kotani, A. & Toyozawa, Y. Optical Spectra of Core Electrons in Metals with an Incomplete Shell. I. Analytic Features. *J. Phys. Soc. Japan* **35,** 1073–1081 (1973).

38. Kotani, A. & Toyozawa, Y. Photoelectron Spectra of Core Electrons in Metals with an Incomplete Shell. *J. Phys. Soc. Japan* **37,** 912–919 (1974).

39. Mahan, G. D. Collective excitations in x-ray spectra of metals. *Phys. Rev. B* **11,** 4814–4824 (1975).

40. Nozières, P. & De Dominicis, C. T. Singularities in the X-Ray Absorption and Emission of Metals. III. One-Body Theory Exact Solution. *Phys. Rev.* **178,** 1097–1107 (1969).

41. Doniach, S. & Šunjic, M. Many-electron singularity in X-ray photoemission and X-ray line spectra from metals. *Journal of Physics C: Solid State Physics* **3,** 285–291 (1970).

42. Hüfner, S. & Wertheim, G. K. Core-line asymmetries in the x-ray photoemission spectra of metals: A comment. *Phys. Rev. B* **11,** 5197–5198 (1975).

43. Hüfner, S., Wertheim, G. K. & Wernick, J. H. XPS core line asymmetries in metals. *Solid State Commun.* **17,** 417–422 (1975).

44. Hüfner, S. & Wertheim, G. K. Core-line asymmetries in the x-ray-photoemission spectra of metals. *Phys. Rev. B* **11,** 678–683 (1975).

45. Herrera-Gomez, A. *A double Lorentzian shape for asymmetric photoelectron peaks*. (2011). at <http://www.qro.cinvestav.mx/~aherrera/reportesInternos/doubleLorentzian.pdf>

46. Shirley, D. High-resolution X-ray photoemission spectrum of the valence bands of gold. *Phys. Rev. B* **5,** 4709–4714 (1972).

47. Tougaard, S. Practical algorithm for background subtraction. *Surf. Sci.* **216,** 343–360 (1989).

48. Végh, J. The Shirley background revised. *J. Electron Spectros. Relat. Phenomena* **151,** 159–164 (2006).

49. Proctor, A. & Sherwood, P Data analysis techniques in x-ray photoelectron spectroscopy. *Anal. Chem.* 13–19 (1982). at <http://pubs.acs.org/doi/abs/10.1021/ac00238a008>

50. Fadley, C. & Shirley, D. X-Ray Photoelectron Spectroscopic Study of Iron, Cobalt, Nickel, Copper, and Platinum. *Phys. Rev. Lett.* **21,** 980–983 (1968).

51. Haber, J. & Ungier, L. ON THE CHEMICAL SHIFTS OF ESCA AND AUGER LINES IN COBALT OXIDES. *J. Electron Spectros. Relat. Phenomena* **12,** 305–312 (1977).

52. Haber, J., Stoch, J. & Ungier, L. X-Ray Photoelectron Spectra of Oxygen in Oxides of Co, Ni, Fe and Zn. *J. Electron Spectros. Relat. Phenomena* **9,** 459–467 (1976).

53. Borod´Ko, Y. G., Vetchinkin, S. I., Zimont, S. L., Ivleva, I. N. & Shul'Ga, Y. M. NATURE OF SATELLITES IN X-RAY PHOTOELECTRON SPECTRA XPS OF PARAMAGNETIC COBALT (II) COMPOUNDS. *Chem. Phys. Lett.* **42,** 264–267 (1976).

54. McIntyre, N. S. & Cook, M. G. X-ray photoelectron studies on some oxides and hydroxides of cobalt, nickel, and copper. *Anal. Chem.* **47,** (1975).

55. McIntyre, N. S., Johnston, D. D., Coatsworth, L. L. & Davidson, R. D. X-ray Photoelectron Spectroscopic Studies of Thin Film Oxides of Cobalt and Molybdenum. *Surf. Interface Anal.* **15,** 265–272 (1990).

56. Carson, G. A., Nassir, M. H. & Langell, M. A. Epitaxial growth of Co3O4 on CoO(100). *J. Vac. Sci. Technol. A Vacuum, Surfaces, Film.* **14,** 1637 (1996).

57. Jeng, S., Zhang, Z. & Henrich, V. E. O_ {2} chemisorption on CoO (100): A resonant-photoemission study. *Phys. Rev. B* **44,** 3266–3271 (1991).

58. Klingenberg, B., Grellner, F., Borgmann, D. & Wedler, G. Oxygen adsorption and oxide formation on Co (11-20). *Surf. Sci.* **296,** 374–382 (1993).

59. Jiménez, V. M., Fernández, A., Espinós, J. P & González-Elipe, A. R. The state of the oxygen at the surface of polycrystalline cobalt oxide. *J. Electron Spectros. Relat. Phenomena* **71,** 61–71 (1995).

60. Robert, T. CORRELATION BETWEEN CHEMICAL BONDING AND SATELLITE LINES IN X-RAY PHOTOELECTRON SPECTRA OF TRANSITION METAL COMPOUNDS. *Chem. Phys.* **8,** 123–135 (1975).

61. Robert, T. & Offergeld, G. SELECTION RULES AND SHAKE-UP SATELLITES IN X-RAY PHOTOELECTRON SPECTRA OF TRANSITION METAL COMPOUNDS. *Chem. Phys. Lett.* **29,** 4–6 (1974).

62. Raaen, S. Correlation effects in 3d transition metals: Presence of a two-hole core-satellite in cobalt. *Solid State Communications* **60,** 991–993 (1986).

63. Raaen, S. & Murgai, V. Absence of two-electron resonances in valence-band photoemission from Cr, Mn, Fe, and Co. **36,** 887–890 (1987).

64. Frost, D. C., Mcdowell, C. A. & Wallbank, B. CHARGE TRANSFER SHAKE-UP SATELLITES IN X-RAY PHOTOELECTRON SPECTRA OF SOLID COMPOUNDS OF 3d0 IONS. *Chem. Phys. Lett.* **40,** (1976).

65. Van Elp, J. *et al.* Electronic structure of CoO, Li-doped CoO, and LiCoO2. *Phys. Rev. B* **44,** 6090–6103 (1991).

66. Eskes, H. & Sawatzky, G. A. Doping dependence of high-energy spectral weights for the high-Tc cuprates. *Phys. Rev. B* **43,** 119–129 (1991).

67. Grosvenor, A. P., Wik, S. D., Cavell, R. G. & Mar, A. Examination of the Bonding in Binary Transition-Metal Monophosphides MP (M = Cr, Mn, Fe, Co) by X-Ray Photoelectron Spectroscopy. *Inorg. Chem.* **44,** 8988–8998 (2005).

68. Lee, G. & Oh, S. J. Electronic structures of NiO, CoO, and FeO studied by 2p core-level x-ray photoelectron spectroscopy. *Phys. Rev. B* **43,** 14674–14682 (1991).

69. Díaz-Fernández, D. *et al.* The growth of cobalt oxides on HOPG and SiO 2 surfaces : A comparative study. *Surf. Sci.* **624,** 145–153 (2014).

70. Kern, W. & Puotinen, D. A. Cleaning solutions based on hydrogen peroxide for use in silicon semiconductor technology. *RCA Rev.* **186,** (1970).

71. Conny, J. M. & Powell, C. J. Standard test data for estimating peak parameter errors in x-ray photoelectron spectroscopy: II. Peak intensities. *Surf. Interface Anal.* **29, 444–459** (2000).

72. Conny, J. M. & Powell, C. J. Standard test data for estimating peak parameter errors in x-ray photoelectron spectroscopy III. Errors with different curve-fitting approaches. *Surf. Interface Anal.* **29,** 856–872 (2000).

73. Carley, A. F & Joyner, R. W. The application of deconvolution methods in electron spectroscopy — a review. *J. Electron Spectros. Relat. Phenomena* **16,** 1–23 (1979).

74. Beatham, N. & Orchard, A. F The application of Fourier transform techniques to the problem of deconvolution in photoelectron spectroscopy. *J. Electron Spectros. Relat. Phenomena* **9,** 129–148 (1976).

75. Sprenger, D. & Anderson, O. Deconvolution of XPS spectra. *Fresenius. J. Anal. Chem.* 116–120 (1991). at <http://link.springer.com/article/10.1007/BF00322120>

76. Koenig, M. F. & Grant, J. T. Deconvolution in X-ray photoelectron spectroscopy. *J. Electron Spectros. Relat. Phenomena* **33,** 9–22 (1984).

77. Muñoz-Flores, J. & Herrera-Gomez, A. Resolving overlapping peaks in ARXPS data: The effect of noise and fitting method. *J. Electron Spectros. Relat. Phenomena* **184,** 533–541 (2012).

78. Végh, J. The analytical form of the Shirley-type background. *J. Electron Spectros. Relat. Phenomena* **46,** 411–417 (1988).

79. Salvi, A. M. & Castle, J. E. The intrinsic asymmetry of photoelectron peaks: dependence on chemical state and role in curve fitting. *J. Electron Spectros. Relat. Phenomena* **95,** 45–56 (1998).

80. Herrera-Gomez, A. *The Peak-Shirley Background*. (2012). at <http://www.qro.cinvestav.mx/~aherrera/reportesInternos/peakShirley.pdf>

81. Tougaard, S. Universality Classes of Inelastic Electron Scattering Cross-sections. *Surf. Interface Anal.* **25,** 137–154 (1997).

82. Herrera-Gomez, A., Bravo-Sanchez, M., Aguirre-Tostado, F S. & Vazquez-Lepe, M. O. The slope-background for the near-peak regimen of photoemission spectra. *J. Electron Spectros. Relat. Phenomena* **189,** 76–80 (2013).

83. Scofield, J. H. *Theoretical photoionization cross sections from 1 to 1500 keV*. (1973). doi:10.2172/4545040

84. Herrera-Gomez, A. *Self consistent ARXPS analysis for multilayer conformal films with abrupt interfaces*. (2008). at <http://www.qro.cinvestav.mx/~aherrera/reportesInternos/arxpsAnalysisSharpIntefaces.pdf>

85. Powell, C. J. & Jablonski, A. *NIST Electron Effective-Attenuation-Length Database - Version 1.3*. (National Institute of Standards and Technology, 2011).

86. C, M., Sanz, J. M., Galán, L., Soriano, L. & Rueda, F. AN XPS STUDY OF THE INTERACTION OF OXYGEN WITH ZIRCONIUM. *Surf. Sci.* **218,** 331–345 (1989).

87. Nyholm, R., Mårtensson, N., Lebugle, a. & Axelsson, U. Auger and Coster-Kronig broadening effects in the 2p and 3p photoelectron spectra from the metals 22Ti-30Zn. *J. Phys. F Met. Phys.* **11,** 1727 (1981).

88. Mahan, G. D. Excitons in Metals: Infinite Hole Mass. *Phys. Rev.* **163,** 612–617 (1967).

89. Fadley, C. & Shirley, D. Multiplet Splitting of Metal-Atom Electron Binding Energies. *Phys. Rev. A* **2,** 1109–1120 (1970).

90. López, M. F *et al.* Resonant photoemission at the 2p thresholds of Fe, Co, and Ni metal. *Zeitschrift für Phys. B Condens. Matter* **95,** 9–12 (1994).

91. Tougaard, S. & Chorkendorff, I. Differential inelastic electron scattering cross sections from experimental reflection electron-energy-loss spectra: Application to background removal in electron spectroscopy. *Phys. Rev. B* **35,** 6570–6577 (1987).

92. Shen, Z. X. *et al.* Photoemission study of CoO. *Phys. Rev. B* **42,** 1817–1828 (1990).

93. Kim, K. X-ray-photoelectron spectroscopic studies of the electronic structure of CoO. *Phys. Rev. B* **11,** 2177–2185 (1975).

94. Hassel, M. & Freund, H.-J. NO on CoO(111)/Co(0001): hydroxyl assisted adsorption. *Surf. Sci.* **325,** 163–168 (1995).

95. Hassel, M. & -J., F H. High Resolution XPS Study of a Thin CoO(111) Film Grown on Co(0001). *Surf. Sci. Spectra* **4,** 273 (1996).

CONFERENCE PRESENTATIONS

Oral

- **Dagoberto Cabrera Germán**, Jorge Alejandro Torres Ochoa, Gabriela Molar-Velazquez, Gustavo Gómez Sosa, Wencel de la Cruz, Alberto Herrera Gómez, 2015, The Shirley background of the Tougaard background in the photoemission spectra of transition metals. *VIII International Conference on Surfaces, Materials and Vacuum*. Puebla, México.

Poster

- **Dagoberto Cabrera Germán**, Jorge Alejandro Torres Ochoa, Gustavo Gómez Sosa, Alberto Herrera Gómez, 2015, CHARACTERIZATION OF METALLIC COBALT AND COBALT OXIDES THROUGH QUANTITATIVE XPS ANALYSIS. *XXIV International Materials Research Congress*. Cancún, México.
- Andrés de Luna Bugallo, Yuri Lizbeth Chipatecua Godoy, **Dagoberto Cabrera Germán**, Jorge Alejandro Torres Ochoa, Gustavo Gomez Sosa, Zeuz Montiel González, Alberto Herrera Gómez, 2015, SOFT NITRIDATION OF HAFNIUM OXIDE USING REMOTE PLASMA SOURCE. *XXIV International Materials Research Congress*. Cancún, México.
- G. Gomez-Sosa, J.A. Torres-Ochoa, M. Bravo-Sanchez, J.H. Mata-Salazar, **D. Cabrera-German**, J. Ibarra-Nuno, A. Herrera-Gomez, 2014, Double-Lorentzian Line Shape in XPS Analysis of Metallic Nickel, Chromium, Cobalt and Their Oxide Films. *Pacific Rim Symposium on Surfaces, Coatings and Interfaces (PacSurf 2014)*. Kohala Coast, USA.
- **Dagoberto Cabrera-Germán**, Gustavo Gómez- Sosa, Julio Heriberto Mata-Salazar, Alberto Herrera- Gomez, 2014, Quantitative approach for assessing the chemical state of cobalt oxide ultra-thin films using the double-Lorentzian asymmetric line-shape in XPS analysis. *VII International Conference on Surfaces, Materials and Vacuum*. Ensenada, México. (Best Poster Presentation)

EL JURADO DESIGNADO POR LA UNIDAD QUERÉTARO DEL CENTRO DE INVESTIGACIÓN Y DE ESTUDIOS AVANZADOS DEL INSTITUTO POLITÉCNICO NACIONAL, APROBÓ LA TESIS DE MAESTRÍA DEL C. DAGOBERTO CABRERA GEMÁN TITULADA: "ANÁLISIS DEL ESPECTRO DE FOTOEMISIÓN DEL Co 2*p* EN COBALTO METÁLICO Y OXIDADO", FIRMAN AL CALCE DE COMÚN ACUERDO LOS INTEGRANTES DE DICHO JURADO, EN LA CIUDAD DE QUERÉTARO, QRO., A LOS VEINTIOCHO DÍAS DEL MES DE SEPTIEMBRE DE DOS MIL QUINCE.

Dr. ALBERTO HERRERA GÓMEZ

Dr. SERGIO JOAQUÍN JIMÉNEZ SANDOVAL

Dr. ANDRÉS DE LUNA BUGALLO